University of Groningen

Kapteyn Astronomical Institute

Halo mass estimates of Fornax Galaxies from Globular Cluster populations

Master Thesis

Author:
Lorraine Putman
S3117774

Supervisor:
Prof. dr. Reynier Peletier
Teymoor Saifollahi

Abstract

One possible pathway for understanding the formation and evolution of galaxies is by studying their earliest stellar structures, namely globular clusters (GC). In this work, we present the number of GCs for 540 dwarf galaxies in the Fornax Cluster, which is currently the largest dwarf galaxy sample with GC counts in the literature. Based on the number of GCs in the galaxies we estimated their dark matter halo masses. To obtain the number of GCs, we subtracted an elliptical model from the images of the dwarf galaxies in the g, r and i bands from the Fornax Deep Survey, and thereby improved the detection of GCs on top of these galaxies. After applying aperture photometry, a selection of the data was matched to already observed GCs from the HST/ACS survey of the Fornax Cluster to determine how GC candidates should be selected. This was possible for 19 galaxies. Criteria were determined based on the values of the matched GCs and used for the GC selection of the resulting galaxies. These selection criteria include g-band magnitude, colors (g-r, r-i) and a compactness parameter representing the difference in magnitude between aperture sizes of 4 and 8 pixels. These selection criteria were also applied on empty fields to determine a statistical background correction for the number of GCs. For the analysis, we subdivided the sample in various ways to investigate the number and specific frequency of GCs as a function of location, early- and late-type galaxies, nucleated and non-nucleated galaxies and surface brightness. We find a higher number of GCs for early-type, nucleated and lower surface brightness galaxies. The higher number of GCs in early-type galaxies is affected by the distribution of the early- and late-type galaxies, because early-type galaxies are more concentrated in the center. Similarly, nucleated galaxies are also more concentrated in the center of the cluster. Additionally, the higher number of GCs in nucleated galaxies can be linked to nuclear star cluster formation paths by the inspiralling of the GCs. Lower surface brightness galaxies have on average a higher number of nucleated star clusters. However, the difference in number of GCs for low and high surface brightness galaxies remains when only nucleated galaxies are considered. The number of GCs is higher in the center of the Fornax Cluster than in the region around Fornax A, consistent with the fact that the GC number in the center of the dense Virgo cluster is higher than in all other regions. Finally, we have also derived the dark matter halo mass for the dwarf galaxies using the scaling relation between the number of GCs and the dark halo mass of a galaxy.

Acknowledgements

First of all, I would like to thank Reynier for his guidance, motivation and honesty. I have learned a lot during the past year and due to your feedback I became more critical towards my work and results. Your honesty has taught me to not take everything personal. I have enjoyed all our talks and appreciate all your help with respect to the project but also for the future. Together with Teymoor, your motivation has inspired me. I would also like to thank Teymoor for his kind and helpful words when I needed them most. I admire your confidence and I have learned a lot from you. I have enjoyed working with you two very much and I advise it to everybody. Unfortunately, the circumstances did not allow cakes but I hope to still make up for this the upcoming time.

I would also like to thank my family for your encouragements and love. You are always open to help or to listen, but also the capability of my brothers showing me your love through annoying comments.

My friends, thank you for all the coffee breaks, dinners and gezelligheid throughout the past year.

I would like to thank Paul and Coppa for your love and support. You have made working at home much more fun and peaceful.

Finally, I would like to thank you my nieces and nephew for all your joy and hugs which have the capacity to turn every sad day around.

Contents

1 Introduction

It is consensus in the literature that in the early Universe globular clusters (GC) formed when protogalaxies merged. As a result, the GCs only contain very old stars [Carretta, E. et al., 2010; Letarte et al., 2006; Larsen et al., 2014]. GC systems have been found in both old elliptical galaxies and in younger spiral galaxies for a range of masses. Studying these systems brings us further in understanding galaxy formation and evolution. GCs are compact gravitationally bound spherical stellar systems. GCs can be described by several physical size parameters, such as the half-light radius (r_h). A typical half-light radius for GC in the Milky Way is $\sim 2-3\ pc$ with a mean mass of $\sim 1 \times 10^5 M_\odot$ [Harris, 1996; Peterson and King, 1975]. The age and metallicity distribution of GC stars is simpler than that of galaxies due to their star-formation history. The simple stellar population, high luminosity and large galactocentric distances which extend several effective radii of the host galaxy makes them attractive to study when investigating a galaxy and its environment. Most galaxies contain globular clusters.
GCs can be used to study the mass assembly of galaxies and trace their mass content in several ways, such as the relations visible in Fig. 1. The GCs mass is plotted versus the stellar mass and the dark matter halo mass. The right panel, shows the linear correlation between the GCs mass and the dark matter halo mass of the host galaxy [Hudson et al., 2014; Harris et al., 2015].

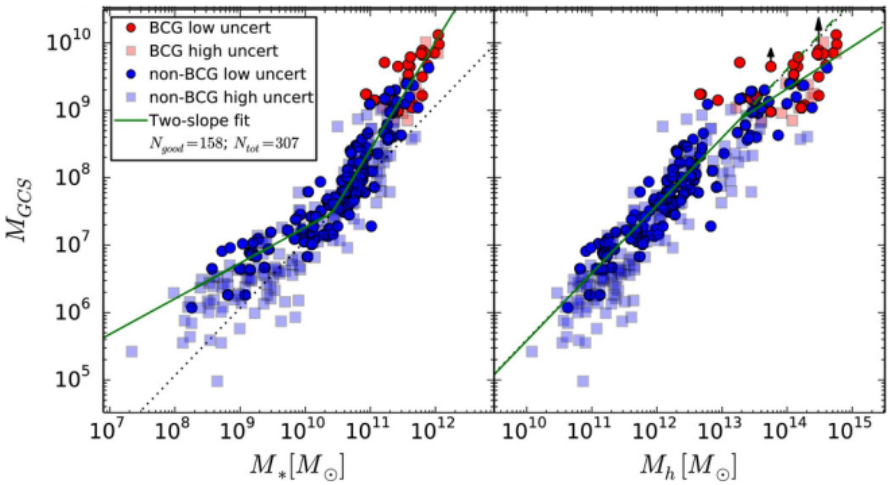

Figure 1: Left panel: Total mass of GCs versus the stellar mass. Right panel: Total mass of GCs versus the dark matter halo mass showing a linear relation. This figure is taken from Hudson et al. [2014]

1.1 Formation of GCs

To be able to describe the formation and evolution of GCs, many distinct processes need to be captured within a model. Some example processes are star cluster formation, the initial mass function, destruction paths by tidal perturbations and relocation due to hierarchical galaxy assembly. There are different models that try to describe the GC formation and evolution. One of these theories considers the GCs to be formed in the most massive gas-rich environments with high star formation rates (SFR), similar to young massive clusters (YMC) which are observed in merging galaxies [Holtzman et al., 1992; Whitmore et al., 1999]. This happened most often in the early universe.

More massive galaxies can also accrete GCs as a result of galaxy mergers [Kim et al., 2018; Li et al., 2017; Renaud et al., 2017] or their GC formation takes place in galaxy discs [Kruijssen, 2015; Pfeffer et al., 2018]. This formation path would take place in normal high-redshift galaxies with gas-rich environments. Alternatively, some GCs may form during or before the reionisation in low-mas dark matter haloes [Peebles and Dicke, 1968; Kimm et al., 2016].

To expand our knowledge on GC formation, larger samples and different environments need to be studied. Throughout the years, many works have investigated GCs, especially in the Milky Way which contains many accreted GCs [Leaman et al., 2013; Kruijssen et al., 2019]. For the extragalactic GC systems the focus lays on early-type galaxies (ETG) which are easier to observe due to the smooth light profile of ETGs. In late-type galaxies it is more difficult to select the GCs due to the spiral arms and the fact that they do not reach the high mass that ETGs can reach.
We will discuss several works that investigate GCs and that are important for this work more in detail below.

1.2 Connections between GCs and their host galaxies

To understand the nature and evolution of the number of GCs within galaxies, most studies investigate the correlations between GCs and properties of their host galaxy.

The work of Georgiev et al. [2010] also investigated the difference in number of GCs between early- and late-type galaxies. More specifically, they investigated the specific luminosity, luminosity ratio of GCs and the luminosity of the host galaxy, and found that early-type galaxies on average have a value twice as high compared to late-type galaxies.

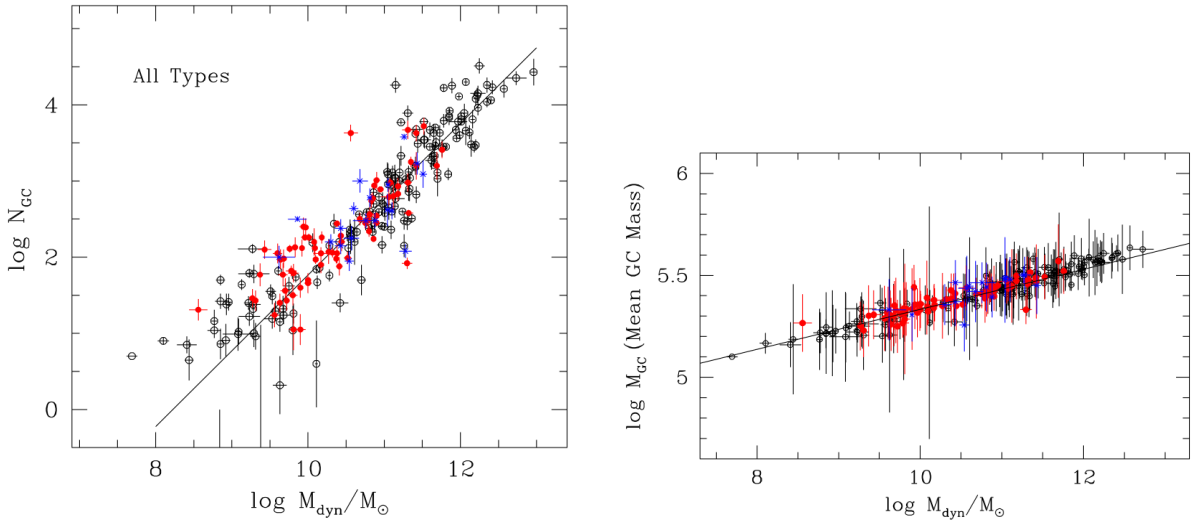

Figure 2: Left panel: The number of GCs versus the dynamical mass for different types of galaxies. The different types of galaxies are denoted by different markers and colours and the diagonal line shows the best fit for galaxies with $M_{dyn} > 10^{10} M_{\odot}$. Right panel: The mean GC mass versus the dynamical mass for different types of galaxies. The diagonal line represents the best fit relation. These figures come from Harris et al. [2013].

Currently the best way to study GCs around galaxies is through HST, given its high spatial resolution. Peng et al. [2008] observed 100 early-type galaxies in the ACS Virgo Cluster Survey

using HST. A full description of the survey can be found in Cote et al. [2004]. They investigated the number of GCs in these ETGs, more specifically the specific frequency, S_N, introduced by Harris and van den Bergh [1981]. This is the number of GCs per unit stellar luminosity, representing the efficiency of GC formation with respect to the field stars. The Virgo cluster ETGs show a 'U-shaped' relation between the S_N and the luminosity which can be seen from Fig. 3. The work of Peng et al. [2008] covers the regions from giants to dwarfs. They also investigated the role of the environment on the number of GCs. They found that galaxies closer to the center of the cluster have a higher S_N. One possible explanation is that the low-mass galaxies in dense regions have a higher SFR at early times resulting in more GCs. It is also possible that the SF stopped earlier for galaxies in dense environments, which would not have any effect on the formation of GCs due to their early creation [Liu et al., 2016]. However, this environmental dependence was not found in the sample of Miller and Lotz [2007]. Therefore, more evidence is needed to understand the environmental effects, for example by studying different galaxy clusters. Liu et al. [2019] investigated 43 galaxies in the Fornax Cluster (ACSFCS: Jordan et al. [2007]). The Virgo cluster has a larger virial radius and mass density than the Fornax cluster. Liu et al. [2019] found similar properties for the $S_{N,z}$ for the ETGS from both clusters and they found an environmental dependence for the low-mass ETGs. The environmental dependence comes through the low $S_{N,z}$ of ETGS that are located within $10 \times R_e$ of the most massive galaxies in the sample of Liu et al. [2019] so their GC systems are likely tidally stripped. However, they also found that a denser environment, not too close to a bright heavy galaxy, can improve the GC formation because other high $S_{N,z}$ galaxies are located around massive neighbors. Different types of galaxies have on average a different S_N. It is even possible for dwarf galaxies to have comparable specific frequencies to giant ellipticals (see Fig. 3) [Lotz et al., 2004; Miller and Lotz, 2007; Durrell et al., 1996], proposing the possibility for the formation of halos of larger galaxies through accretion [Searle and Zinn, 1978; Côté et al., 1998, 2000].

1.2.1 Dwarf galaxies

The main focus of this work will be in fainter magnitude ranges studying dwarf galaxies. Dwarf galaxies can be classified in several manners, for example by morphology or surface brightness. Due to the large variety of shapes and characteristics of dwarf galaxies, it is also possible to divide the sample in multiple sub-classes.

From Fig. 3 we see high S_N values for dwarf galaxies. A possible explanation could be that these galaxies formed their stars during high efficiency moments. The SFR was especially high during early times which would result in high S_N values. The spread in the S_N could then be caused by a spread in the formation times. Due to the high efficiency in the star formation (SF), the galaxies could gain enough mass before their SF is stopped by feedback [Elmegreen and Efremov, 1997; Kruijssen, 2012].

Recently, the statistics in the dwarf sample has been increased significantly by the work of Carlsten et al. [2021a]. They investigated GCs and nuclear-star clusters of early-type satellites from the Exploration of Local VolumE Satellites (ELVES) Survey. Their findings are in line with the increased S_N in denser environment results from Peng et al. [2008]; Liu et al. [2019] and they proposes three possible causes. An increase in GC creation due to the formation in early collapsing halos, a decrease in the GC destruction in denser environments from earlier quenching or increased merger rates, and decreased field star formation from earlier quenching. Carlsten et al. [2021a] also found a strong correlation between GCs and nuclear-star clusters which is also influenced by the environment. The nucleation fraction of dwarf satellites is lower than the fraction from dwarfs present in clusters.

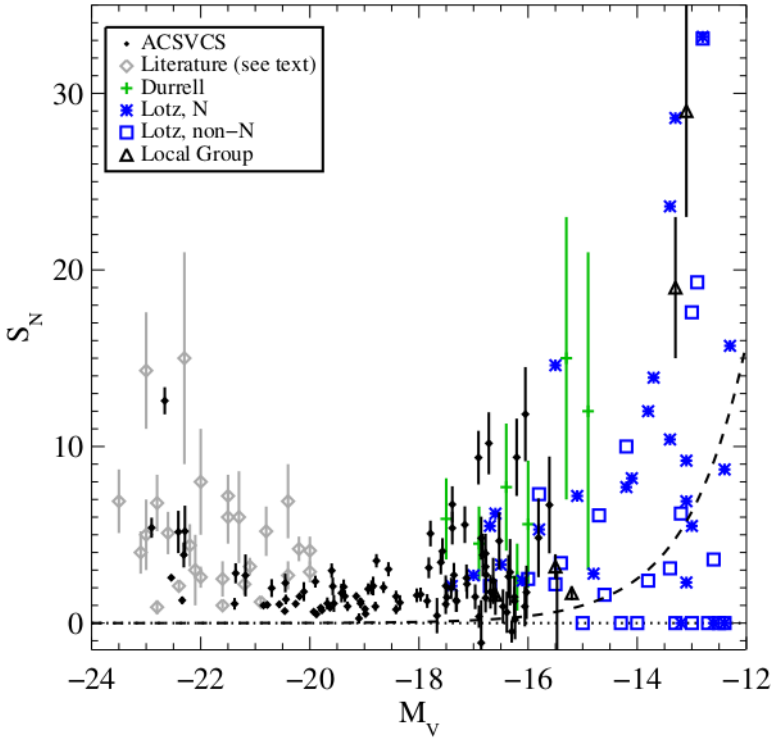

Figure 3: Specific frequency versus M_V for 100 ACSVCS galaxies (black circles) [Peng et al., 2008]. Dwarf galaxies from Durrell et al. [1996] and Lotz et al. [2004]. The literature values are taken from Kissler-Patig et al. [1996, 1997]; Dirsch, B. et al. [2003]; Dirsch et al. [2003, 2005]; Forbes et al. [1996]; Rhode and Zepf [2004]; Zepf et al. [1995]; Harris et al. [2004]. This figure comes from Peng et al. [2008].

1.2.2 Dark matter halos

Another important relation between the GCs and the host galaxy, is the GC mass fraction from the total halo mass. The total stellar mass contained within the GCs is determined through the globular cluster luminosity function (GCLF) and the M/L ratio. The GCLF is represented by a Gaussian shape, where the peak and the standard deviation depend on the galaxy luminosity. The largest part of the mass determination is accounted for by the brightest part of the GCLF. The GC mass trend can be seen in the right panel of Fig. 2, where the mean GC mass is equal to M_{GCs}/N_{GC}.

Harris et al. [2013] conducted research to investigate several of these correlations. They gathered already published number of GCs for a range of galaxy luminosities. They also investigated the relation between the number of GCs and the dynamical mass of the galaxy defined by Eq. 1.2.2 [Wolf et al., 2010]:

$$M_{dyn} = \frac{4R_e\sigma_e^2}{G}, \tag{1}$$

where R_e is the effective radius, σ_e is the stellar velocity dispersion and G is the gravitational constant. The dynamical mass does show a linear correlation with the number of GCs as can be seen from the left panel of Fig. 2. Similar correlations are shown in Peng et al. [2008]; Georgiev et al. [2010]; Spitler et al. [2008], but these works use masses determined photometrically. The

number of GCs increases with the dynamical mass almost linearly. Harris et al. [2013] does note that if this relation is valid for both spiral and elliptical galaxies, then the spiral galaxies will have less GCs per unit dynamical mass than elliptical galaxies. This off-set is accounted for in the left panel Fig. 2 and therefore not visible in this figure.

Harris et al. [2013] also calculated the specific mass, which is defined as the percentage GC mass of the dynamical mass, $S_M = 100\frac{M_{GCS}}{M_{dyn}}$. Throughout different works, slightly different definitions of the specific mass are used [Peng et al., 2008; Georgiev et al., 2010] which also leads to different discussion points and explanations. The specific mass calculated in Harris et al. [2013] can be seen in Fig. 4, which shows a similar shape to the S_N relation. Low mass galaxies ($log(M_{dyn}/M_\odot) \approx 6-9$) have a higher GC mass fraction just as high mass galaxies ($log(M_{dyn}/M_\odot) \approx 11-13$,) while the ratio is the lowest for the intermediate-luminosity and mass galaxies. This means that the SF was most efficient for the intermediate-mass galaxies. Internal and external quenching effects caused the low and high mass galaxies to have less efficient SF. The GCs could be formed in the earliest starbursts in the densest regions. Subsequent SF rounds could then be truncated for low and high mass galaxies which could explain the U-shape from Fig. 4. The truncation of SF is likely different depending on the galaxy mass. In the lower mass galaxies intrinsic process, such as starburst winds, photoionization or supernovea (SNe), will quench the SF. In high mass galaxies the quenching will be caused trough tidal stripping of the gas or UV fields heating the the gas of the galaxy.

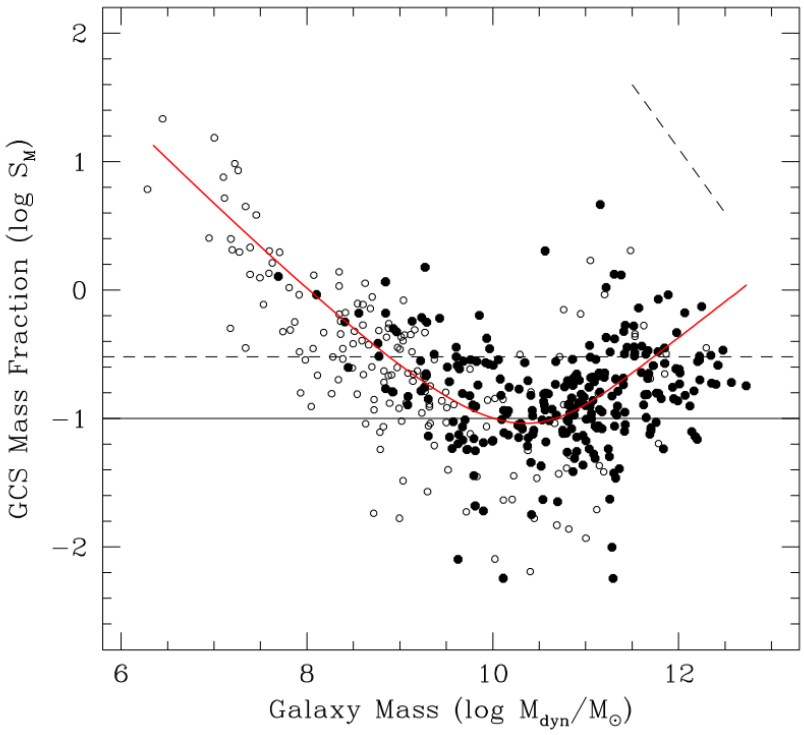

Figure 4: The specific mass frequency versus the galaxy mass, where the specific mass frequency is $S_M = 100(M_{GCs}/M_{dyn})$. The dynamical mass is determined either through effective radius and the central velocity dispersion (R_e, σ_e) or from the luminosity (L_v). This figure is taken from Harris et al. [2013].

1.3 Fornax Deep Survey

The Fornax Deep Survey (FDS) is a collaboration between two surveys, the Fornax Cluster Ultra-deep Survey (FoCUS, PI: R. Peletier) and the VST Early-Type GAlaxy Survey (VEGAS, PI: E. Iodice). The survey is centered on NGC 1399, the brightest galaxy of the main Fornax cluster and the Fornax A sub-group which is centered on NGC 1316, the brightest galaxy of the complete Fornax cluster. The coverage can be seen in Fig. 5. The Fornax Deep Survey is a very deep survey, about 3 mag deeper than SDSS. It contains data in the SDSS u-, g-, r- and i-band and corresponding weight maps. Five fields around the Fornax A subcluster are only observed in the g-, r- and i-band. The VLT Survey Telescope [Schipani et al., 2012] is the telescope that operated for the FDS and in 2.6 m long telescope with the OmegaCAM [Kuijken et al., 2002] attached. The OmegaCAM has 32 CCDs with a $1 \times 1\ deg^2$ field and a resolution of 0.21 $arcsec$ pixel^{-1} ($5\ pix \approx 1\ arcsec$). For more information on the observations see Venhola et al. [2017]; Iodice et al. [2016].

The dwarf galaxies in the Fornax cluster are published in the Fornax Deep Survey Dwarf galaxy Catalog (FDSDC) and consists of a total of 564 dwarfs [Venhola et al., 2018a]. This catalog reaches the 50% completeness at the limiting magnitude of $M_r = -10.5\ mag$ with a mean effective surface brightness of $\overline{\mu}_{e,r} = 26\ mag/arcsec^2$.

Cantiello et al. [2020] uses the FDS to derive photometry of compact sources, more specifically GCs, and their distribution throughout the Fornax cluster. Around the central galaxy in the cluster, NGC 1399, an over-density of GCs is found. There is no clear structure of GCs found between NGC 1399 and the Fornax A subgroup central galaxy, NGC 1316, which also does not show a rich intra-cluster GCs population such as NGC 1399.

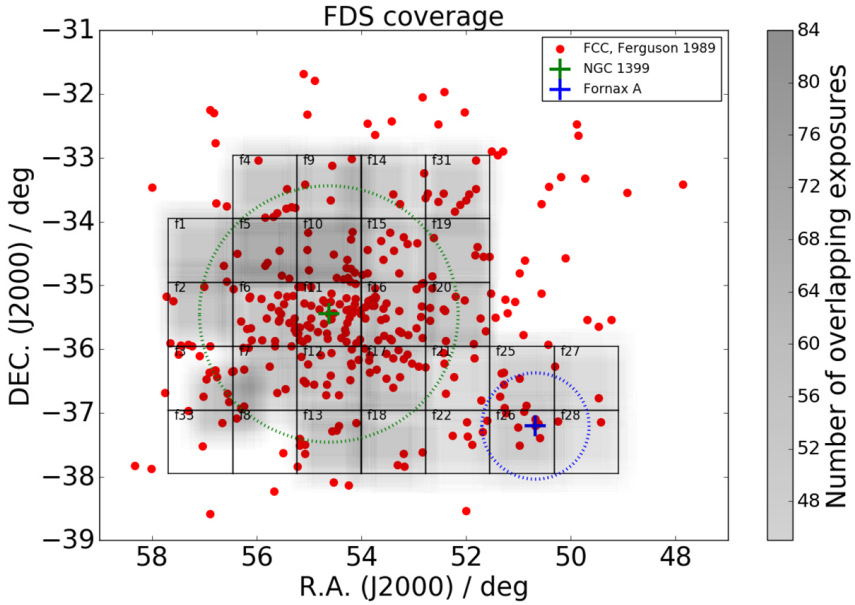

Figure 5: The complete coverage of the Fornax Deep Survey including galaxies labeled as FCC galaxies from Ferguson and Sandage [1989]. The green circle is the virial radius of NGC 1399 of 0.7 Mpc [Drinkwater et al., 2001] and the blue circle displays a 2σ over-density around NGC 1316. This figure comes from Venhola et al. [2018b].

1.4 This thesis

This thesis is structured as follows: in Chapter 2 we describe the sample, the GCs selection method and the analytical framework that is used to compare data to other works; in Chapter 3 we show the number of GCs for the complete sample of 540 dwarf galaxies of Fornax; in Chapter 4 we will compare our findings to other works; in Chapter 5 we will discuss our results and give possible explanations; in Chapter 6 we will summarize this work.

2 Methodology

In this Chapter, we will describe the method used for observing and selecting GCs. There is a GC sample based on HST data, which is used to construct a method to select new GCs for the resulting dwarf galaxies. In Section 2.1, we will elaborate on the dwarf galaxies samples and the HST sample; in Section 2.2 we will clarify the steps for modelling the galaxy light; in Section 2.3 the photometric measures are described; in Section 2.4 we explain the method for finding new GCs based on the initial GC sample (based on HST); in Section 2.5 we comment on the background subtraction and necessary corrections; in Section 2.6 we explain the last steps essential for the calculation of the number of GCs per galaxy; in Section 2.7 we list several relations and equations used for investigation later in this work; in Section 2.8 we compare our number of GCs for the available HST galaxies to the work of Liu et al. [2019].

2.1 Sample

The sample of galaxies can be divided into two sections: a sample on which the GC selection is based and a sample containing the resulting dwarf galaxies of the FDS Survey. The complete FDS dwarf galaxy sample consists of 564 galaxies. Of these 564 galaxies, 24 galaxies were excluded through the analysis due to different issues and can be found in Appendix 9.

2.1.1 Sample for GC selection

At first, 21 bright dwarf galaxies have been selected which are available in both the FDS data and from Hubble Space Telescope (HST). HST data is deeper than the FDS data and has a high spatial resolution, which makes it possible to spatially resolve the GCs. In the FDS data it is not possible due to the contamination of the atmosphere and distance to the Fornax cluster. By comparing HST data with FDS data it is possible to determine the completeness of the observed globular clusters of the FDS data at least up to the globular cluster luminosity function (GCLF). The ACS data is complete to a g-magnitude of ~ 26.1 covering $\sim 95\%$ of the GCLF [Cote et al., 2004]. This comparison also enables us to determine trustworthy color criteria for the GCs. More specifically, the data is compared to work from Jordán et al. [2015] who used the Advanced Camera for Surveys (ACS) on board of the HST to find GCs as part of the ACS Virgo and Fornax Cluster Surveys [Cote et al., 2004; Jordan et al., 2007]. Jordán et al. [2015] has g- and z-band magnitudes for all the sources and half-light radii are obtained by fitting point spread function-convolved King models. These parameters are used to estimate a probability of an object being a GCs from 0 to 1, where the probability of an object being a GCs is denoted by p_{GC}. In this work, only the GCs with $p_{GC} > 0.75$ are considered.

A total of 21 galaxies are available in both data sets. Eventually, the galaxies FCC249 and FCC277 are not used because there was an improper gri-stacked image and too many bright foreground objects to obtain a good ellipse fit to model and subtract the galaxy's light. A list of the resulting 19 galaxies is visible in Table 6.

2.1.2 Sample of new galaxies

The sample of new galaxies consists of the resulting dwarf galaxies from the FDS catalog with a couple of exceptions (see Appendix 9). The coverage of the galaxies in this work can be seen in Fig. 7.
For the rest of this Chapter, the focus is on the sample for the GC selection.

target_name	galaxyn	RA_ICRS	DE_ICRS	PA	arat	reff	rmag1	rmag_fit	gmag_fit	reff_h
FDS26_DWARF141	19	50.5946	-37.3976	56.035999	0.432	16.62014	15.5847	14.578	15.2083	11.3
FDS19_DWARF001	55	51.8251	-34.5265	29.2062	0.4083	14.63574	13.9593	13.0425	13.8025	12.4
FDS17_DWARF227	90	52.7845	-36.2901	-49.521599	0.7507	8.08564	14.8555	14.0022	14.5505	6.9
FDS16_DWARF258	95	52.8534	-35.3309	-33.101501	0.787	14.53584	14.4511	13.6565	14.5505	12.26
FDS16_DWARF417	100	52.9485	-35.0514	78.330803	0.7567	19.77038	15.3737	14.5493	15.2866	16.3
FDS15_DWARF417	106	53.1987	-34.2387	-60.337299	0.4861	10.65222	15.0575	14.0861	14.736	8.1
FDS14_DWARF144	119	53.3919	-33.5714	45.655701	0.8527	13.97248	14.9157	14.1339	14.8053	12.6
FDS16_DWARF159	136	53.6228	-35.5465	-3.6786	0.8515	17.495899	14.5522	13.7403	14.5104	16.6
FDS16_DWARF002	143	53.7467	-35.1711	-57.3307	0.8542	9.81058	13.6765	12.851	13.515	9.5
FDS16_DWARF303	148	53.82001667	-35.26549444	84.075996	0.7311	26.9	18.3084	12.2496	12.652	13.4
FDS11_DWARF279	182	54.2263	-35.3747	-28.155899	0.961	9.6731	14.4018	13.6167	14.3925	9.8
FDS11_DWARF235	202	54.5273	-35.4399	-89.812698	0.592	13.28242	15.0506	14.1693	14.9055	9.5
FDS10_DWARF189	203	54.5382	-34.5188	-39.381302	0.5454	16.044941	15.4762	14.6089	15.2431	12.1
FDS9_DWARF000	204	54.5567	-33.1272	21.925301	0.3894	18.96818	14.8673	13.9771	14.6995	10.2
FDS4_DWARF001	255	55.265	-33.7791	-7.3199	0.4156	17.03438	13.6383	12.8435	13.4974	11.7
FDS4_DWARF002	288	55.8444	-33.9388	5.4268	0.2612	14.98094	15.4054	14.5661	15.2404	8.3
FDS7_DWARF000	301	56.2649	-35.9727	-23.357599	0.5368	7.60046	14.0541	13.1674	13.7919	9.3
FDS7_DWARF001	303	56.3087	-36.9367	-78.985802	0.9174	14.76926	15.3208	14.5409	15.164	12.9
FDS2_DWARF000	335	57.653	-35.9094	48.431301	0.5965	14.54166	14.356	13.5423	14.2127	11.6

Figure 6: The columns of the table represent the following properties: $target\_name$ is the name of the objects, $galaxyn$ is the FCC number given by Ferguson [1989]. Followed by the right accession (RA_{ICRS}) and declination (DE_{ICRS}), the position angle in degrees (PA), axis ratio and effective radius in $''$. $rmag1$ is the magnitude in the r-band within $1 \times Re_e$ and the parameters $rmag\_fit$ and $gmag\_fits$ represent the galaxy's magnitude obtained through Sersic fitting. The final column shows the effective radius from the work of Hamraz et al. [2019]. All the parameters are retrieved from Venhola et al. [2018a] unless stated otherwise.

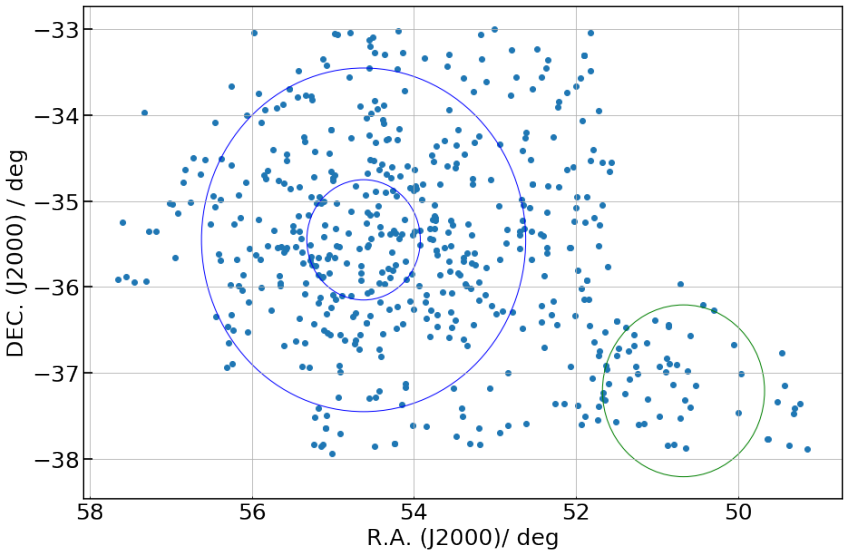

Figure 7: The coverage of the complete sample of dwarf galaxies in this work. The inner blue circle represents the core [Ferguson, 1989] and the outer the virial radius [Drinkwater et al., 2001] of the cluster its main galaxy NGC1399. The green circle has a one degree radius centered at the Fornax A subgroup NGC1316 [Drinkwater et al., 2001].

2.2 Data Reduction

The data from FDS is in the form of mosaic images with corresponding weight images. Even though the data is available in four bands u, g, r, and i, only the last three are exploited in this work. First of all, the u-band data is not available in all FDS tiles, it does not go deep enough and the seeing is in most cases higher than the other bands causing problems later on during the GC selection. Therefore every galaxy frame is taken in the g, r, i, and in the gri-stacked band, for identification purposes. For every galaxy, a frame is cut with a dimension of $15 \times R_{eff}$, based on the effective radius of the galaxy taken from Venhola et al. [2018b], and a bigger frame to have a higher number of stars around each galaxy of 15×15 $arcmin^2$ that will be referred to as the big galaxy frame. The smaller frame is used to determine the amount of GCs and the big galaxy frame for aperture correction. The detection of GCs in bright galaxies is not great and therefore the light of the galaxy needs to be modelled and subtracted. This ensures a better detection of the GCs that are on top of the galaxy. This is done in two different manners: 1) an elliptical model is constructed and subtracted using *IRAF* [National Optical Astronomy Observatories, 1999] and 2) a local background subtraction using Source Extractor [Bertin and Arnouts, 1996].

2.2.1 Modeling the galaxy

The first method is constructing an elliptical model using *IRAF*, which operates in the space telescope science data analysis system (STSDAS) [Hanisch, 1989]. The *isophote* package offers the function *ellipse* which fits several elliptical isophotes to a galaxy image. To obtain an optimal elliptical model all bright objects, such as large foreground stars, should be masked so they can not influence the model. The *ellipse* function takes initial guesses for the center of the galaxy, the position angle (PA) and the ellipticity. It is possible to vary the center coordinates, PA and ellipticity or to keep them fixed for every isophote. In most cases, all three parameters were allowed to vary to obtain a good fit. However, in certain cases the position angle was fixed to

avoid ellipse rings in the subtracted image. The *ellipse* function returns a table containing the information to fit elliptical isophotes to the galaxy at different radii. *Isophote* package also offers the task *bmodel*, which uses the output table from *ellipse* to create the photometric model of the galaxy. This model is subtracted from the original image utilizing the task *imarith*. In Fig. 8 an example is displaying the outcomes of different steps: the original image, the galaxy model and the subtracted image.

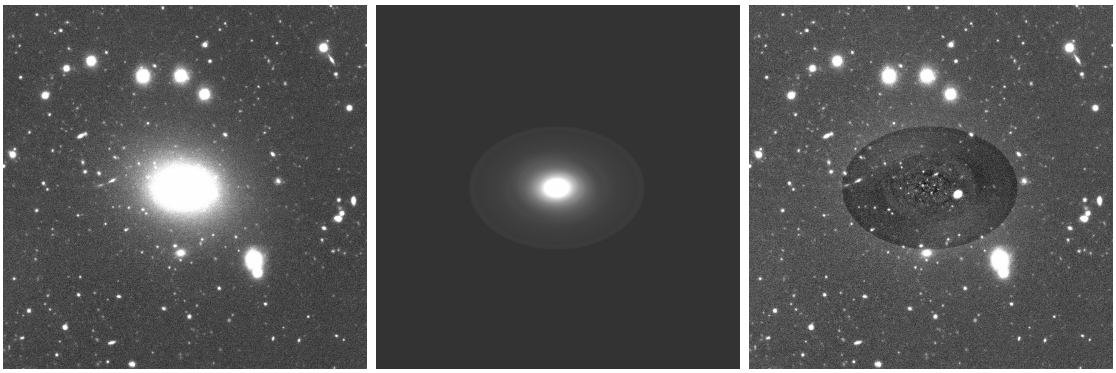

Figure 8: (a) Galaxy FCC100 gri-stacked image. (b) Model of the surface brightness of galaxy FCC100 produced by the functions *ellipse* and *bmodel*. (c) The subtracted image: (a) - (b). In the subtracted image objects within the galaxy become visible.

The second method is more robust and less time consuming than the first method. This is done by adjusting several parameters in the *default.sex* file of Source Extractor to subtract local background which directly returns the photometric values of the objects within the image frame. The parameters can be found in Table 1 where especially the choice of the mesh size ($BACK\_SIZE$) is important for an accurate background determination. The small mesh size will ensure that only local light is taken into account for the background subtraction. This method is not suited for very dense fields with many bright objects. Therefore, the largest part of the galaxies and the brightest galaxies ($M_r < -15\ mag$) are modeled using *ellipse*. To save time, the galaxies went first through SExtractor and the returned check images were controlled by eye to see if the background subtraction was successful. In the case of an unsuccessful subtraction, the galaxy light is still modeled with *ellipse* function and afterward run through SExtractor to find the sources. An example of the local background subtraction can be seen in Fig. 9.

2.3 Photometry

After the elliptical models are subtracted from the image frames in all the different bands and the stacked image, the images are given to Source Extractor [Bertin and Arnouts, 1996] to perform aperture photometry. Aperture photometry includes the summation of the pixel counts within a specified aperture size and the subtraction of the average close by sky count per pixel multiplied by the amount of pixels within the aperture. The gri-stacked frame is the deepest frame and is therefore used as detection frame while photometry is obtained from the separate bands. The big galaxy frames are directly given to SExtractor without any further reduction applied to determine aperture corrections and Δm normalization. During these runs, all the corresponding weight-images for the frames are also given to SExtractor. Several parameters of *default.sex* file are listed in Table 1, where *Normal* represents the parameters of the SExtractor

Figure 9: (a) Galaxy FCC242 g-band image. (b) The check image returned from SExtractor after applying local background subtraction.

runs for the subtracted frames and the big galaxy frames. Also, the parameters are shown for the runs with local background subtraction directly returning the objects with their photometric values. Afterward, the resulting objects in all three bands are matched based on their position within 0.1 *arcsec*.

Parameter	Normal	Local Background subtraction
DETECT_MINAREA	5	5
DETECT_TRESH	3.0	3.0
ANALYSIS_TRESH	3.0	3.0
DEBLEND_NTRESH	32	32
DEBLEND_MINCONT	0.005	0.005
BACK_TYPE	AUTO	AUTO
BACK_SIZE	64	8
BACK_FILTERSIZE	3	2
CHECKIMAGE_TYPE	NONE	-BACKGROUND

Table 1: SExtractor configuration parameters.

To be able to measure the light of the objects within the image through SExtractor, an aperture diameter size of 8 pixels ($1.6''$) is chosen. The flux of the objects is therefore only measured within a small finite aperture even though it is distributed over a larger area. However, taking a larger aperture size, leads also to more noise (low S/N pixels around an object) being measured. Therefore, we need to account for the flux from objects outside the 8 pixel aperture and this can be done by applying aperture correction. Aperture correction is the difference in magnitude of bright non-saturated stars measured between the used aperture size (8 pixels) and a larger aperture size, such as 50 pixels which measures roughly all the light of the source. The smaller the initial aperture, the larger the dependency on the correction factor. The aperture correction depends on the seeing of the fields. The seeing of the different fields can be quantified by the FWHM values, visible in Fig. 10.

2.3.1 Aperture Correction

FCC	FDS NAME	FWHM_g	cor_g	std_g	FWHM_r	cor_r	std_r	FWHM_i
19	FDS26_DWARF141	0.93	0.748	0.067	0.81	0.47384	0.019	0.91
55	FDS19_DWARF001	1.14	0.6231	0.015	0.89	0.50379	0.008	0.87
90	FDS17_DWARF227	1.11	0.9504	0.052	0.87	0.4909	0.023	1.01
95	FDS16_DWARF258	1.26	0.8303	0.009	0.94	0.61327	0.018	1.08
100	FDS16_DWARF417	1.26	0.7422	0.021	0.94	0.66901	0.026	1.08
106	FDS15_DWARF417	1.13	0.695	0.017	0.9	0.5169	0.007	0.97
119	FDS14_DWARF144	1.18	0.7441	0.01	0.96	0.61775	0.017	0.86
136	FDS16_DWARF159	1.26	0.871	0.056	0.94	0.8	0.064	1.08
143	FDS16_DWARF002	1.26	0.8203	0.014	0.94	0.68484	0.022	1.08
148	FDS16_DWARF303	1.26	0.8423	0.018	0.94	0.6474	0.036	1.08
182	FDS11_DWARF279	1.06	0.7656	0.012	1.09	0.84905	0.028	1.15
202	FDS11_DWARF235	1.06	0.7193	0.01	1.09	0.8393	0.051	1.15
203	FDS10_DWARF189	1.15	0.7503	0.013	1.02	0.57144	0.012	1.09
204	FDS9_DWARF000	1.2	0.797	0.082	0.97	0.6327	0.049	0.84
255	FDS4_DWARF001	1.39	0.9046	0.024	1.19	0.8112	0.017	0.7
288	FDS4_DWARF002	1.39	0.922	0.027	1.19	1.0365	0.069	0.7
301	FDS7_DWARF000	0.83	0.5169	0.01	0.95	0.59478	0.02	1.42
303	FDS7_DWARF001	0.83	0.597	0.007	0.95	0.53635	0.007	1.42
335	FDS2_DWARF000	1.35	0.6324	0.019	1.14	0.46261	0.028	0.79

Figure 10: The columns represent the FCC names (*FCC*) [Ferguson, 1989], followed by the FDS name (*FDS NAME*). The full width at half maximum values (*FWHM*) are given for all three bands in [arcsec] and are taken from Venhola et al. [2018b], which displays the average FWHM over the field. The corrections (*cor*) in all the three bands are in [mag] and represent the average of the difference in magnitude between the apertures of 8 pixels and 60 pixels from five stars around the galaxy. The standard deviations (*std*) of the mean correction of these five stars is also given in all three bands.

For bright and unsaturated stars the light profile should be the same and this can be used to create a correction for the missing light. For every galaxy is an aperture correction determined based upon five stars surrounding the galaxy. In most cases, there are not enough proper stars available in the 15×Re image and therefore the big galaxy frames, $15x15$ $arcmin^2$ around the galaxy center, are used to determine the aperture corrections. The coordinates of the galaxy centers are taken from Venhola et al. [2018a]. To ensure an optimal aperture correction, the stars should not be saturated so fainter than 16 mag. To find stars in the galaxies, all the acquired objects are cross-matched with GAIA DR2 [Gaia Collaboration et al., 2018] with $\frac{parallax}{parallax_{error}} > 5$ to assure that they are stars of point-sources within the Milky Way and to have accurate distance measurement. The stars should not have any objects close or bad pixels around, which can be ensured due to the parameter *FLAGS* returned by *SExtractor*, which gives basic warnings about the source extraction process so we take stars with *FLAGS=0*. Afterward, the stars are ordered based upon their g magnitudes and the five brightest objects are taken for the aperture correction. The aperture correction are based upon the curve of growth, which shows the magnitudes acquired for several consecutive aperture sizes taken up to a diameter size of 60 pixels. At an aperture size of 60 pixels, the curve of growth is already flat and seems to approach an asymptotic value. The difference in magnitude for consecutive apertures is visible in Fig. 11

for the five different stars. The apertures considered are in [pixels]: 4, 8, 10, 12, 16, 20, 30, 40, 50 and 60. The vertical axis is therefore displaying the difference in magnitude between on of the apertures above minus the aperture at 8 pixels. So the absolute magnitude difference between an aperture of 4 and 8 pixels is 1 mag. All the curves are combined in Fig. 12. The curve seems to reach an asymptotic value because not much light is added at larger apertures. To determine a correction factor for each band, the magnitude found at an aperture size of 60 pixels is subtracted from the magnitude found at an aperture size of 8 pixels. The correction factor is taken to be the average difference of magnitudes between aperture sizes of 8 and 60 pixels for these five bright objects. The correction values in magnitude for every band of the GC selection sample are shown in Fig. 10 denoted by cor_g, cor_r and cor_i and the standard deviation of the aperture correction is denoted by std_g, std_r and std_i. In general, the higher the seeing (FWHM) the higher the aperture correction value because more light will fall outside of the 8 pixel aperture.

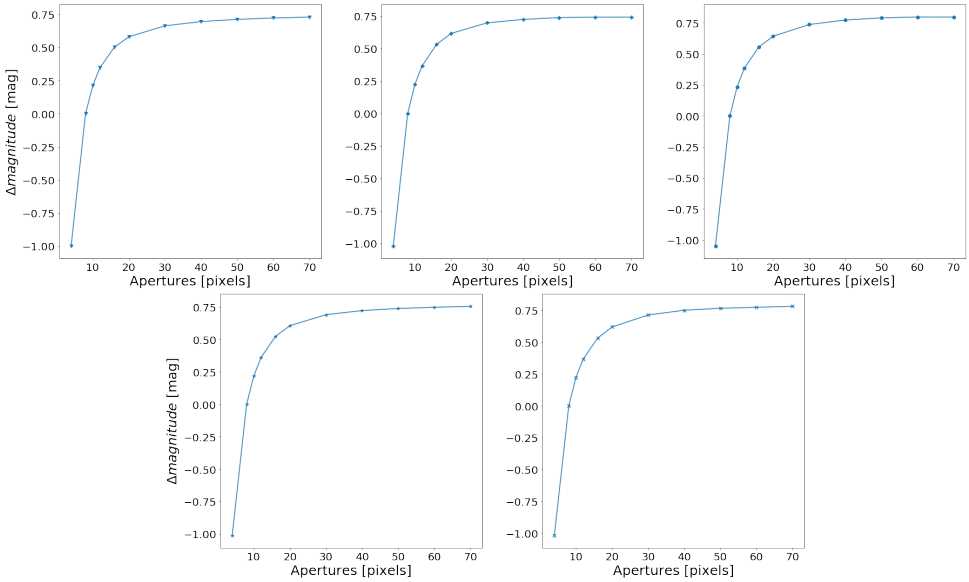

Figure 11: Curve of growth of five stars surrounding FCC 100 where the vertical axis is normalized for an aperture size of 8 pixels.

In Fig. 13 all the objects found by SExtractor with corrected g-band magnitudes are visible in blue and the GCs for these galaxies from Jordán et al. [2015] in red. Not all objects found are GCs, in fact only a small amount is and there is a strong decrease for objects $g > 25\ mag$ due to reaching the limit of the data set with a median g-band limit around $g \sim 25.6\ mag$ [Cantiello et al., 2020].

We have applied several checks to ensure the validity of the corrections and the resulting colors for the first 19 galaxies before applying this technique to any new galaxies. The first check is comparing the photometric values of this work to the photometric values of Jordán et al. [2015] and can give an indication for trustworthy corrections. To find the GCs in the FDS data, the sources are matched with the GCs of Jordán et al. [2015] based on their location within $1''$. Jordán et al. [2015] only contains data in the g- and z- band and therefore only the g-band data is compared directly. However, by applying a transition formula it is possible to go from $g_{ACS} - z_{ACS}$ to $g_{ACS} - i_{ACS}$. The formula is obtained from Hamraz et al. [2019] and is Eq.2.3.1:

$$(F475W - F814W) = 0.924(F475W - F850LP) - 0.027, \tag{2}$$

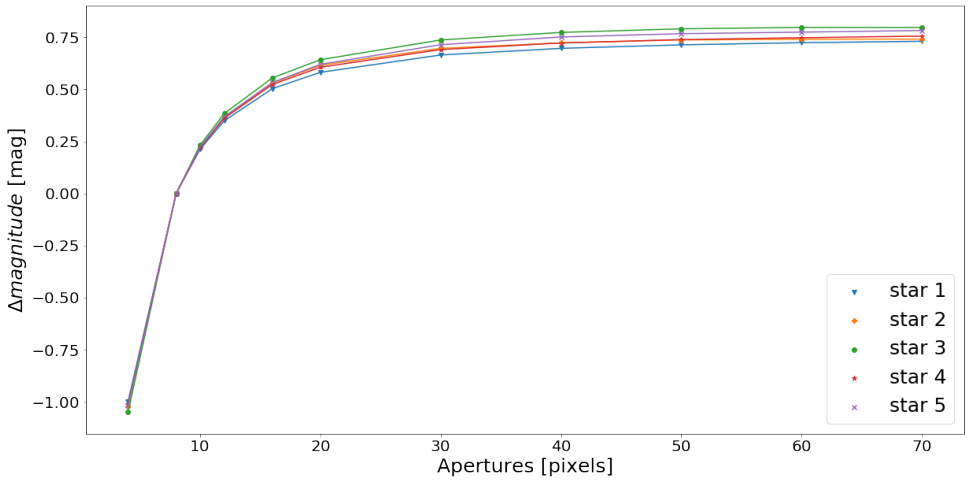

Figure 12: Combined curve of growth of five stars in surrounding FCC 100 where the vertical axis is normalized for an aperture size of 8 pixels.

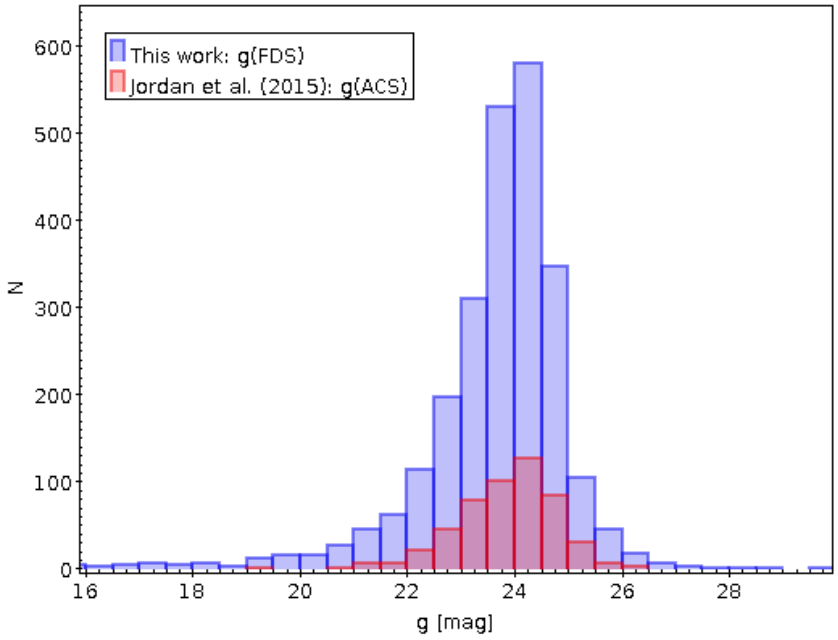

Figure 13: Histogram of the total amount of objects found within the sample for the GC selection (blue) and the number of GCs with $p_{GC} > 0.75$ from Jordán et al. [2015] (red).

where (F475W-F814W) corresponds to the g-i color.

In Table 2, we see the mean difference and standard deviation from Fig. 14 for different magnitude ranges after cleaning the data through sigma-clipping with $\sigma = 5$. The mean off-set is largest in the magnitude range $21 - 22$, however it has the smallest spread. In fainter regions, the average is closer to zero with increasing scatter and standard deviation between FDS data and HST values. The tables for the $g - i$ and $z - i$ comparisons can be found in Appendix 8.

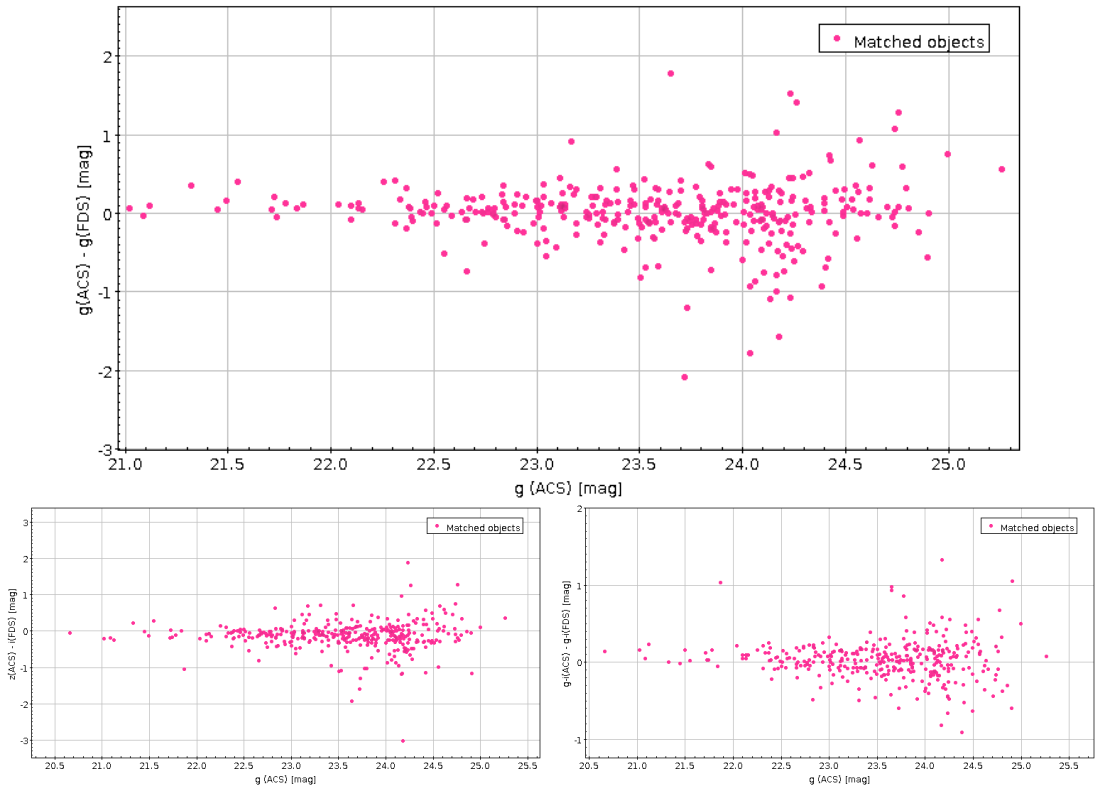

Figure 14: Photometric comparison between the magnitudes of this work and the work of Jordán et al. [2015]. All the data points are objects with $p_{GC} > 0.75$ [Jordán et al., 2015] and available in both data sets. All panels have the g magnitude from ACS on the horizontal axis. The upper panel shows a direct comparison between the g magnitudes. The lower left panel shows a comparison between z_{ACS} and g_{FDS}. The lower right panel shows a comparison between the g-i color. Eq.2.3.1 is used to transform $g_{ACS} - z_{ACS}$ to $g_{ACS} - i_{ACS}$.

Magnitude range	μ_g	σ_g	$\sigma_g/\sqrt{N}$
21-22	0.123	0.128	0.036
22-23	0.026	0.193	0.025
23-24	-0.004	0.277	0.022
24-25	-0.008	0.516	0.047

Table 2: The mean off-set, standard deviation and standard deviation divided by the number of objects per g magnitude range between the this work and the work of Jordán et al. [2015]. N is the number of objects per g magnitude range.

Another check is to implement the data into color-color diagrams based upon stars Covey et al. [2007]. For this comparison, only point sources are considered and these are selected based upon their FWHM shown in Fig. 15, where g_{auto} is the Kron-like [Kron, 1980] automated aperture magnitude returned directly from SExtractor. A horizontal trend is visible which is caused by the presence of point sources. These sources are selected by eye and are afterward compared to Covey et al. [2007] in Fig. 16. The shapes are similar to the data however the selected point sources have a larger spread.

The point source selection follows the shape of the stars nicely in Fig. 16, which suggests a

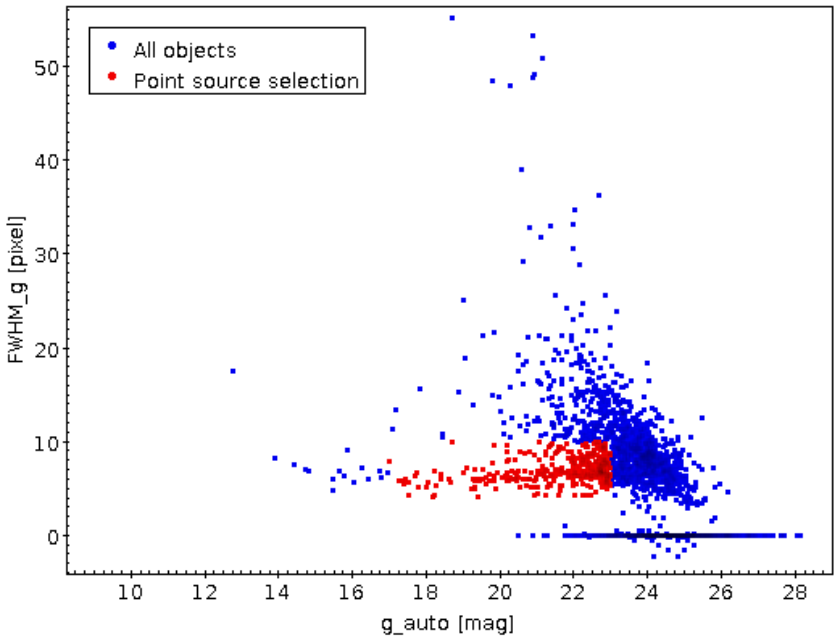

Figure 15: Full width half-maximum values of the g-band versus the Kron-like automated aperture in the g-band. The blue data points is the complete set of the first 19 galaxies. The red objects are the point source selection.

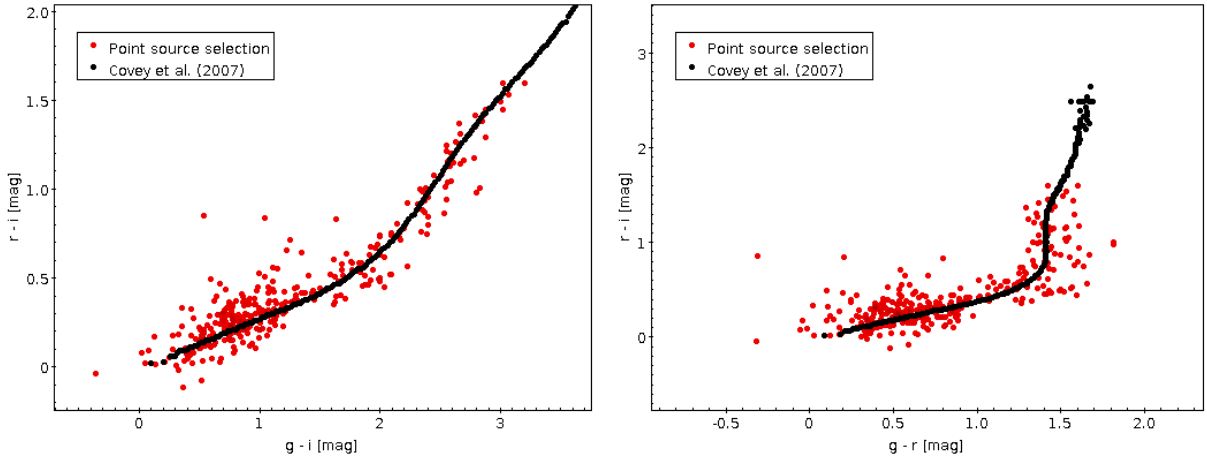

Figure 16: Color-color plots including point sources form this work compared to color-color relations for stars from Covey et al. [2007]

reasonable aperture correction.

Another check is directly comparing the photometric values to Cantiello et al. [2020]. This can be done by matching all the objects resulting from the first 19 galaxies to the data set of Cantiello et al. [2020]. These comparisons can be seen in Fig. 17

The mean differences from Fig. 17 in the g-band can be found in Table 3 and for the r- and i-band in Appendix 8. In all three bands, the mean in similar but especially the scatter is low in the bright region and larger in fainter regions. However, most of the values are in accordance with the values of Cantiello et al. [2020] which indicates valid aperture photometry.

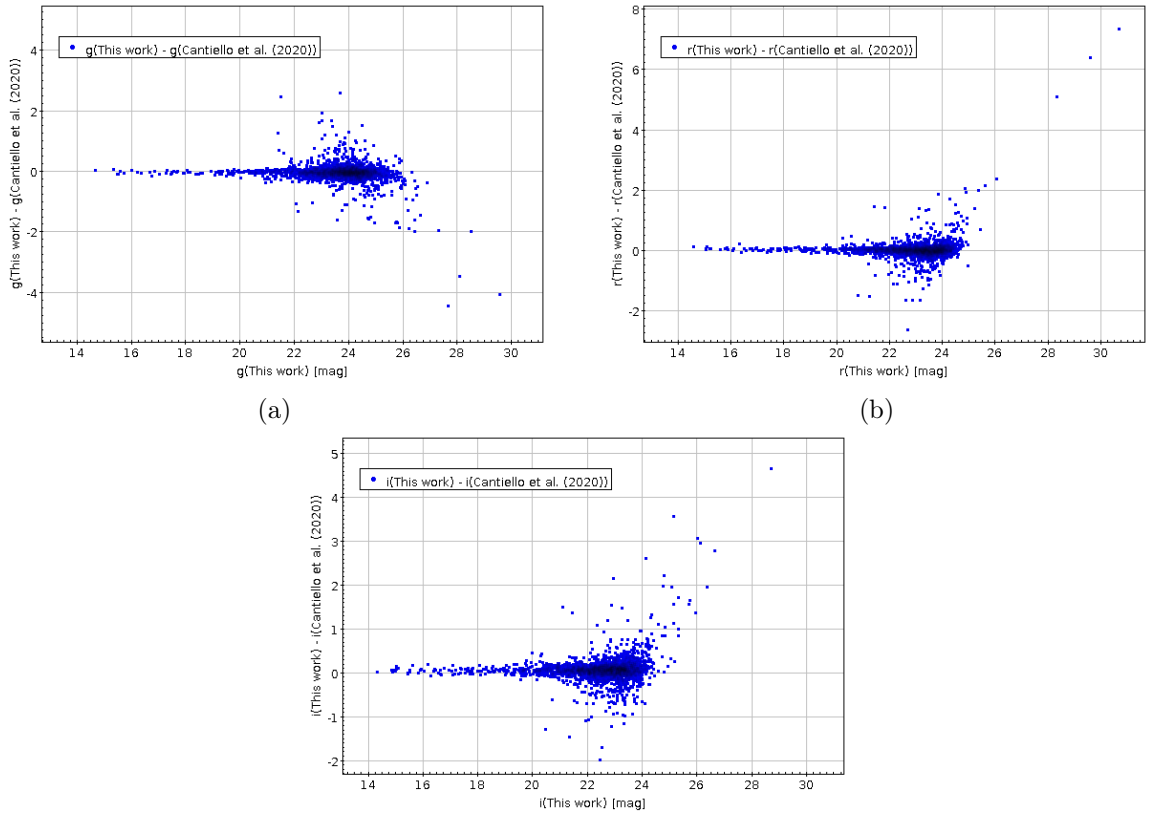

Figure 17: Direct photometric comparison with the work of Cantiello et al. [2020].(a) Shows the direct comparison of the g-band magnitudes for all available sources. (b) Shows the direct comparison of the r-band magnitudes. (c) Shows the direct comparison of the i-band magnitudes.

Magnitude range	μ_g	σ_g	$\sigma_g/\sqrt{N}$
21-22	0.059	0.100	0.010
22-23	0.062	0.153	0.008
23-24	0.055	0.168	0.006
24-25	0.024	0.219	0.007

Table 3: The mean off-set, standard deviation and standard deviation divided by the number of objects per g magnitude range between the this work and the work of Cantiello et al. [2020]. N is the number of objects per g magnitude range.

2.3.2 Compactness Correction

The Fornax Cluster is too far away to resolve GCs by their sizes and therefore another parameter is introduced [Peng et al., 2011; Beasley and Trujillo, 2016a]: the compactness index, which we will use to differentiate background galaxies from GCs. In this work, compactness is defined as the magnitude at an aperture of 4 pixels minus the magnitude at 8 pixels. Compact objects will add less light at a bigger aperture size and therefore have a small compactness value. However, larger objects like background galaxies will add more light at bigger apertures and therefore

have a larger compactness value. Even though a low compactness index means that objects are compacter than objects with a higher value, it is not exactly the same as the compactness of an object. Seeing also influences the compactness parameter, because a high seeing will increase the blurriness of the objects and therefore the objects will have a higher compactness. To make this compactness index independent of the atmospheric seeing, a normalization is applied in Eq. 2.3.2:

$$\Delta m_{norm} = \Delta m - \Delta m_{star}, \tag{3}$$

where Δm_{star} is the mean compactness of stars (point sources) within the big galaxy frames of the galaxy. The stars are selected in the same field and manner as the stars for the curve of growth.

2.4 GC selection

The GC selection criteria are based upon 19 galaxies of which the GCs are already known due to Jordán et al. [2015]. The GCs that are found in both Jordán et al. [2015] and in the FDS data are referred to as known GCs and all the objects found in these 19 galaxies are referred to as the complete data set. First of all, all the data is split according to their g-magnitude into bins of 1 magnitude starting at a g magnitude of 21. The apparent magnitude limit of $g = 21\ mag$ ($M_g = -10.5\ mag$) is taken as a separation criteria between GC and ultra-compact dwarf galaxies (UCDs) [Mieske, S. et al., 2004; Hilker et al., 2007; Saifollahi et al., 2021]. In Table 4 the number of GCs and the complete data set per magnitude are shown.

Magnitude range	N_{GC}	$N_{complete\ data\ set}$
$21 - 22$	15	107
$22 - 23$	69	312
$23 - 24$	153	841
$24 - 24.5$	64	581
$24.5 - 25$	33	347

Table 4: Number of GCs per magnitude bin in the first 19 galaxies.

The GCs are selected per magnitude bin based upon their colors $g - r$ and $r - i$ and their compactness value. In this 3d space, the data is selected which falls within a convex hull of the GCs data. The convex hull of the GCs data is the smallest convex polygon that contains all the data and an example of a convex hull can be seen in Fig. 18a.
To minimize the contaminants, only a selection of GCs are used for the convex hull. We want to include all the points that are closest to the densest GC date in 3d. The distance to the densest regions depends on the unknown photometric errors in the points and therefore the selection is established using a special method, namely Kernel Density Estimation (KDE).

2.4.1 Kernel Density Estimation

Density estimation is focused on reproducing the density function based on a given data set. KDE is a non-parametric method for the estimation of the probability density function of random variables. Therefore KDE works for uni- and multi-variate data. The kernel density estimator

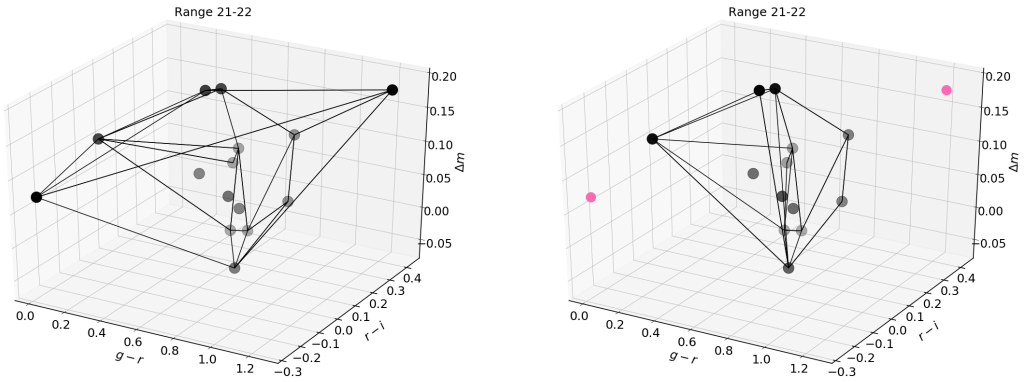

(a) (b)

Figure 18: Left panel: Convex hull in 3d considering all the available GCs in the magnitude range $21-22$ mag. The 3d parameters are consisting of 2 colors $g-r$, $r-i$ and the compactness Δm. Right panel: Convex hull in 3d only considering a part of the available GCs to decrease the amount of contamination in the magnitude range $21-22$ mag. If new sources are contained within the convex hull, they will be considered a GC.

is given by Eq.4:

$$\hat{f}_h(x) = \frac{1}{nh} \sum_{i=1}^{n} K\left(\frac{x - x_i}{h}\right), \tag{4}$$

where K is the kernel function, h is the bandwidth and n is the number of data points. It is possible to use several types of kernels and in this work only the Gaussian kernel is considered. For every data point from the given data, a normal distribution is drawn where the variance is equal to the bandwidth. A low bandwidth means that only very close points to the considered points are given weight, while with a high bandwidth a larger amount of surrounding points are given any weight. Therefore the bandwidth is important for the smoothness of the density function. In this work the statistical function *gaussian_kde* is used within the Python−based ecosystem SciPy [Virtanen et al., 2020], which includes a bandwidth estimator. The default estimator is Scott's Rule [Scott, 2015]. This is implemented by computing a coefficient, Scott's factor. By multiplying this coefficient with the standard deviation of the sample, the bandwidth is calculated visible in Eq.5

$$h = \sigma_{sample} \times n^{-1./(d+4)}, \tag{5}$$

where n is the number of data points and d the number of dimensions. The optimal bandwidth choice is the one that minimizes the mean integrated squared error. This bandwidth estimator works well for uni-modal distributions while multi-modal distributions will likely be over smoothed.

2.4.2 KDE application

For every magnitude range KDE is applied in 3d ($g-r$, $r-i$ and Δm) parameter space. Therefore at locations in 3d space where more data points (GCs) are located, the estimation of the probability will be higher than a region where almost no data points are found. So KDE returns the probability of a random data point being located at a certain position. Because the GCs are

selected based on a convex hull, it is important to keep the contamination low. Therefore, the known GC data is ordered from highest to lowest KDE probability. By considering all available GCs in a magnitude range, the contamination will also be much higher. KDE makes it possible to filter out the outliers and therefore decrease the amount of contamination. The minimum amount of data points necessary is 4 to be able to create a convex hull in 3d space. As an example, the magnitude range 21-22 is considered which contains a total of 15 GCs. However, if all these 15 points are used to create the convex hull, 25 data points are found within the convex hull from the complete data set. This means that 10 objects are selected which are no GCs. However, if we do not consider the lowest KDE probability point and only regard 14 data points for the convex hull creation, 17 data points are selected from the total data sample. By neglecting this outlier, the contamination also decreased from ten to three data points.

In Fig. 19, the selected objects from the total data sample are shown for every possible number of GCs considered to create the convex hull. Therefore, the horizontal axes starts at four and these data points are located in the densest region. In general, the right side of the figures show steeper slopes and therefore a higher contamination level. In Fig. 18, an example is shown for the magnitude range 21-22 wherein the left panel all 15 GCs are taken for the convex hull whereas in the right panel only 13 are considered. From these figures, we have selected the number of GCs in such a manner to still utilize over 80% of the GC data set while reducing the contamination level. The final number of GCs considered for the convex hull creation is indicated by the red lines and these convex hulls are used for further GC selection. In Fig. 18b the final convex hull for the g range of $21-22\ mag$ is shown, where the pink data points are not considered for the convex hull decreasing the contamination level.

In Table 5 the number of initial GCs (N_{total}), the number of GCs considered for the convex hull (N_{selec}), and the number of objects found in the total sample of the first 19 galaxies ($N_{select\ total\ sample}$) for every magnitude range are listed.

Magnitude range	N_{total}	N_{select}	$N_{select\ total\ sample}$
$21-22$	15	13	15
$22-23$	69	60	71
$23-24$	153	131	211
$24-24.5$	64	47	76
$24.5-25$	33	18	35

Table 5: The number of initial GCs (N_{total}), the number of GCs considered for the convex hull (N_{selec}), and the number of objects found in the total sample of the first 19 galaxies ($N_{select\ total\ sample}$) for every magnitude range.

2.5 Background subtraction and corrections

Selecting GCs based on their colors and Δm entails contamination of foreground stars and background galaxies. Many foreground stars have $g < 21\ mag$ and are therefore partly already selected out. However, this still leaves contamination from background galaxies and fainter foreground stars. To investigate the contamination in the selection, several larger fields of $15 \times 15\ arcmin^2$ including both emptier and denser fields, to take into account the intra-galactic GCs [Cantiello et al., 2020], are taken. These field are also going through the same selection

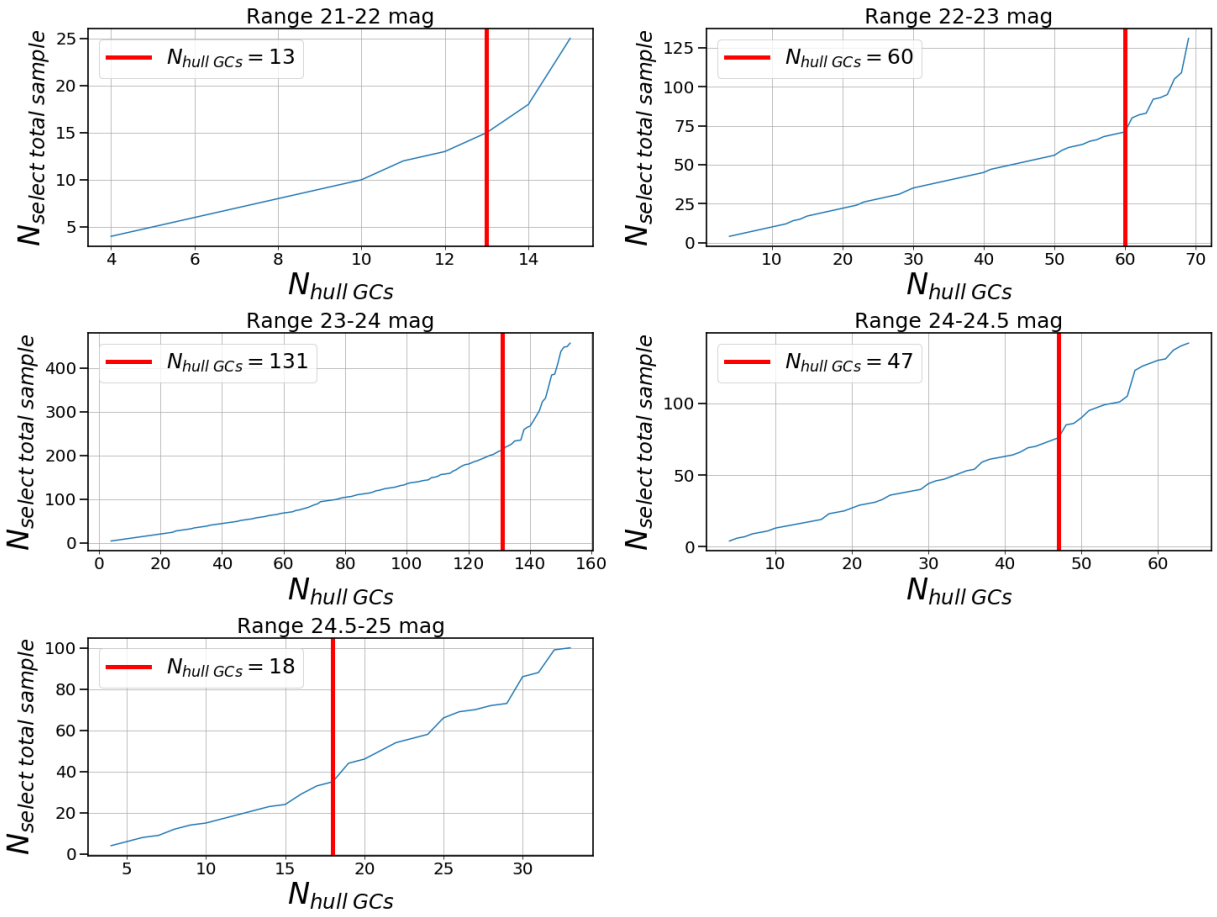

Figure 19: Number of globular clusters used for the creation of the convex hull with the corresponding number of objects found in the complete data set.

procedure. This was eventually done for 75 frames of different fields and the average luminosity function (LF) of the resulting selection of objects is divided by the total area of 225 $arcmin^2$. This results in a number of contaminating objects per magnitude bin per area. In Fig. 20 the LF of the background contamination per area is showing low contamination in the bright region ($g : 21 - 23\ mag$) and higher contamination in the fainter regions ($g : 23 - 24.5\ mag$). The faintest magnitude ranges ($g : 24 - 25\ mag$) have a lower number of contamination due to the high amount of objects discarded for the selection. This results in a lower contamination, but in a higher correction factor which is clarified in the next paragraph. For every galaxy, the amount of background can be determined by multiplying this LF with the area of the galaxy.

For the determination of GC in a galaxy we consider a radius of $3 \times R_{eff}$. It is not exactly known within what radius the GCs are part of the galaxy and this also depends on the size of the galaxy. For certain comparisons, we have also considered a radius of $5 \times R_{eff}$, which in general decreases the S/N due to the higher amount of background objects. In Fig. 21 an example is shown of $3 \times R_{eff}$ area for galaxy FCC100. The center, ellipse parameters, and R_{eff} are taken from Venhola et al. [2018b] and are visible for the first 19 galaxies in Fig. 6. The area of the ellipse can be calculated by πab, where a and b are respectively the semi-major and minor axis of the ellipse. This area is then multiplied by every bin of the LF of Fig. 20 to determine the amount of contamination per galaxy and subtracted from the globular cluster luminosity function (GCLF) from the galaxy. The GCLF shows the number of CGs per magnitude bin. An

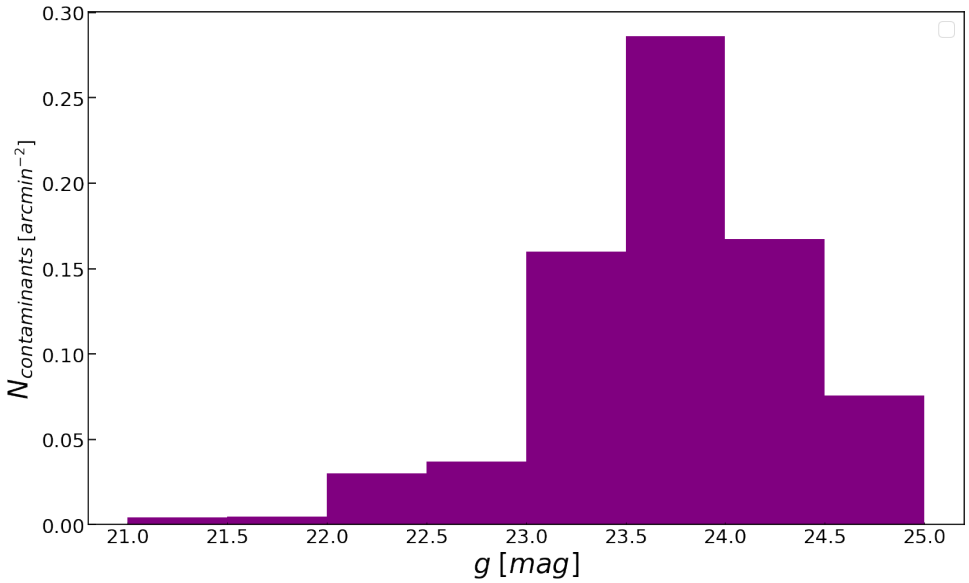

Figure 20: Number of contaminants per area per magnitude bin.

example of the initial GCLF within $3 \times R_{eff}$ can be seen in Fig. 22 (a) and after the subtraction of the background (b).

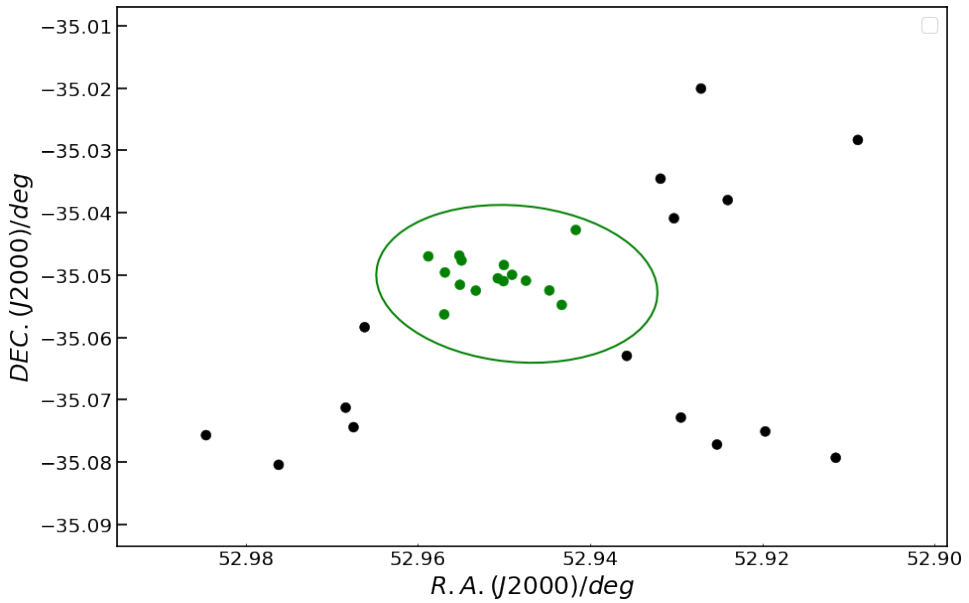

Figure 21: Locations of all the GCs found in the frame of FCC 100. The points within the green ellipse are the GCs within $3 \times R_{eff}$.

To take into account the missing GCs two corrections are considered: completeness and selection correction. The completeness selection is calculated per magnitude range and accounts for the GCs that are not found or matched with the GCs of Jordán et al. [2015]. The selection correction is accounting for the GCs that are disregarded, to reduce the amount of contamination in the GC sample, during the creation of the convex hulls. These corrections are calculated

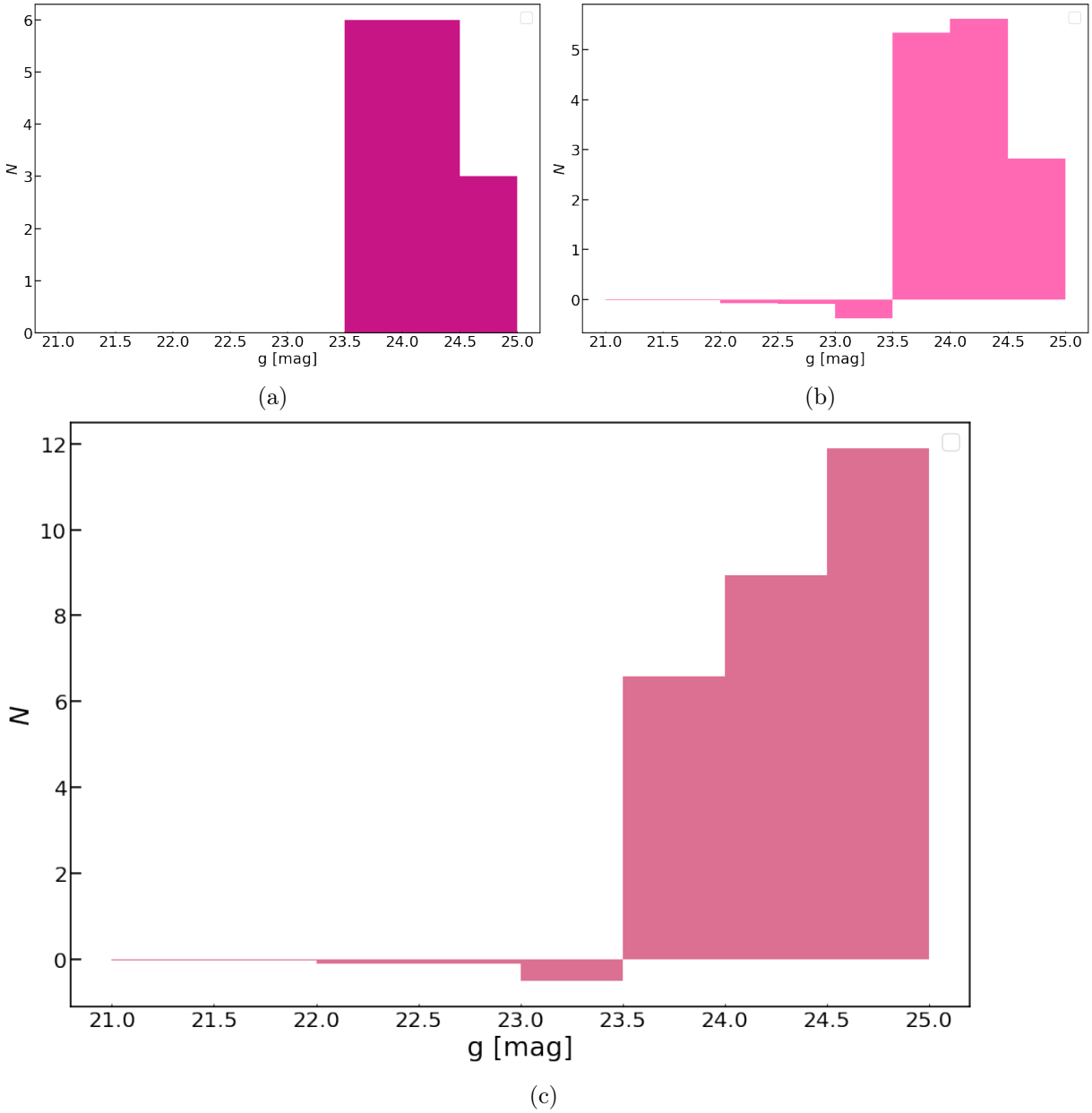

Figure 22: (a) Initial GCLF within $3 \times R_{eff}$ of FCC 100. (b) GCLF with background subtracted. (c) GCLF with background subtracted and correction factors applied.

by dividing the number of missing objects by the total amount of objects used, in the case of the selection correction, or found, in the case of the completeness selection, in a specific magnitude range. For the calculation of the completeness correction, certain galaxies have not been considered to avoid overcompensation. These were galaxies with an edge-on view or another bright galaxy close which leads to an improper elliptical model and eventually more missing GCs. This is the case for the galaxies FCC55, FCC255, FCC202, and FCC148. In the left panel of Fig. 23 the incompleteness per magnitude bin per galaxy is shown for all the 19 galaxies. From this Figure, it can be seen that the four galaxies mentioned above have a higher incompleteness compared to the other galaxies. The galaxies eventually used for the completeness correction are visible in the right panel. In the magnitude range from 21-23 all GCs are found and at fainter

magnitudes the number of missing GCs is increasing. At magnitudes fainter than 26 almost no GCs are found anymore and therefore only a magnitude range of 21-25 is considered and corrected for.

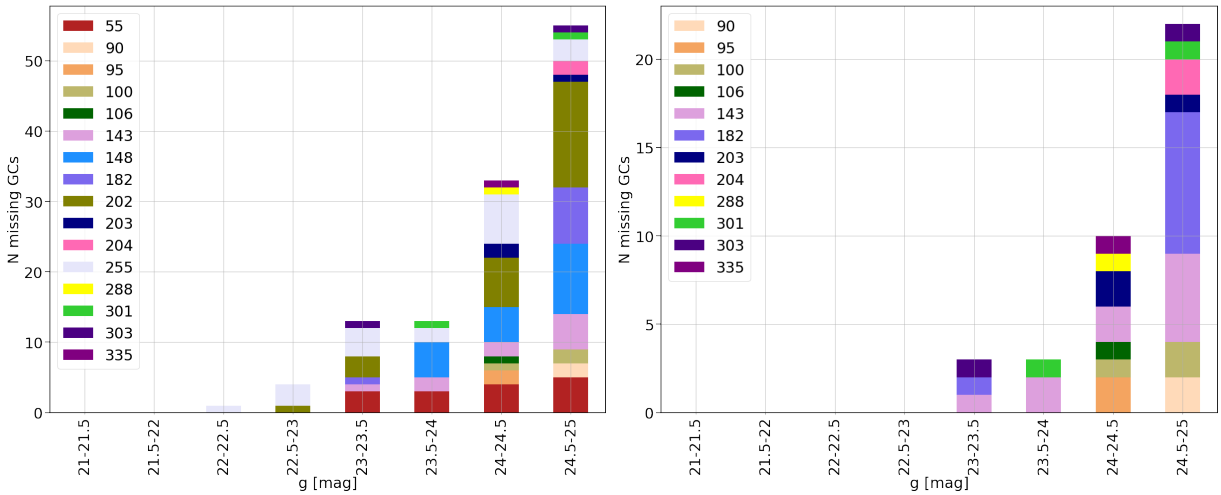

Figure 23: Number of missing GCs compared to Jordán et al. [2015] per magnitude bin. Left panel: all of the galaxies with missing GCs are shown. Right panel: Selection of galaxies used to calculate the completeness correction.

The completeness correction is calculated by counting the amount of matched GCs and dividing this by the total amount of GCs from Jordán et al. [2015] in the same galaxy frame. To turn this into a correction factor one is appended to be able to directly multiply it with the found selection. The selection correction is calculated by the number of GCs used for selection divided by the total number of GCs available per magnitude bin plus one to turn it into a factor. The GCLF of every galaxy is multiplied by both the correction as a selection factor presented in Table 6 and an example of a final GCLF is shown in the right panel of Fig. 22

Magnitude range	Completeness correction	Selection correction
$21 - 21.5$	1	1.1538
$21.5 - 22$	1	1.1538
$22 - 22.5$	1	1.15
$22.5 - 23$	1	1.15
$23 - 23.5$	1.1071	1.1679
$23.5 - 24$	1.0577	1.1679
$24 - 24.5$	1.1695	1.3617
$^{*}24.5 - 25$	2.2941	1.8333

Table 6: The correction factors at every magnitude range. The completeness correction is based on the amount of GCs found within a specific area by Jordán et al. [2015] and how many of those GCs are also found in this work. The selection correction is based on the amount of GCs disregarded for the convex hull, which is explained in Section 2.4. * The correction factors in this magnitude range are not used because we only consider the number of GCs until the GCLF peak of 24.5 *mag*.

2.6 Number of GCs

A common method for establishing the final number of GCs for a galaxy is by summing the different magnitude bins up to a magnitude of the GCLF peak, which is in the case of Fornax at a g-band magnitude of 24.5 and multiplying this by 2 to account for the GCs at the faint end of the GCLF [Harris and van den Bergh, 1981]. Due to the background subtraction and the correction factors, the final GC numbers are not integers.

2.6.1 Uncertainties

Many factors play a role in the determination of the number of GCs. Therefore, many different types of uncertainties are encountered. In this thesis only Poisson errors are considered, which represents the error caused by stochastic processes in nature. After selecting the number of GCs within a radius of $3 \times R_{eff}$, the error in the number of GCs in every bin is: $N_{GC,error/bin} = \sqrt{N_{GC}}$, where N_{GC} is the number of GCs in every bin. To take into account the uncertainty from the background subtraction, the standard error from Fig. 20 is defined as:

$$\sigma_{ctmn.\ normalized/bin/} = \frac{\sigma_{ctmn./bin}}{\sqrt{N_{bin}} * 225}, \tag{6}$$

where $\sigma_{ctmb./bin}$ is the standard deviation of the contamination bin including all contaminating objects found in 75 fields. N_{bin} is the total number of objects in that bin and 225 is the normalization for the total area of the 15×15 $arcmin^2$ fields. Afterward, the steps that are applied to calculate the final number of globular clusters are also taken into account when calculating the uncertainties. The new uncertainty after the background subtraction is: $\sqrt{N^2_{GC,error/bin} + \sigma^2_{ctmn.\ normalized/bin}}$. The correction and selection factor are then multiplied with this uncertainty per bin. The last step is to sum up the number of GCs to a g-magnitude of 24.5 and multiply this value with 2. For the uncertainty propagation this means: $N_{GC,error} = (\sqrt{N^2_{GC,error\_bin1} + N^2_{GC,error\_bin2} + ...}) \times 2$, where $N_{GC,error\_bin1}$ is the error including the background subtraction and corrections.

2.6.2 Background subtraction

Throughout this work, we have subtracted a background which was based on an average of 75 fields spread over the complete FDS, an averaged background subtraction. These fields include a variety of densities and therefore a variety in the amount of background or intergalactic GCs. However, the work of Cantiello et al. [2020] showed that the Fornax cluster contains regions with a higher density of intergalactic GCs. These regions can be seen in Fig. 24, where especially the center field has a very high density of GCs due to the central galaxy of the Fornax Cluster. Therefore the averaged background subtraction used in this work might underestimate the number of GCs in these regions, while the background subtraction for galaxies in the outer regions might be overestimated. To investigate these effects of the different backgrounds, we have calculated the number of GCs for all the galaxies using local background subtraction. This means the GCs within a specific radius, such as $3 \times R_{eff}$ or $5 \times R_{eff}$, are considered as the GCs of the galaxy and all the other GCs found in the galaxy image are used to construct the background LF. The background LF from the resulting objects is normalized by the complete area of the image.

In Fig. 25, the difference in number of GCs between local and averaged background subtraction versus the absolute r-band magnitude is shown for different effective radii. The upper

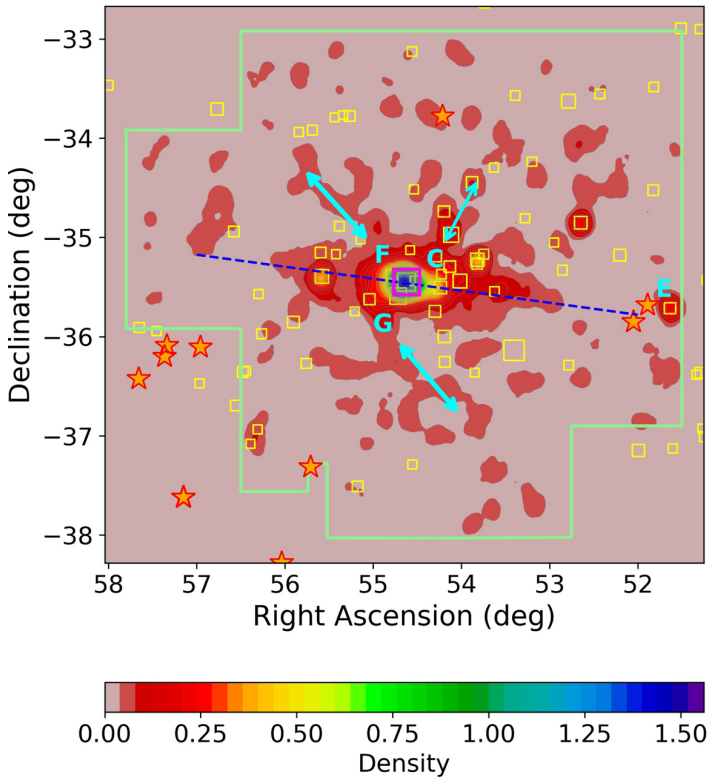

Figure 24: GC distribution in the Fornax Cluster, where the density is the number of GC candidates per $arcmin^2$. For further info about the several markers and arrows see the original figure in Cantiello et al. [2020].

left panel shows the difference in number considering $5 \times R_{eff}$ which is in good agreement for the fainter galaxies but has several outliers in the bright region. In the right corner panel, we have added the field number where the galaxy is located in and their error bars. In Fig. 5, the complete FDS sample is visible including all the field numbers. The central field is field 11 and contains also most outliers. The difference in number of GCs is caused by the lower amount of objects when using local background subtraction. Due to the high number of GCs in the background in the central field [Cantiello et al., 2020] it is logical that the strongest effect is in Field 11 and at other locations where the density is higher. When we take a smaller radius to count the GCs within a galaxy, we obtain the two lower rows from Fig. 25. The middle row shows $3 \times R_{eff}$ and the lower row shows $2 \times R_{eff}$, which already shows a decrease in the difference. The outliers remain but the difference in number of GCs increases more for smaller radii. This effect is mostly observed for bright galaxies because the GCs in the the brighter galaxies are more spread over the galaxy and many more will already be observed within a $5 \times R_{eff}$ radius than in for example a $2 \times R_{eff}$ radius. The biggest differences are found within the main field while in the other fields the difference in the number of GCs due to local background subtraction is not as high compared to averaged background subtraction. In these cases, the preference goes to the averaged background subtraction due to the better statistics obtained and no opportunities to have an over-subtracted background due to a larger dwarf galaxy close by which might enter more objects in the field but not necessarily in the galaxy region itself. An example of such a situation is with the galaxies FCC 47 and FCC 48. One side of the field of FCC48 is including many GCs from the larger galaxy FCC47 and therefore the local background subtraction will

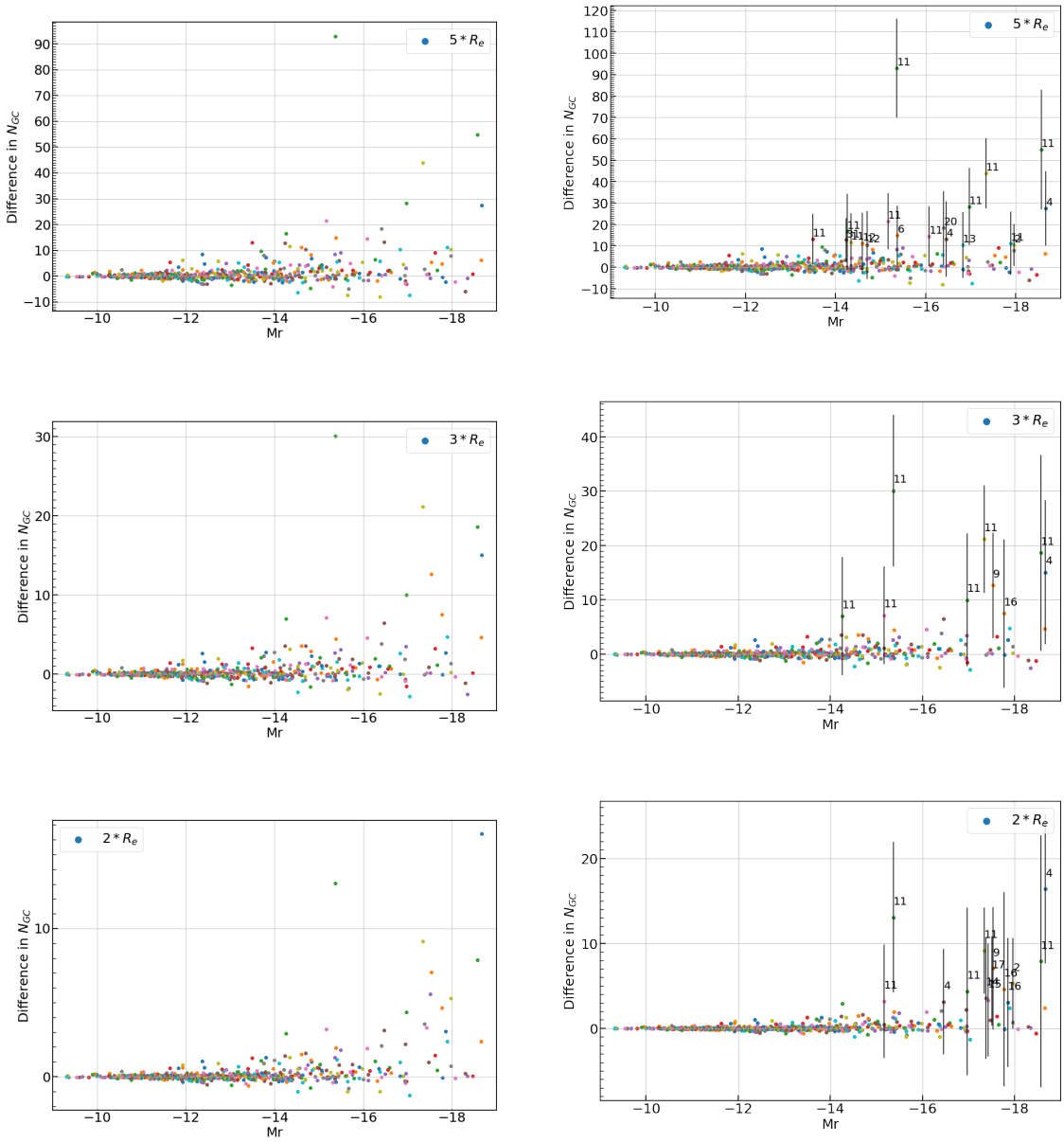

Figure 25: Difference in number of GCs between local background subtraction and averaged background subtraction versus the absolute r-band magnitude. The difference is taken as: $N_{GC,averaged\ background} - N_{GC,local\ background}$.

be high, even though the pollution within the $3 \times R_{eff}$ radius is not as high anymore as at the outskirts of the image. These situations can lead to underestimating the number of GCs with local background subtraction. To improve the use of local background subtraction, it is good to only consider the objects from for example $5 \times R_{eff}$ till $25 \times R_{eff}$, which is also used in for example Carlsten et al. [2021a], to increase the statistics and decrease the effects just described.

An important difference between the two subtraction methods is the uncertainty. An advantage of the averaged background subtraction is the statistics behind compared to local background subtraction. In Table 7, the uncertainty for both methods are given per $arcmin^2$. Where σ *averaged* is the standard error in the local background subtraction calculated from Eq. 2.6.1

and μ *local* is calculated by taking the mean of $\sqrt{N_{normalized}}$ for all the magnitude bins of fields that have a contamination values, where $N_{normalized}$ is the number of contaminants in the local field per $arcmin^2$. The mean of the local background subtraction is including the magnitude bins with 0 objects and therefore also no error to be consistent with the uncertainty calculations of the averaged background field. As expected, the uncertainties in the local background subtraction are much larger than the averaged background subtraction.

Magnitude range	σ *averaged*	μ *local*
21-21.5	0.0005	0.0120
21.5-22	0.0004	0.0194
22-22.5	0.0019	0.0719
22.5-23	0.0021	0.1130
23-23.5	0.0059	0.2644
23.5-24	0.0105	0.3779
24-24.5	0.0097	0.2940
24.5-25	0.0054	0.1885

Table 7: The uncertainties for different magnitude ranges of the averaged and local background subtraction normalized per $arcmin^2$. The uncertainty in the averaged background subtraction (σ *averaged*) is calculated from Eq. 2.6.1. The uncertainty in the local background subtraction is determined by taking the mean of the $\sqrt{N_{normalized}}$, which is the number of contaminants in the local field per $arcmin^2$.

2.7 Specific frequency and the Dark Halo Mass

Once the number of GCs is known per galaxy, it is possible to calculate several parameters such as the specific frequency (S_N), the specific mass frequency (T_N) and the dark matter halo mass for every galaxy.

The specific frequency is defined as the number of globular clusters per unit of V-band luminosity with a normalization of a galaxy of $M_V = -15$ [Harris and van den Bergh, 1981]. The relation for the specific frequency is given below in Eq.7:

$$S_N = N_{GC} \cdot 10^{0.4(M_V+15)}, \tag{7}$$

where M_V is the absolute magnitude in the V-band giving an indication of the stellar mass. However, the FDS data only offers the bands g, r, i and u. Therefore, M_r will be used for the physical interpretation and M_V to compare to other works. To obtain M_V a formula from Jester et al. [2005] is used, which is intended for stars but is also applied to galaxies because no more suitable transformation is available. Also, V lies between g and r, so this transformation is very accurate. This formula is shown below in Eq. 8:

$$M_V = M_g - 0.58 \times (g - r) - 0.1, \tag{8}$$

where M_g and M_r the absolute magnitudes calculated from the apparent magnitude obtained by Sersic fitting from Venhola et al. [2018b]. They used GALFIT [Peng et al., 2002, 2010] and the r-band images from the FDS. A distance modulus of 31.51 is assumed throughout this work [Blakeslee et al., 2009]. In cases where M_r is used, Eq. 7 is still applied but with a normalization factor of $M_r = 15$.

Another important feature of a galaxy is its stellar mass, which is inferred in this work through observed colors and the mass-to-light ratio in the same manner as Venhola et al. [2018b]. The original formula is defined by Taylor et al. [2011] and seen in Eq. 9:

$$log_{10}(\frac{M_*}{M_\odot}) = 1.15 + 0.070 \times (g-i) - 0.4M_i, \tag{9}$$

where M_i is the absolute i-band magnitude which is not determined in the work of Venhola et al. [2018b]. The Seŕsic model fitting was done for the r-band images and therefore they have adapted the formula above to Eq. 10:

$$log_{10}(\frac{M_*}{M_\odot}) = 1.15 + 0.070 \times (g-i) - 0.4M_r + 0.4 \times (r-i), \tag{10}$$

where the colors are measured within one effective radius R_{eff}.

We will also take a look at the correlation between the stellar mass and the specific mass frequency [Zepf and Ashman, 1993], T_N. The specific mass frequency is defined in Eq.11:

$$T_N \equiv N_{GC} \cdot 10^9 M_\odot / M_*. \tag{11}$$

The catalog of Venhola et al. [2018a] does not include the surface brightness for the dwarf galaxies. So to investigate the relation between the surface brightness and the number of GCs, the surface brightness is determined using Eq. 2.7:

$$\mu_r = r_1 + 2.5 \times log_{10}(R_{eff}^2 \cdot \frac{b}{a} \cdot \pi), \tag{12}$$

where r_1 is the magnitude measured within $1 \times R_{eff}$ and $\frac{b}{a}$ is the axis ratio. These values are directly taken from the catalog and the surface brightness is calculated in $[mag/arcsec^2]$.

Finally, the dark matter halo mass can also be determined based on relations from Harris et al. [2017]. The total GCs mass is given by $M_{GCS} = N_{GC}\langle M_{GC}\rangle$, which can be divided by η_M, the mass ratio, to obtain the dark matter halo mass. For dwarf galaxies we can take a mean GC mass of $1.0 \times 10^5 M_\odot$ and $\eta_M = 2.9 \times 10^{-5}$ [Harris et al., 2017] to obtain the relation visible in Eq. 13:

$$M_{halo} = N_{GC} \times 3.14 \cdot 10^9 M_\odot. \tag{13}$$

2.8 Validity

The work of Liu et al. [2019] continued with the data and GC selection from Jordán et al. [2015]; Villegas et al. [2010]; Cote et al. [2004]; Peng et al. [2008]. The work of Liu et al. [2019] calculated the number of GCs for the available galaxies in the Fornax cluster considering all GCs with $p_{GC} \geq 0.5$ and investigated the specific frequency of the GCs. They order the GCs based on their galactocentric distances. In Fig. 26 a direct comparison is made between the number of GCs of this work and from Liu et al. [2019] including the error. The blue line describes a one-to-one correlation.

Liu et al. [2019] considers GC with $p_{GC} \geq 0.5$ and select only GCs that are brighter than 1σ of the mean of the GCLF [Villegas et al., 2010]. They consider the same background correction for all the galaxies based on 16 control fields. To determine the GCs that are part of the galaxy, they order the GC based on their distance to the center of the galaxy and they add a number

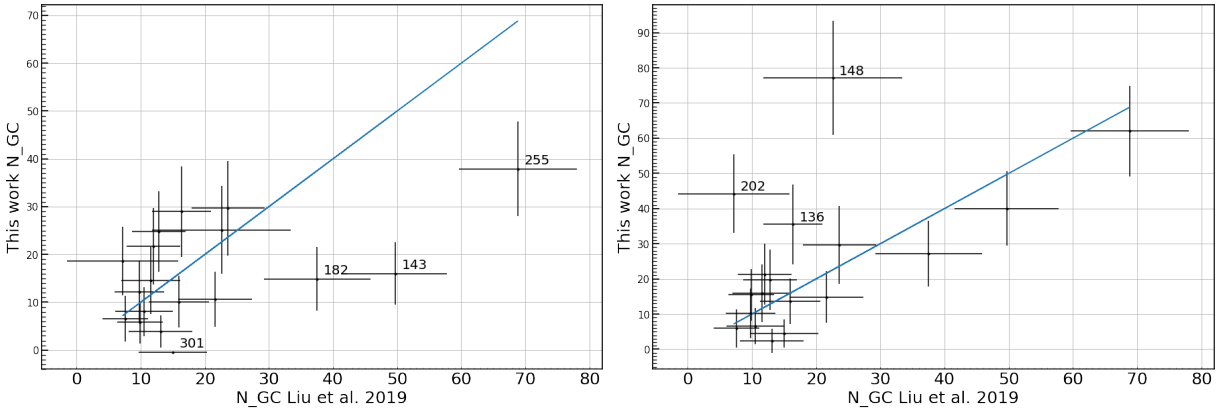

Figure 26: Number of GCs from Liu et al. [2019] versus the number of GCs from this work. The blue line corresponds to a one-to-one correlation. The galaxy FCC number is included for the outliers. Left panel: the area for the number of GCs used is $3 \times R_{eff}$. Right panel: the area for the number of GCs used is $5 \times R_{eff}$.

based on the mean density of contaminants, area of the annulus between two subsequent GCs and p_{GC}. Based on these values, Liu et al. [2019] fit Sérsic radial profiles which are extrapolated to infinity to determine the number of GCs per galaxy.

Due to different data sets and different methods, it is not expected to have a perfect correlation between this work and the work of Liu et al. [2019]. However, many of the galaxies have comparable values within the error bars. It is also good to note the dependence of the are, for several galaxies the difference between an area of $3 \times R_{eff}$ and $5 \times R_{eff}$ results in a big difference in the number of GCs. A couple of galaxies, are also noted as special cases in the work of Liu et al. [2019] and retrieve a specific treatment. In this work, we do not consider specific galaxy cases in determining the number of GCs.

3 Results

To obtain the number of GCs for the total sample of 540 dwarf galaxies available in the FDS, the galaxies have gone through the data reduction steps as explained in Section 2.2. In this section, the database of GCs is described for 540 dwarf galaxies. This includes an estimate of the number of GCs per galaxy, but the catalog also includes locations, g, r and i magnitudes and compactness measurements of the observed GCs.

After obtaining all the sources within the images of the galaxies, they are divided into bins based on their g magnitude. The sources are only considered as GCs when they are contained within the convex hull of the corresponding g magnitude range. After this selection, we are left with all the GCs found within the image of $15 \times R_{eff}$. To make a selection of GCs per galaxy, we only select data points that are found within a specific radius. Only sources within an ellipse with major axis $3 \times R_{eff}$ are considered. The resulting number of GCs for all the galaxies is visible in Fig. 27 versus the absolute r-band magnitude, where the right panel has uncertainties included.

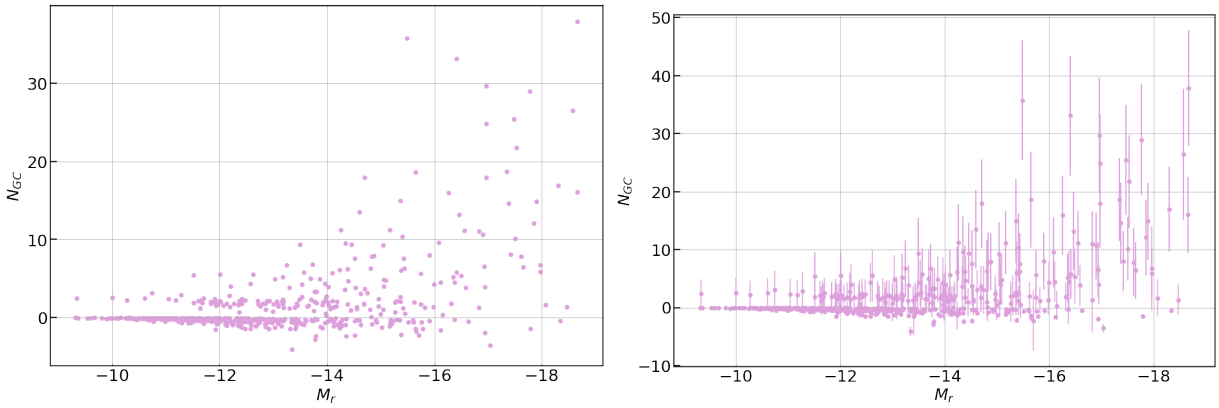

Figure 27: The number of GCs versus the absolute galactic r-band magnitude with and without uncertainties. The negative values arise from galaxies with initially none or almost no GCs. The background subtraction returns a negative LF which increases due to the multiplication of the correction factors.

From Fig. 27, it is possible to see an increase in the number of GCs for brighter galaxies, as expected. The total sample contains 540 galaxies of which 194 have a positive number of GCs. The number of galaxies with zero or a negative amount of galaxies is increasing for fainter galaxies as expected for low luminosity galaxies [Georgiev et al., 2010; Lim et al., 2018; Carlsten et al., 2021a]. Several aspects of the galaxies can be used to investigate their relation with the number of GCs. In the next section we will compare the complete sample to other works, investigating the number of globular cluster N_{GC}, specific frequency S_N, specific mass frequency T_N and dark matter halo mass estimates.

4 Analysis

For 540 dwarf galaxies in FDS sample, we have calculated the number of GCs of which 194 galaxies have GCs ($N_{GC} > 0$). The uncertainty in the number of GCs is calculated considering Poisson errors from the number of GCs and from the background subtraction. We have calculated averages to find a trend within the number of GCs and specific frequency, which makes it more accessible to draw conclusions and compare to other works.
In Section 4.1, we will discuss the radial range for the considerations of GCs; in Section 4.2 we compare our results for the number of GCs and the specific frequency to previous works; in Section 4.3 we divide the complete sample of 540 galaxies into several sub samples based on different parameters: spatial distribution, early- and late-type galaxies, nucleation and surface brightness; in the last Section 4.4 we present estimates of the dark matter halo masses of the Fornax dwarf galaxies.

4.1 Radial range to consider the GCs

An important choice is the radius wherein the GCs are counted and considered part of the galaxy. This value depends on the radial distribution of the GCs in low mass dwarf galaxies. Therefore the radius is often determined by deriving the half-number radius, the radius where half of the GCs are contained within. Several works [Lim et al., 2018; Amorisco et al., 2018; van Dokkum et al., 2017] have studied this GC half-number radius and the half-number radius of the GC distribution is often taken as $1.5 - 2.0 \times R_{eff}$ but there remains uncertainty in these radial profiles. Carlsten et al. [2021a]; Prole et al. [2019] also investigated the radial profile and find a small preference for $r_{GC} > R_{eff}$. They counted the GCs within $2 \times R_{eff}$ to investigate the radial distribution and assume a Plummer profile for this distribution and find a half-number radius of $1.2 \times R_{eff}$. They corrected for the GCs outside of their radius by integrating the Plummer profile to infinity. In this work, we take a larger radius of $3 \times R_{eff}$ while there is no correction applied for GCs outside this radius. For larger galaxies a value of $5 \times R_{eff}$ would be better suited due to the larger spread in the radial distribution from accretion of GCs. However, this would also increase the Poisson noise due to more background sources, so a lower signal to noise. A possible improvement for this work would be to use the local background subtraction for the region around NGC 1399 due to the high contamination and use the averaged background subtraction for the other regions of the Fornax Cluster. For the calculation of the local background it might be better to consider only data outside of a larger radius, such as $5 \times R_{eff}$, and not everything directly outside of the radius that is considered for the GC counts from the galaxy. The region between $3 \times R_{eff}$ and $5 \times R_{eff}$ is still likely to contain GCs from the galaxy itself and therefore not purely represent the background contamination around the galaxy.

4.2 Comparisons to previous works

Even though the counting of GCs is not a difficult task by itself, detecting them is. Therefore, the works investigating the number of GCs is limited especially in the low-mass dwarf regime. More massive galaxies have been studied in several surroundings such as Virgo by Peng et al. [2008] and Fornax by Villegas et al. [2010]; Jordán et al. [2015]; Liu et al. [2019]. Samples of nearby dwarf galaxies are also investigated by Lotz et al. [2004]; Georgiev et al. [2008, 2009] and recently a larger sample of dwarf galaxies in Virgo and the Local Volume by Carlsten et al. [2021a]. These referenced works are also the works used for comparisons. However, the number of galaxies considered in this paper is the largest until now.

4.2.1 Number of GCs

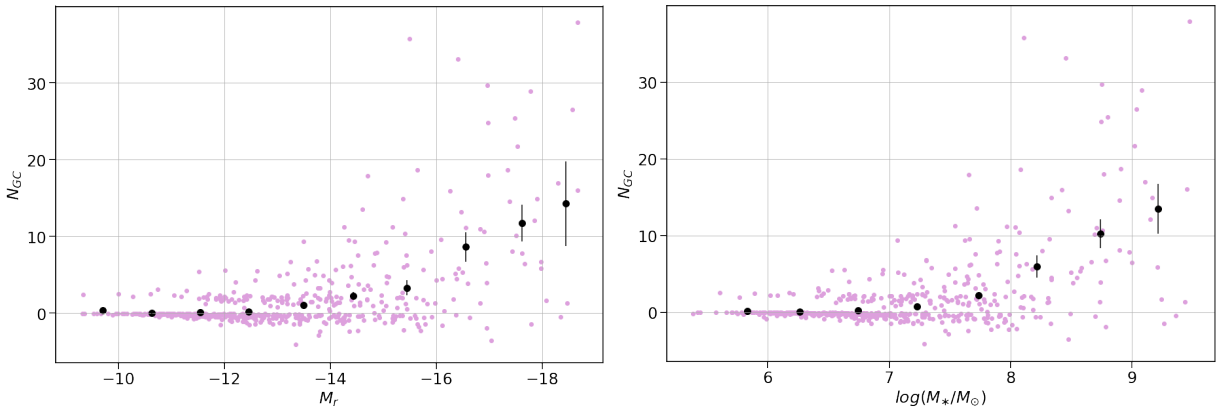

Figure 28: Left panel: The number of GCs versus the absolute galactic r-band magnitude. Right panel: The number of GCs versus the.stellar mass. The black circles represent the mean value and the error bars are the standard error of the mean.

To be able to compare the number of GCs to other works, we have calculated the mean number of GCs. This is done by binning the data from Fig. 27 in either M_r or $log(\frac{M_*}{M_\odot})$ in bin sizes of respectively 1 and 0.5. All the galaxies are considered for the calculation and the resulting means can be seen in Fig. 28, where the stellar mass is calculated through Eq. 10. The increase for brighter galaxies is clearly reflected in the mean values and the error in the number of GCs is also increasing for brighter galaxies due to a larger spread and smaller sample sizes. The error bars are displaying the standard error of the mean: $\sigma_{\bar{x}} = \frac{\sigma_x}{\sqrt{N}}$, where σ_x is the standard deviation. The higher the number of galaxies within a magnitude bin, the smaller the standard deviation in a relative sense.

In the left panel of Fig. 29, we see the number of GCs versus the stellar mass of the Fornax cluster, Virgo cluster [Peng et al., 2008; Carlsten et al., 2021a] and early-type satellites and small group hosts in the Local Volume (LV) [Carlsten et al., 2021a]. The sample of the LV consists of 177 dwarf galaxies, which is complete down to $M_V \sim -10$ [Carlsten et al., 2021b]. For the Virgo sample Carlsten et al. [2021a] used the Next Generation Virgo Survey (NGVS) catalog from Ferrarese et al. [2020] which is a sample of the center of the Virgo Cluster. The sample from Peng et al. [2008] is complete with early-type member until $B_T < 12$, containing very few dwarfs.

For low stellar masses almost no GCs are found and if GCs are present the highest numbers are found in the Virgo Cluster. Increasing in stellar mass means in general an increase in number of GCs and scatter. In the right panel of Fig. 29, the mean number of GCs is calculated for the different data sets in the same manner. The Virgo cluster has on average the highest number of GCs at a given stellar mass. The dwarf galaxies in the Local Volume and Fornax are more comparable considering the number of GCs. In the range of $log(M_*/M_\odot) = 8 - 8.5$ the Local Volume has a higher average than Fornax. However, the average of the Local Volume in this range is represented by a smaller sample than Fornax. Also, at higher stellar masses the number of GCs in this work are more likely to serve as a lower boundary due to the area considered for the GCs counts (see Section 2.8 and 4.1). The Virgo sample also shows a steeper increase with a slight dip at $log(M_*/M_\odot) = 8.5 - 9$ caused by the manner of binning. Due to the sample size of this work, our errors are smaller than the work of Carlsten et al. [2021a] especially in the lower mass bins. This is best visible in Fig. 30, which is a zoomed in version of Fig. 29.

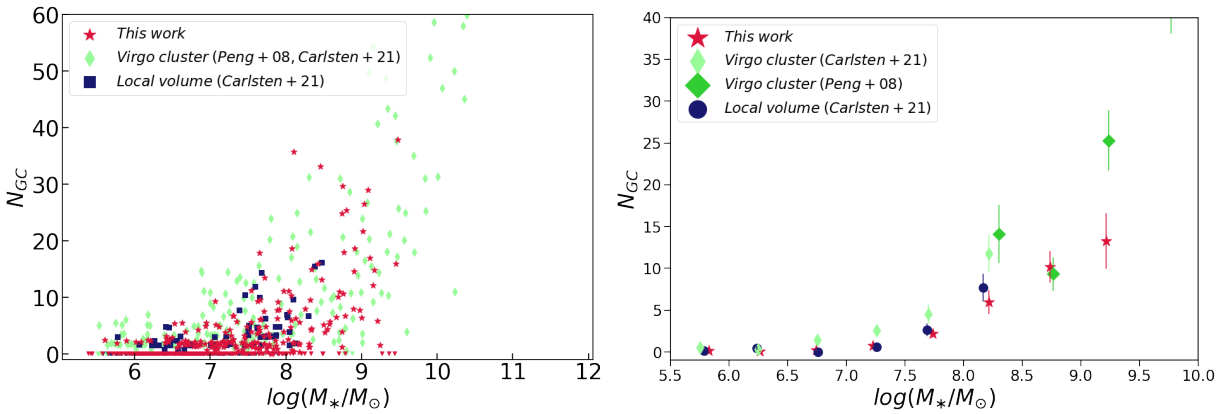

Figure 29: Left panel: The number of GCs versus stellar mass for this work, the Virgo cluster where the more massive galaxies are from Peng et al. [2008] and the low mass range of Virgo and the Local Volume is from Carlsten et al. [2021a]. Right panel: Corresponding averages calculated by binning the data in bin sizes of 0.5 and the error bars are the standard error of the mean.

However, one of the most prevailing parameters is the specific frequency calculated through Eq. 7 and is defined as the number of GCs per galactic luminosity, which expresses the efficiency of the GC formation with respect to other stars in the galaxy. In Fig. 31, the vertical axes is given by $S_{N,r}$ which is the specific frequency calculated based on the absolute r-band magnitude and normalized with a value of $M_r = -15\ mag$. The specific frequency depends on the number of GCs in a galaxy and galaxies with no GCs are presented as triangles at the bottom of Fig. 31. The trend for dwarf galaxies in S_N is increasing for decreasing galactic luminosity [Peng et al., 2008; Miller and Lotz, 2005; Durrell et al., 1996] which is in agreement with this work (see Fig. 31). The decrease in the specific frequency is valid until galaxies with luminosities of $M_V \approx -20\ mag$, brighter galaxies show an increase again in the specific frequency [Peng et al., 2008; Harris et al., 2013; Rhode et al., 2005].

In Fig. 32, the galaxies are too faint to show the flattening. It does compare the S_N of this work to Coma dwarfs [Lim et al., 2018] and UDGs [Lim et al., 2018] from the HST/ACS Coma Treasure Survey. The UDGs of the Coma cluster have the highest S_N. Due to the consistence in the manner of binning method, some conclusions might be more difficult to draw with smaller samples of other works. The higher S_N from the Coma UDGs is visible in most bins however in the brightest and faintest bin it is represented by one galaxy, which also explains the missing error bars. The S_N of the Fornax cluster is lower than the UDG samples but comparable to the Coma dwarfs. The Coma dwarf sample consists of a total of 54 dwarfs and therefore the statistics are better in this work leading to smaller uncertainties. Expectably, the S_N is the highest in Coma, since the galaxy density is the highest, followed by Virgo and lastly Fornax.

Another useful parameter is the specific mass frequency, T_N, which depends the number of GCs and the stellar mass of the galaxy calculated trough Eq. 11. In Fig. 33, data from the LV and the Virgo cluster [Carlsten et al., 2021a] are displayed as well. The dashed black lines show the specific mass frequencies for $N_{GC} = 1, 10, 20$ and 30. The dwarfs in Virgo have a higher T_N than in the LV and Fornax, even though the differences are not so high around $log(M_*/M_\odot) \sim 8$. The LV is in the same range as Fornax however with larger errors. In general for the low mass galaxies the average number of GCs is lower than 1.

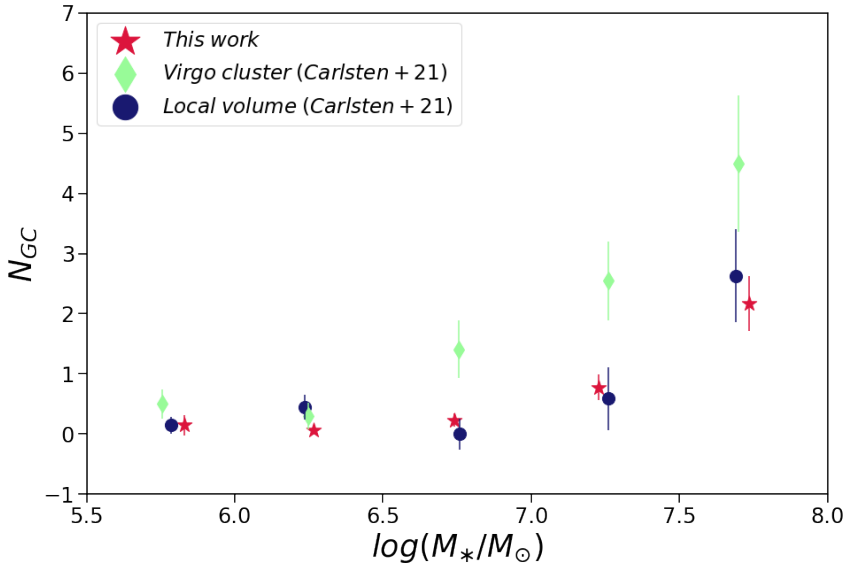

Figure 30: Averages for the number of GCs versus the stellar masses. This image is a zoomed in version of Figure 29.

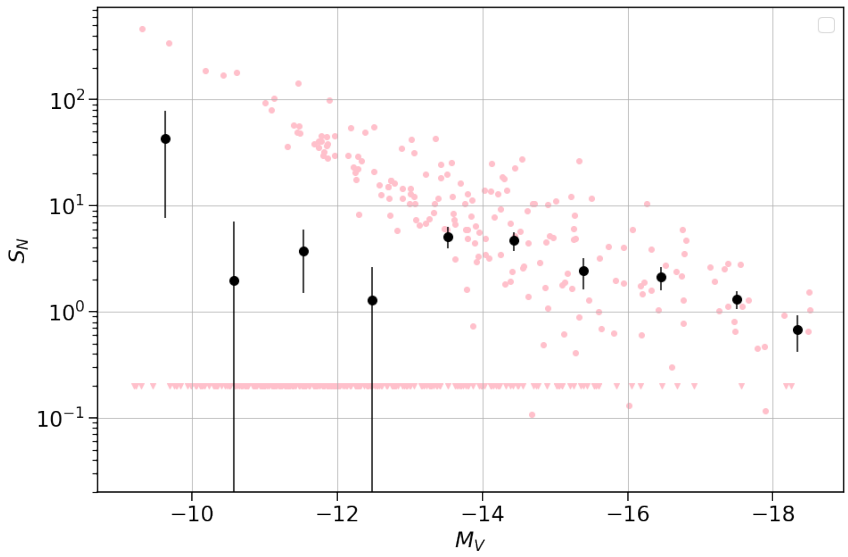

Figure 31: Specific frequency versus the V-band magnitude. Galaxies with zero or no GC are represented by the line on the bottom of the figure. Thee mean value for the specific frequency is calculated per bin with a size of 1 mag

4.3 Subsamples

To take a closer look at the dwarf galaxies in Fornax, we divide the sample by different parameters. This allows us to study possible environmental effects, but also the differences in the number of GCs between early- and late-type galaxies and the presence of nuclear star clusters. We will also divide the sample based on the surface brightness to see if this results in a significant difference in the specific frequency. All with the aim of understanding GC formation, and dark matter halos. To test for significance throughout this section, we have applied Kolmonogrov-Smirnov tests (KS-test).

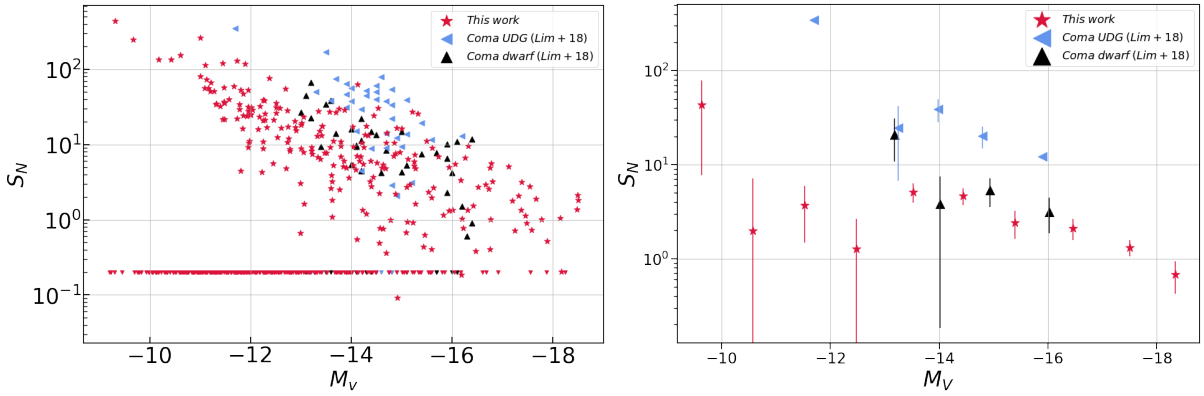

Figure 32: Left panel: The number of GCs versus the absolute V-band magnitude compared to samples of the Coma cluster [Lim et al., 2018]. Right panel: The mean number of GCs versus the V-band magnitude calculated in bins of 1 *mag*. The error bars are the standard error of the mean.

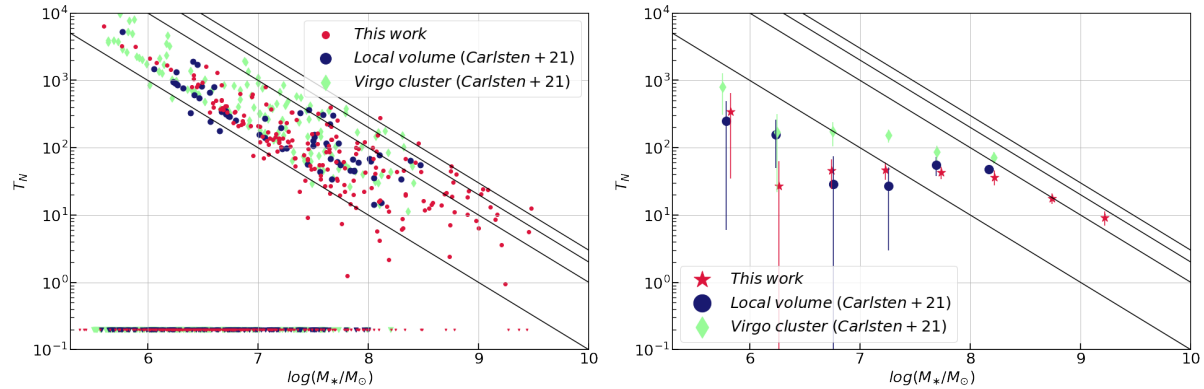

Figure 33: Left panel: Specific mass frequency versus the stellar mass compared to the Virgo cluster and the Local Volume [Carlsten et al., 2021a]. Right panel: The mean specific mass frequency versus the stellar mass calculated in bins of 0.5. Galaxies with zero or no GCs are represented by the triangles in the bottom of the figure.

4.3.1 Environment

	$N_{galaxies,all}$	$N_{galaxies\ with\ N_{GC}>0}$
Fornax core	80	47
Outskirts	407	136
Fornax A	53	11

Table 8: Number of GCs in every regions with and without including the galaxies with $N_{GC} = 0$. Fornax core region is consisting of all the galaxies within < 0.7 *deg* of the central galaxy NGC 1399 (see blue inner circle in Fig. 7). Fornax A region contains all the galaxies within 1 *deg* of Fornax A (see green circle in Fig. 7). The outskirt region contain all the residual galaxies.

The environment of a galaxy plays an important role in its creation and evolution and therefore also on the number of globular clusters. To investigate the effects of the environment on the number of GCs per galaxy, we divide the galaxies in three groups based on their location:

Fornax core, Fornax A and outskirt region. For more details on the differences between the Fornax core and Fornax A region, see Su et al. [2021]. The Fornax core group is consisting of all the galaxies within < 0.7 *deg* of the central galaxy NGC 1399 displayed by the inner blue circle in Fig. 7, the Fornax A group is consisting of galaxies within 1 *deg* of Fornax A visible as the green circle in Fig. 7 and the outskirts region is consisting of all the galaxies that are not part of one of the previous groups. The number of galaxies in every group is visible in Fig. 8, where the number of galaxies are included for the complete sample and for the positive N_{GC} sample. In the left panel of Fig. 34, the mean number of GCs is visible for every group versus the stellar mass. For all the stellar masses the Fornax A regions seems to have the lowest amount of GCs and the Fornax core region the largest number of GCs. In the right panel, the specific frequency versus the absolute r-band also including the mean values for all the three regions. The Fornax A region has a significantly lower S_N than the Fornax core group. It is important to note that the difference in binning in the two figures lead to a different amount of data points and not all bins contain galaxies.

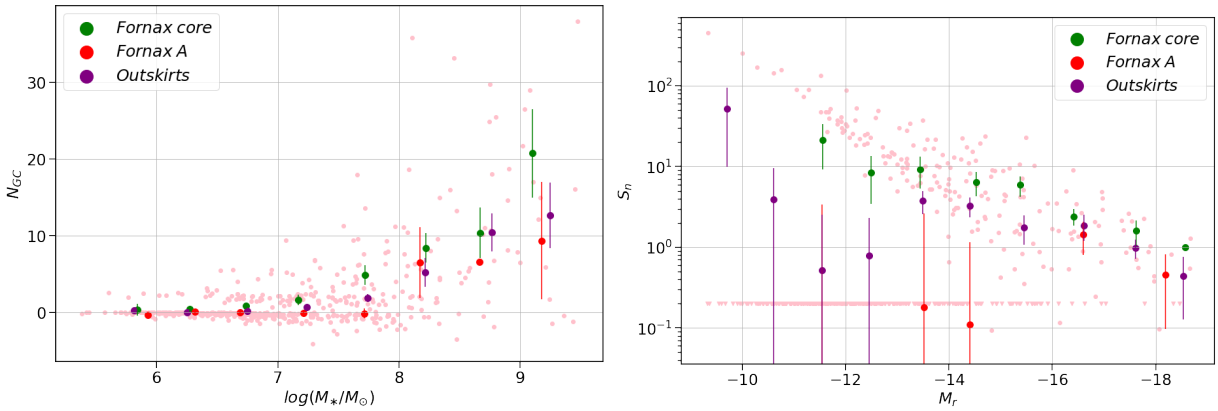

Figure 34: Left panel: Number of GCs versus the stellar mass including average values for three different regions. Right panel: Specific frequency versus the absolute r-band magnitude. Galaxies with zero or no GCs are represented by the triangles in the bottom of the figure. The mean values are calculated per bin with a size of 1.

While the Fornax core group lies in the densest regions of the cluster, the amount of GCs can be influenced by intragalactic GCs and GCs from NGC 1399. Therefore, we have also investigated the effects of local background subtraction on the mean of the Fornax core group. In Fig. 35, the mean number of GCs is visible for the the three different regions with a local background subtraction for the Fornax core group. The Fornax core group is definitely lower due to the local backgrounds subtraction, yet the Fornax A group does remain lower. The local background subtraction show its strongest decrease in the last two stellar mass bins. This is also the range where observed the strongest effect in Section 2.6.2 and due to this decrease and the overlapping error bars, it becomes difficult to draw any strong conclusions. It would be best to investigate this further by taking a more sophisticated approach for the background subtraction in the main region of Fornax or possibly investigate more specific cases, to find a clear trend between the clustercentric distance and the specific frequency.

Liu et al. [2019] investigated the GC specific frequency for 43 early-type galaxies for Fornax combined with the ETGs from Peng et al. [2008]. To investigate the environmental effect they uses two parameters following the work of Guérou et al. [2015], who implemented a region of the

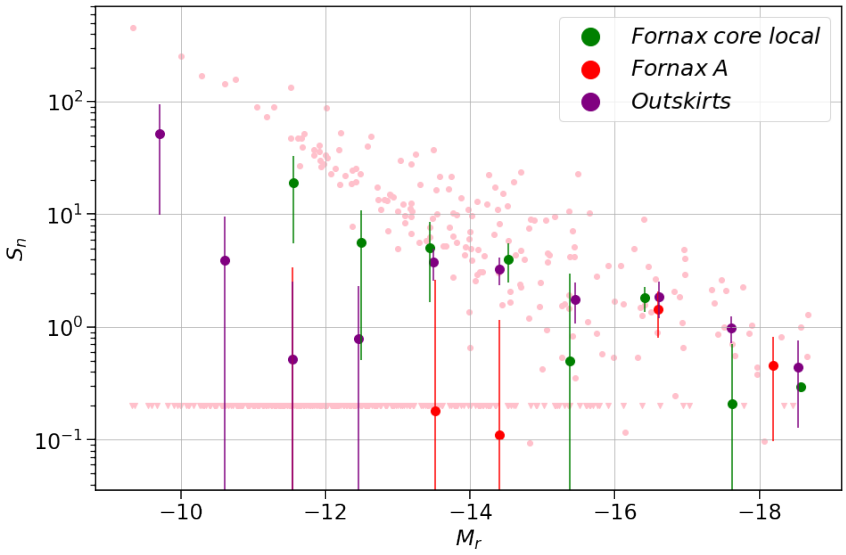

Figure 35: Specific frequency versus the absolute r-band magnitude for three different regions. The Fornax core region is calculated with local background subtraction. The Fornax A region and the outskirts are calculated with averaged background subtracted.

15 closest neighbors. They find that low-mass galaxies located within the densest environments with strong tidal forces actually strip the galaxies of their GCs, while the galaxies that are not in these strong tidal fields but in denser regions have a higher GC formation efficiency. They find low $S_{N,z}$ for galaxies within $10 \times R_{eff}$ of the massive host galaxies or most luminous galaxies which is likely caused by tidal stripping of the GCs. $10 \times R_{eff}$ of NGC1399 and NGC1316 are within ~ 0.1 *deg* and respectively three and zero galaxies are found within this range. Therefore, the possible stripping of GCs will not effect the averages strongly within the regions considered.

4.3.2 Early- and late-type

	$N_{galaxies,all}$	$N_{galaxies\ with\ N_{GC}>0}$
Early-type	453	175
Late-type	85	17

Table 9: Total number of galaxies with and without GCs for early- and late-type galaxies.

In the dwarf galaxy catalog of Venhola et al. [2018a], the galaxies are also labeled as early- or late-type galaxies with possible spiral structure. This distinction between early- and late-type is through first order morphological classifications based on visual inspection and parametric classification. For more details on the morphological classification see Venhola et al. [2018a]. The galaxies are divided into the groups early- or late-type galaxies.

In Table 9, the division between early- and late-type galaxies is given considering all the 540 galaxies in the sample. The left panel of Fig. 36, shows the number of GCs versus the absolute r-band. The right, panel shows the specific frequency, where the galaxies with no GCs are causing the lower means. The mean number of GCs is higher for early-type galaxies than for late-type galaxies except for the last two bins where the error bars are larger and overlapping.

In the right panel of Fig. 36, the mean $S_{N,r}$ is derived based on the distinction between the early- and late-type galaxies. The largest part of the sample is early-type as can be seen from

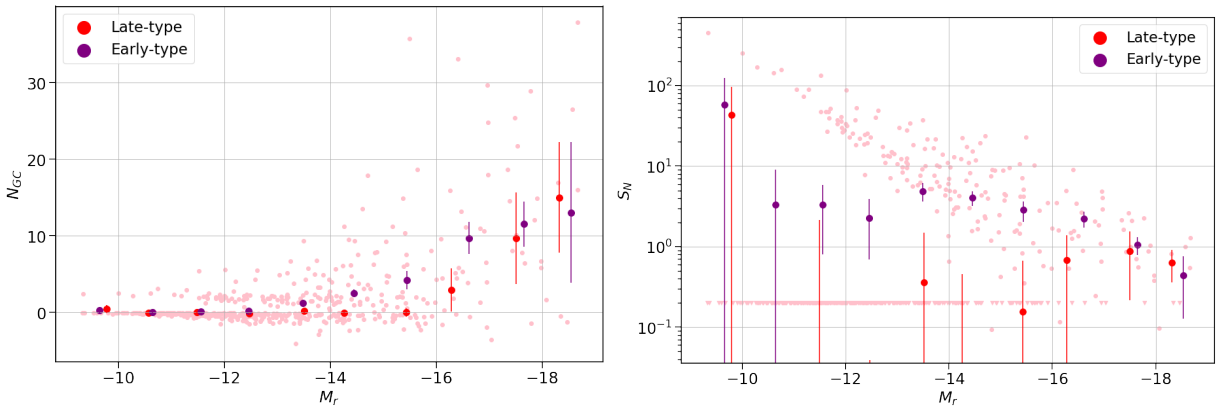

Figure 36: Left panel: Number of GCs versus the absolute r-band magnitude including average values for early- and late-type galaxies. Right panel: Specific frequency versus the absolute r-band magnitude. The mean values are calculated per bin with a size of 1 mag. Galaxies with zero or no GCs are represented by the triangles in the bottom of the figure.

Table 9, and the early-type galaxies also contain a higher percentage of galaxies with GCs than the late-type galaxies. The early-type galaxies show an earlier increase in the number of GCs than the late-type galaxies but have a similar mean for the brightest galaxies.
In the work of Georgiev et al. [2010], they compare the S_N values of early- and late-type galaxies from several works. They observe a similar trend for the early-type galaxies, so increasing S_N for decreasing luminosities. In Fig. 37 the specific frequencies for several different type of galaxies is shown, most importantly for this work are the mean values for early- and late-type galaxies. The mean values are calculated by binning the data in magnitude bins and the error bars are showing one standard deviation. Georgiev et al. [2010] finds that late-type galaxies have a lower mean at specific galaxy luminosities than early-type galaxies, just as in this work. There is also quite some scatter in the fainter regions with large error bars, which are smaller in this work due to the large sample size. We can conclude that the mean S_N is significantly higher for early-type galaxies than for late-type galaxies.

4.3.3 Nucleation

We can also divide the dwarf galaxy sample based on the presence of nuclear star clusters. Venhola et al. [2018a]selected the galaxies with nuclear star clusters and found that towards the center of the main cluster, the fraction of early-type and nucleated galaxies increases. This is however not the case for the Fornax A region where the fractions are lower compared to the main cluster and not a clear correlation is found. The division of the nucleated galaxies can be seen in Fig. 38.

In Fig. 39, we show S_N for the nucleated and non-nucleated galaxies. The S_N for nucleated galaxies is significantly higher than the non-nucleated galaxies.
In the work of Miller and Lotz [2007], they have investigated several Virgo and Fornax dwarfs especially looking at the differences between nucleated and non-nucleated dwarfs. They find that the nucleated sample is more centrally concentrated and has a higher S_N than the non-nucleated and less concentrated galaxies which is in agreement with this work. The nucleated sample in Fornax is also more centrally concentrated [Venhola et al., 2019]. Carlsten et al. [2021a] also investigated the effects of nucleated galaxies and confirms the results from Sánchez-Janssen et al. [2019] stating that the nucleation fraction of dwarfs a dependence on the environment. Several

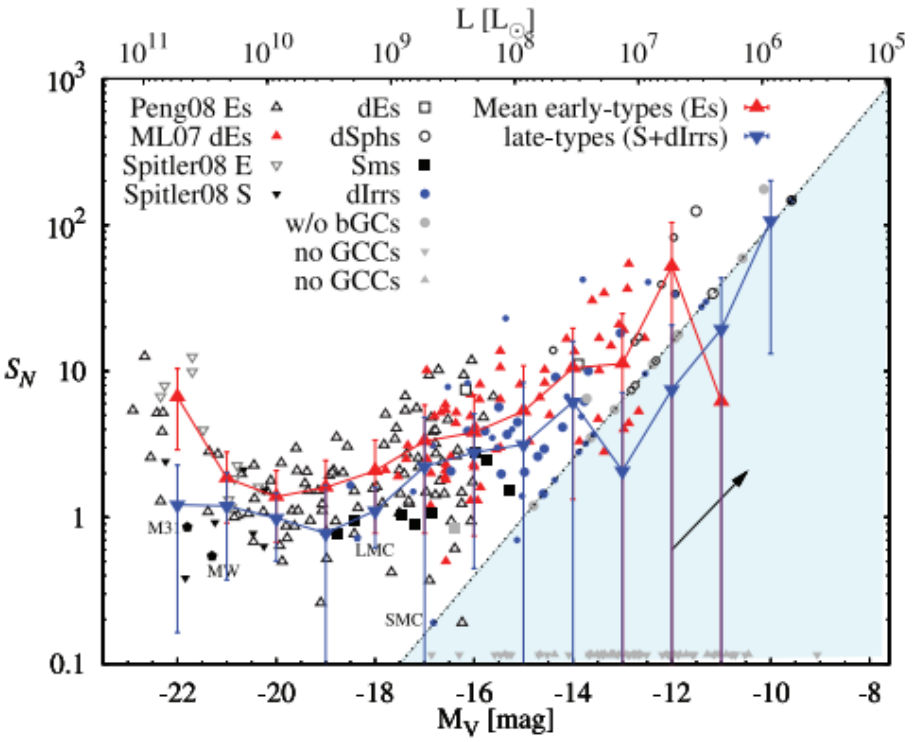

Figure 37: The specific frequency versus the absolute V-band magnitude from different works and different type of galaxies. The errors bars are displaying the standard deviation for every magnitude bin. The dashed line represents the S_N when a galaxy has one GC. For a complete overview from the literature values included, see the original figure in Georgiev et al. [2010].

works with different data samples focused on early-type galaxies have found a significant difference between the nucleated and non-nucleated galaxies with an environmental trend [Ferguson and Sandage, 1989; Miller and Lotz, 2007; Lim et al., 2018; Zanatta et al., 2021].

4.3.4 Surface brightness

The surface brightness is the amount of light per area in the sky and is calculated for all the dwarf galaxies through Eq. 2.7. In Fig. 40, the surface brightness is visible at different stellar masses. This data is binned in the horizontal axis with steps of 0.5 and in every bin the data is divided into two equal sized groups where the surface brightness is ordered. This results in two groups for every bin of with the lowest surface brightness galaxies (faint) and the highest surface brightness (bright). In Fig. 41 the number of GCs is displayed versus the stellar mass including the averages for the two surface brightness ranges. Galaxies with the same stellar mass and a fainter surface brightness have on average a higher number of GCs. In the right panel, we can see the $S_{N,r}$ versus M_r with the division of high and low surface brightness based on the stellar mass. In general, the $S_{N,r}$ is higher for low surface brightness galaxies although the trend is and difference is strongest in the brightest regions ($M_r < -14$).

There are not so many works that have investigated the relation between the number of GCs and the surface brightness of dwarf galaxies. Yet it can give interesting insights on the ongoing debate on the difference between Ultra-diffuse galaxies (UDGs) and dwarf galaxies. The number of GCs has also been an important proxy for the dark matter halo mass for UDGs in several clusters [Amorisco et al., 2018; Lim et al., 2018; Prole et al., 2018; Beasley and Trujillo, 2016a]

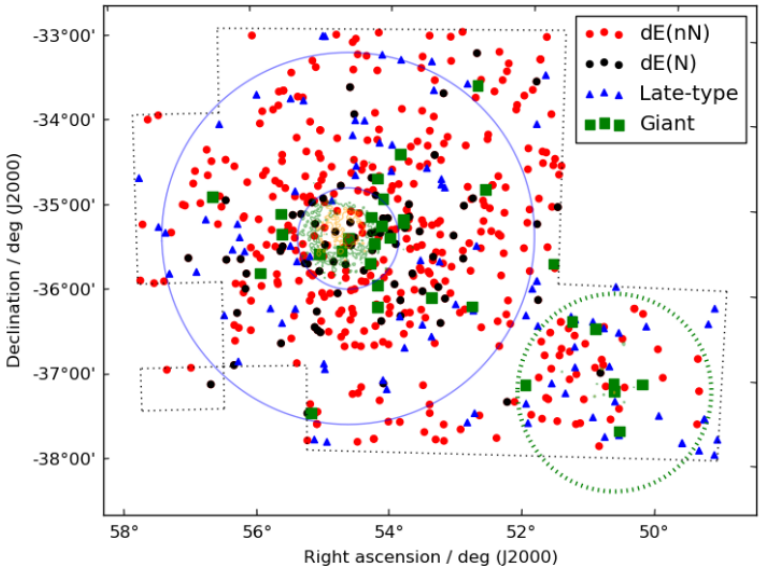

Figure 38: Locations of different type of galaxies: non-nucleated dwarf ellipticals (dE(nN)), nucleated dwarf ellipticals (dE(N)), late-type dwarf galaxies (Late-type) and giants. The inner blue circle represents the core [Ferguson, 1989] and the outer the virial radius [Drinkwater et al., 2001] of the cluster its main galaxy NGC 1399. The green circle has a one degree radius centered at the Fornax A subgroup NGC 1316 [Drinkwater et al., 2001]. This figure comes from Venhola et al. [2018b].

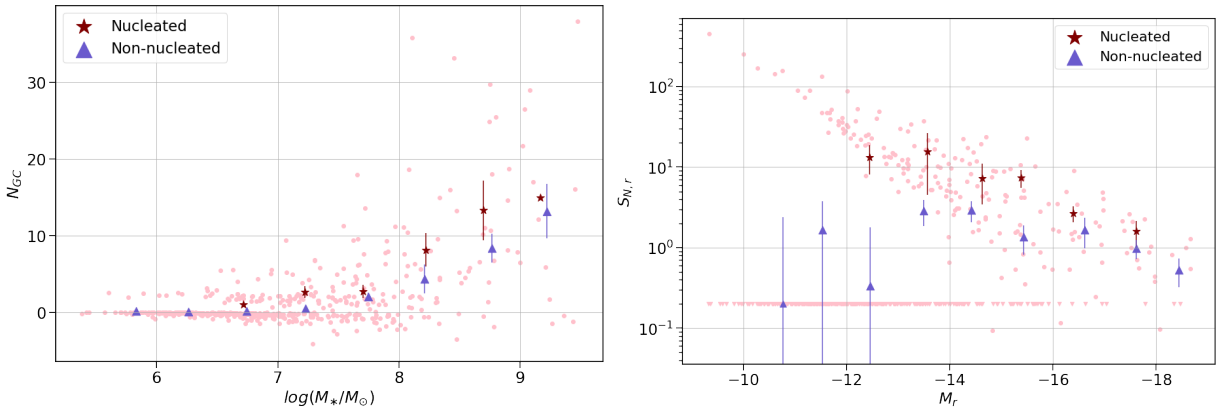

Figure 39: Left panel: Number of GCs versus the stellar mass including average values for nucleated and non-nucleated galaxies. Right panel: Specific frequency versus the absolute r-band magnitude including averages. Galaxies with zero or no GCs are represented by the triangles in the bottom of the figure.

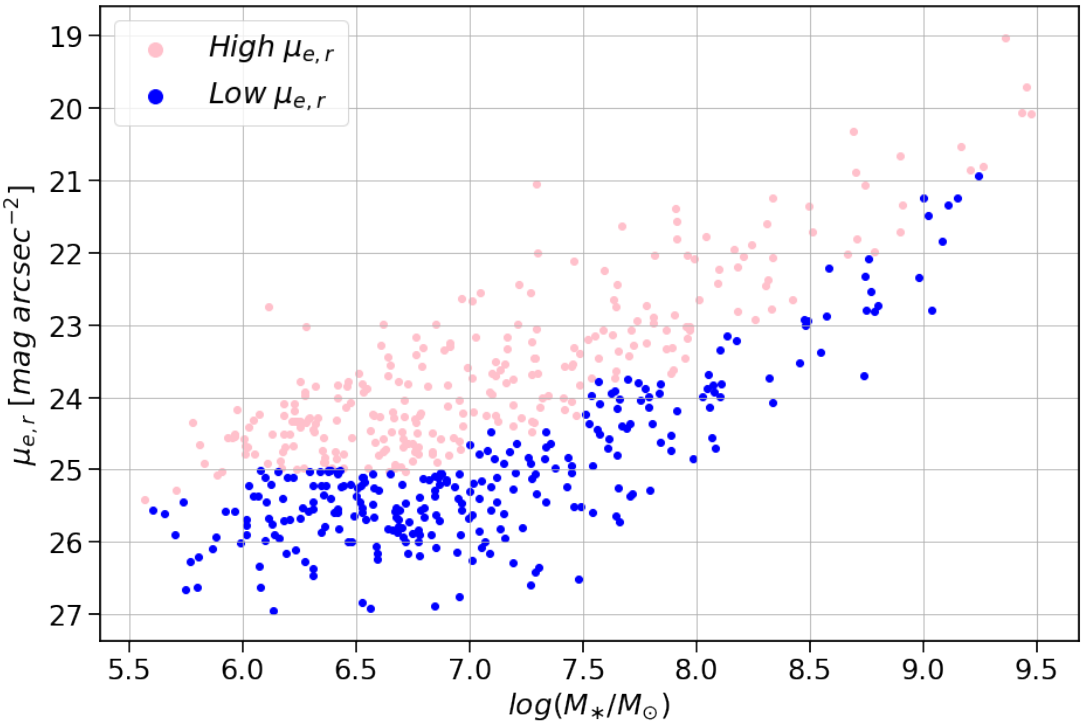

Figure 40: The surface brightness versus the stellar mass, where the surface brightness is calculated through Eq. 2.7 and the stellar mass through Eq. 9. At every stellar mass bin of 0.5, the data is divided in equal sizes of low and high surface brightness.

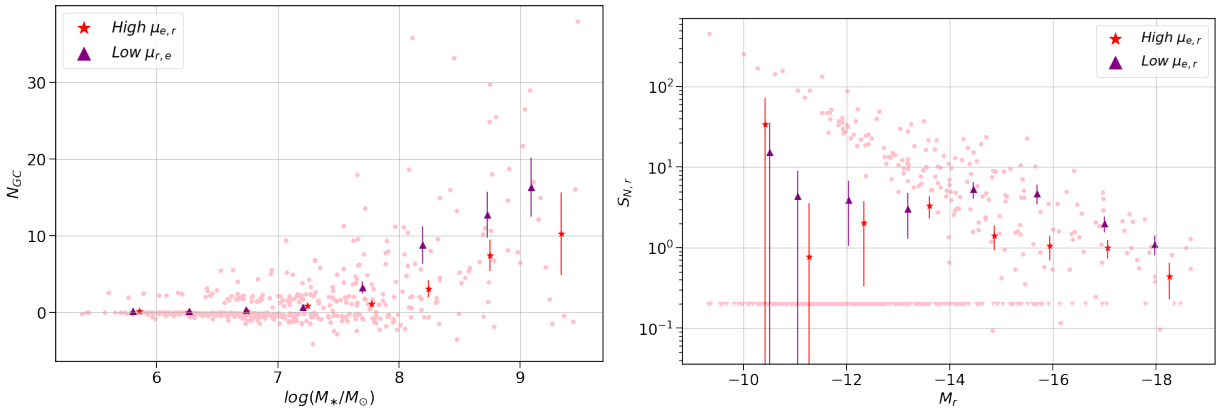

Figure 41: Left panel: Number of GCs versus the stellar mass including average values for low and high surface brightness galaxies. Right panel: Specific frequency versus the absolute r-band magnitude including averages. The high and low surface brightness groups are divided within stellar mass bins from Fig. 40. Galaxies with zero or no GCs are represented by the triangles in the bottom of the figure.

and these values are consistent within the range of dwarf galaxies. Lim et al. [2018] studied UDGs in the Coma Cluster and finds that the S_N is higher for UDGs than for dwarf galaxies. They also investigated the relation between the specific frequency and surface brightness of dwarfs and UDGs. They observed that galaxies with $\mu_e \sim 25\ mag/arcsec^2$ have higher S_N values than higher surface brightness galaxies. However there is also a lot of scatter found in

this trend resulting in a insignificant correlation.

The work of Miller and Lotz [2007] investigates mostly the differences between nucleated and non-nucleated galaxies but also finds a trend in the surface brightness. The specific frequency increases with decreasing central surface brightness for nucleated galaxies.

4.4 Dark Matter Halo Mass

Between the number of GCs and the dark matter halo mass is a well-known relation, see Eq. 13. This relation is built upon the ratio between the GCs mass and the halo mass of the host galaxies, where the GCs mass is based in the number of GCs and the mass-to-light ratio for GCs. Several works [Hudson et al., 2014; Harris et al., 2017; Beasley and Trujillo, 2016b; Spitler and Forbes, 2009; Peng and Lim, 2016] studied this method and found that the ratio is constant below a stellar mass of $M_* = 10^{11} M_\odot$. Liu et al. [2019] also investigated this relation using this method, where the dark matter halo mass is inferred from the global stellar mass-halo relations from Behroozi et al. [2010]. They also found a decrease in the ratio for stellar masses higher than $3 \times 10^{10} M_\odot$, possibly by the higher halo masses from Behroozi et al. [2010]. On the numerical side, these relations can be investigated by semi-analytic models based on dark matter trees [El-Badry et al., 2019]. Kruijssen [2015] suggested as an explanation for the linear relation between the GC mass and the dark matter halo the environmental effects on the number of GCs and the merging of galaxies. Therefore a possible explanation for the constant ratio can come from the central limit theorem and the merging of galaxies [El-Badry et al., 2019; Choksi and Gnedin, 2019; Bastian et al., 2020].

Even though the uncertainties are large, it gives a rough estimate of the dark matter halo mass. In Fig. 42, the left panel shows the halo mass versus the absolute r-band magnitude and the right panel versus the stellar mass. Only for galaxies with $N_{GC} > 0$ the dark matter halo mass can be calculated which does not mean that the galaxies with no GCs do not have a dark matter halo mass. Galaxies with the same stellar mass or magnitude show a large spread in the dark matter halo mass.

To infer strict conclusions about the halo mass from the previously investigates sub-samples (environment, early- and late-type galaxies, nucleation and surface brightness) is not possible.

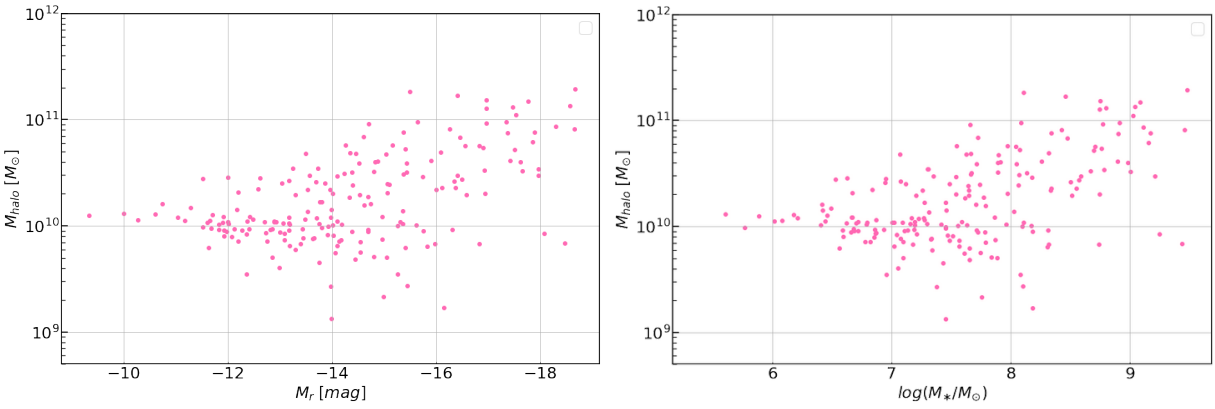

Figure 42: Left panel: Halo mass versus the absolute r-band magnitude. Right panel: Halo mass versus stellar mass. The halo mass is calculated through Eq. 13.

5 Discussion

The exact nature behind the formation of GCs remains obscure. The search started however with the formation of massive ellipticals due to the high number of GCs while at low masses most galaxies do not possess any GCs. Both observations and simulations are creating the framework where GCs form early and quick and the galaxies SF is quenched at later times. The galaxy can still accrete stars later on through dissipationless mergers. For the low mass regime, the dwarf galaxies, it is possible that some GCs are destroyed. The GCs are possibly already stripped by tidal interactions within their surroundings, destructed over cosmic time or disrupted early-on [Fall and Rees, 1977; Vesperini, 1998; Fall and Zhang, 2001; Fall et al., 2005; Bastian, N. et al., 2005]. However, it is also a possibility that the GCs were never formed in these galaxies. Georgiev et al. [2010] observed isolated galaxies without GCs which implies that the lack of GCs in dwarf galaxies can not be purely explained by tidal stripping.

Another topic is the GC formation efficiency. The relation between the number of GCs and the galactic mass encourages an explanation from dark matter simulations. These simulations can not yet explain the discrepancy between the GC and field star formation. In other words, how can the difference in S_N values for different galaxies and environments be explained? We will discuss some of these problems and possible explanations below for the several findings represented in Section 4.

In Section 5.1, we will discuss the possible explanations for the difference in the number of GCs for different clusters and within the Fornax Cluster; in Section 5.2, we will discuss the trends for the higher number of GCs in early-type galaxies; in Section 5.3, we will elaborate on possible formation paths for nuclear star cluster and their relation to GCs; in the last section 5.4, we discuss the effects of the surface brightness on the number of GCs.

5.1 Environment

In this work, we do not find a significant difference in the S_N of the Fornax core region and the outskirts regions. Even though the core region is denser and therefore it might be expected to have a more effective GCs efficiency [Peng et al., 2008; Lim et al., 2018; Liu et al., 2019]. This can have several explanations, such as the manner of sampling and investigating or specific reasons valid for the Fornax cluster. We have divided the complete sample bases on their location from NGC 1399 and Fornax A, NGC 1316. Another method could have been using the environmental parameter from Guérou et al. [2015]; Liu et al. [2019]. This environmental parameter takes other dense regions into account because it considers the 15 closest surrounding galaxies and the corresponding area. The difference between the Fornax core region and the outskirts is not significant but the average trend is higher as can be seen from Fig. 34. When only the early-type galaxies are considered in these regions, we do observe an even larger difference between the averages of the Fornax core region and the outskirts.

The Virgo and Fornax cluster are of course also different environments which can also be seen from the average difference in the number of GCs for a fixed stellar mass (see Fig. 29). Virgo has an estimated mass around $5-6\times10^{14}M_{\odot}$ [Ferrarese et al., 2012; Kourkchi and Tully, 2017; Kashibadze, Olga G. et al., 2020] while the Fornax cluster has a virial mass of $7\times10^{13}M_{\odot}$ [Drinkwater et al., 2001]. Fornax is likely dynamically more evolved and has a lower galaxy density than the Virgo cluster. The lower galaxy density is also an explanation for the lower S_N in Fornax compared to the Coma cluster as seen in Fig. 32. A possible explanation for lower average of number of GCs for the Fornax A group could come from the relatively large number of late-type galaxies and non-nucleated galaxies and the low galaxy density in Fornax A. From the

total Fornax A group $\sim 35\%$ is late-type, compared to $\sim 19\%$ and $\sim 15\%$ respectively for Fornax core region and the outskirts. To investigate this effect, we have only considered the early-type galaxies in the three different samples and find that the difference in S_N is not significant but it remains lower than the other two regions. Considering the nucleation, Fornax A contains a total of 53 galaxies and only one of these galaxies contains a nuclear star cluster. In Section 4.3.2 and 4.3.3, we have seen the significant difference between the early- and late-type galaxies and nucleated galaxies and non-nucleated galaxies for the S_N. However, the question remains what caused or how large the effect was of for example the environment around Fornax A or if the galaxy is nucleated or not. Likely the environment will play an important role if not directly on the number of GCs than on the fact that a galaxy is nucleated or not or the distribution of early- and late-type galaxies.

In the literature several solutions have been proposed for the higher S_N in denser environments. One possibility for the higher S_N for dwarf galaxies in denser environments could be the earlier collapse of the subhalos, due to the higher merger rate in dense environments. Therefore the GCs form during higher SFR densities compared to the subhalos further out [Kruijssen, 2015]. This idea was observationally found and discussed by Peng et al. [2008]. The higher number of GCs is a result of a higher star cluster formation efficiency due to high pressure and densities in the interstellar medium [Goddard et al., 2010; Kruijssen, 2012]. Models have confirmed the higher GCs abundance in galaxies that formed earlier on [Mistani et al., 2016; Pfeffer et al., 2018; Carleton et al., 2021].

Another possibility for the increased S_N is that the GCs in denser galaxy regions are less affected by destruction processes than GCs in outer region galaxies. Proposed models can be found in Elmegreen [2010] and Kruijssen [2015]. The location of the GCs can be explained by these theories through early mergers, which will cause the GCs to also be in the outskirts of the galaxy.

5.2 Early- late-type galaxies

We found that the S_N is significantly higher for early-type galaxies than late-type galaxies. However, it can also be seen that the differences are not so large for bright galaxies. For both the number of GCs as S_N the brightest two magnitude bins are overlapping. Late-type galaxies are also further from the center of the cluster, residing in less dense regions which could also lead to a lower S_N. Georgiev et al. [2010] found that the specific luminosity S_L for early-type galaxies is twice the S_L of late-type galaxies. At a specific GC luminosity, late-type galaxies usually have a lower stellar mass than early-type galaxies. Late-type galaxies will likely form the GC in the disc because the accretion through mergers is unlikely due to the disc-like properties. The works of Bekki et al. [2006]; Rhode et al. [2005] explain the higher S_N for massive elliptical galaxies by hierarchical merging. One possible explanation for the formation of elliptical dwarf galaxies is that they formed from late-type dwarf galaxies, like irregulars (dIrrs), through tidal processes [Moore et al., 1998; Smith et al., 2015]. Yet dwarf ellipticals seem to have a higher number of GCs than late-type galaxies contradicting this formation suggestion. It would be possible when new GCs are formed during the transformation from dIrrs to elliptical resulting in younger GCs, which are generally not found [Sánchez-Janssen and Aguerri, 2012].

5.3 Nuclear star clusters

Several works have investigated the difference in S_N of nucleated and non-nucleated galaxies and find a higher S_N for nucleated galaxies which is also found in this work (see Fig. 39) [Miller and

Lotz, 2007; Lim et al., 2018; Carlsten et al., 2021a; Zanatta et al., 2021]. There might be a bias involved due to the radial distribution of the nucleated galaxies. The nucleated galaxies are more towards the center of the cluster (see Fig. 38) where on average also a higher number of GCs is found. Around a third of the nucleated galaxies is found within the Fornax core region. If we only consider the galaxies within the Fornax core region, we also find a higher S_N for the nucleated galaxies but this can only be concluded for the brighter ($M_V < -12.5\ mag$) galaxy range. At fainter magnitudes nucleated galaxies are not present. Carlsten et al. [2021a]; Sánchez-Janssen et al. [2019] also found a secondary dependence on environment for the nucleation fraction of early-type dwarf galaxies. Ordenes-Briceño et al. [2018] studied the Fornax dwarf population and compared their nucleation fraction in the range of $R_{vir}/4 < r < R_{vir}/2$ to the results of Eigenthaler et al. [2018] who studied the range $r < R_{vir}/4$, and found similar nucleation fraction. Both of these works studied the central dwarf region with the Next Generation Fornax Survey (NGFS).

The higher number of GCs corresponding with nucleated galaxies can also be linked to the formation of the galaxies. It is possible that the nuclear star clusters were formed in early SF period or by inspiralling GCs. That NSCs are found with a more metal poor population than stars surrounding them, suggest that the NSCs are either formed before the stars or grow later on but from less enriched gas (inspiralling GCs). However, it remains quite difficult for now to put constraints on the metal-poor populations observationally [Seth et al., 2010; Kacharov et al., 2018].

The other possible formation path, infalling GCs, was suggested for the first time by Tremaine et al. [1975]. The dynamical friction created while orbiting would drag the GCs towards the nucleus. For a more elaborate discussion on the formation and evolution of NSC see the review on NSCs from Neumayer et al. [2020]. To improve the understanding of the relation between the number of GCs and the NSC, spectral info obtained from IFU spectra will be critical [Fahrion et al., 2019; Johnston et al., 2020].

5.4 Surface brightness

We have found a significance difference in the S_N between low and high surface brightness galaxies. It is important to note that the division of low and high surface brightness is not based on one cut, but by dividing the sample in a stellar mass bin in two equal samples. This division can be seen in Fig. 40 and especially at high stellar mass most dwarf galaxies in the sample have in general a high surface brightness. We can draw the conclusion that at a specific stellar mass, a low surface brightness galaxy will have a higher S_N and number of GCs than high surface brightness galaxies.

The work of Lim et al. [2018] found a higher number of GCs trend for UDGs with $\mu_e \sim 25\ mag/arcsec^2$, which is the surface brightness cut until $log(M_*/M_\odot) \sim 7 - 7.5$. Around this stellar mass the trend starts while at lower stellar masses the average number of GCs is basically zero in all galaxies. Miller and Lotz [2007] showed an increasing S_N for lower surface brightness nucleated galaxies. In our two equally divided samples, the number of nucleated galaxies in the low surface brightness group is in most bins twice the number of nucleated galaxies in the high surface brightness group. This introduces a bias because of the higher S_N of nucleated galaxies at higher stellar masses. Therefore, we have checked if the trend remains when we consider nucleated and non-nucleated galaxies separately. The increase in S_N remains for both low surface brightness nucleated as non-nucleated galaxies with an increase in scatter and error bars due to the smaller samples.

6 Conclusions

In this work we have calculated the number of GCs in a sample of 540 dwarf galaxies from the Fornax Cluster. Data is obtained from the Fornax Deep Survey Dwarf galaxy Catalog in the gri bands. To improve the detection of the GCs, we model the light of the galaxy and subtract the elliptical model. Photometry of all observed sources is obtained through SExctractor with an aperture size of 8 pixels and to account for the missing light from larger radii, we apply aperture correction. A total of 19 dwarf galaxies from our sample is also available from HST data, more specifically the work of Jordán et al. [2015] who determined a probability (p_{GC}) for a source being a GC. We use the HST data to calibrate the GC sample, by matching our sources based on their location to the GCs ($p_{GC} > 0.75$) from Jordán et al. [2015]. This results in a GCs catalog for 19 galaxies with FDS photometry. To determine GCs in the resulting dwarf galaxies, we have considered three parameters for the selection: $g-r$, $r-i$ and Δm the compactness. We have divided the GC sample from the 19 galaxies in g magnitude bins and constructed convex hull in the 3d parameter space. New sources that are within these convex hulls are considered as GCs. To take into account the contamination of intra-GCs or non-GCs sources, we subtract a background which is an average number of sources found after the GC selection from 75 fields. After the background subtraction, we correct for incompleteness from GCs that are not matched to HST and from missing GCs due to the selection method. Only GCs in an ellipse of $3 \times R_{eff}$ are considered as GCs from the galaxy. The radius is strongly influenced by the larger galaxies which can contain GCs further out. For future works, it would be interesting to investigate the radial distribution of the GCs and possible adapt the $3 \times R_{eff}$ radius. By counting the number of GCs per magnitude bin until the GCLF peak and multiplying this number to account for the faint end of the LF, we obtain the total number of GCs in the galaxy. This leaves us with a sample of 540 dwarf galaxies including their number of GCs, of which only 194 galaxies contain GCs. The total sample of GCs is divided into several groups to investigate the influences on the number of GCs and the specific frequency, S_N, based on: location, early- late-type galaxies, nucleated and non-nucleated galaxies and surface brightness. Below we present the main conclusions from this work:

- We present the largest sample of dwarf galaxies with GC calculations in literature.
- The number of GCs is on average higher in the Virgo cluster than in Fornax. This is likely due to the difference in mass and the fact that the Fornax cluster is more evolved.
- The number of GCs and the S_N of galaxies in the Fornax core region are slightly higher than the outskirt regions which can be explained by the higher density in these regions. Higher density regions can have a higher S_N due to the increased GCs formation, decreased GCs destruction or effective quenching from the field stars formation.
- The S_N is significantly lower in the Fornax A group compared to the Fornax core. The Fornax A group contains a relatively large amount of late-type galaxies, but when considering only early-type galaxies the S_N remains lower in the Fornax A group.
- We find a higher number of GCs in early-type galaxies compared to late-type galaxies. This result is likely biased from the distribution of the early- and late-type galaxies. Early-type galaxies are located more in higher density regions which therefore could also lead to a higher number of GCs.
- The S_N is significantly higher in nucleated galaxies compared to non-nucleated galaxies. Also here the distribution of the galaxies plays an important role because the nucleated

galaxies are also located in higher density regions. The higher number of GCs in nucleated galaxies can also be linked to the formation of the nuclear star clusters. One possible formation mechanism for nuclear star clusters is the inspiralling of GCs which could explain the more metal poor population compared to the surrounding stars.

- Galaxies with a comparable stellar mass and a lower surface brightness have more GCs than galaxies with a high surface brightness. The number of nucleated galaxies is higher in the lower surface brightness groups than in the higher surface brightness group. The increase in the S_N for low surface brightness groups remains when we only consider the nucleated and non-nucleated galaxies separated.
- We present dark matter halo mass estimates for 194 dwarf galaxies based on their number of GCs.

References

Amorisco, N. C., Monachesi, A., Agnello, A., and White, S. D. M. (2018). The globular cluster systems of 54 Coma ultra-diffuse galaxies: statistical constraints from HST data. *MNRAS*, 475(3):4235–4251.

Bastian, N., Pfeffer, J., Kruijssen, J. M. D., Crain, R. A., Trujillo-Gomez, S., and Reina-Campos, M. (2020). The globular cluster system mass-halo mass relation in the E-MOSAICS simulations. *MNRAS*, 498(1):1050–1061.

Bastian, N., Gieles, M., Lamers, H. J. G. L. M., Scheepmaker, R. A., and de Grijs, R. (2005). The star cluster population of m - ii. age distribution and relations among the derived parameters. *A&A*, 431(3):905–924.

Beasley, M. A. and Trujillo, I. (2016a). GLOBULAR CLUSTERS INDICATE THAT ULTRA-DIFFUSE GALAXIES ARE DWARFS. *The Astrophysical Journal*, 830(1):23.

Beasley, M. A. and Trujillo, I. (2016b). GLOBULAR CLUSTERS INDICATE THAT ULTRA-DIFFUSE GALAXIES ARE DWARFS. *The Astrophysical Journal*, 830(1):23.

Behroozi, P. S., Conroy, C., and Wechsler, R. H. (2010). A COMPREHENSIVE ANALYSIS OF UNCERTAINTIES AFFECTING THE STELLAR MASS-HALO MASS RELATION FOR 0 <z< 4. *The Astrophysical Journal*, 717(1):379–403.

Bekki, K., Yahagi, H., and Forbes, D. A. (2006). The U-shaped Distribution of Globular Cluster-specific Frequencies in a Biased Globular Cluster Formation Scenario. *ApJL*, 645(1):L29–L32.

Bertin, E. and Arnouts, S. (1996). SExtractor: Software for source extraction. *AAPS*, 117:393–404.

Blakeslee, J. P., Jordán, A., Mei, S., Côté, P., Ferrarese, L., Infante, L., Peng, E. W., Tonry, J. L., and West, M. J. (2009). The ACS Fornax Cluster Survey. V. Measurement and Recalibration of Surface Brightness Fluctuations and a Precise Value of the Fornax-Virgo Relative Distance. *ApJ*, 694(1):556–572.

Cantiello, M., Venhola, A., Grado, A., Paolillo, M., D'Abrusco, R., Raimondo, G., Quintini, M., Hilker, M., Mieske, S., Tortora, C., Spavone, M., Capaccioli, M., Iodice, E., Peletier, R., Barroso, J. F., Limatola, L., Napolitano, N., Schipani, P., van de Ven, G., Gentile, F., and Covone, G. (2020). The Fornax Deep Survey with VST. IX. Catalog of sources in the FDS area with an example study for globular clusters and background galaxies. *AAP*, 639:A136.

Carleton, T., Guo, Y., Munshi, F., Tremmel, M., and Wright, A. (2021). An excess of globular clusters in Ultra-Diffuse Galaxies formed through tidal heating. *MNRAS*, 502(1):398–406.

Carlsten, S. G., Greene, J. E., Beaton, R. L., and Greco, J. P. (2021a). ELVES II: GCs and Nuclear Star Clusters of Dwarf Galaxies; The Importance of Environment. *arXiv e-prints*, page arXiv:2105.03440.

Carlsten, S. G., Greene, J. E., Peter, A. H. G., Beaton, R. L., and Greco, J. P. (2021b). Luminosity Functions and Host-to-host Scatter of Dwarf Satellite Systems in the Local Volume. *ApJ*, 908(1):109.

Carretta, E., Bragaglia, A., Gratton, R. G., Recio-Blanco, A., Lucatello, S., D'Orazi, V., and Cassisi, S. (2010). Properties of stellar generations in globular clusters and relations with global parameters ***. *A&A*, 516:A55.

Choksi, N. and Gnedin, O. Y. (2019). Origins of scaling relations of globular cluster systems. *MNRAS*, 488(4):5409–5419.

Cote, P., Blakeslee, J. P., Ferrarese, L., Jordan, A., Mei, S., Merritt, D., Milosavljević, M., Peng, E. W., Tonry, J. L., and West, M. J. (2004). The ACS virgo cluster survey. i. introduction to the survey. *The Astrophysical Journal Supplement Series*, 153(1):223–242.

Côté, P., Marzke, R. O., and West, M. J. (1998). The Formation of Giant Elliptical Galaxies and Their Globular Cluster Systems. *ApJ*, 501(2):554–570.

Côté, P., Marzke, R. O., West, M. J., and Minniti, D. (2000). Evidence for the Hierarchical Formation of the Galactic Spheroid. *ApJ*, 533(2):869–883.

Covey, K. R., Ivezić, Ž., Schlegel, D., Finkbeiner, D., Padmanabhan, N., Lupton, R. H., Agüeros, M. A., Bochanski, J. J., Hawley, S. L., West, A. A., Seth, A., Kimball, A., Gogarten, S. M., Claire, M., Haggard, D., Kaib, N., Schneider, D. P., and Sesar, B. (2007). Stellar SEDs from 0.3 to 2.5 μm: Tracing the Stellar Locus and Searching for Color Outliers in the SDSS and 2MASS. *AJ*, 134(6):2398–2417.

Dirsch, B., Richtler, T., Geisler, D., Forte, J. C., Bassino, L. P., and Gieren, W. P. (2003). The Globular Cluster System of NGC 1399. I. A Wide-Field Photometric Study. *AJ*, 125(4):1908–1925.

Dirsch, B., Schuberth, Y., and Richtler, T. (2005). A wide-field photometric study of the globular cluster system of NGC 4636. *AAP*, 433(1):43–56.

Dirsch, B., Richtler, T., and Bassino, L. P. (2003). The globular cluster systems of ngc 3258 and ngc 3268 in the antlia cluster*. *A&A*, 408(3):929–939.

Drinkwater, M. J., Gregg, M. D., and Colless, M. (2001). Substructure and Dynamics of the Fornax Cluster. *ApJL*, 548(2):L139–L142.

Durrell, P. R., Harris, W. E., Geisler, D., and Pudritz, R. E. (1996). Globular Cluster Systems in Dwarf Elliptical Galaxies. II. The Virgo Cluster. *AJ*, 112:972.

Eigenthaler, P., Puzia, T., Taylor, M., Ordenes-Briceño, Y., Muñoz, R., Ribbeck, K., Alamo-Martínez, K., Zhang, H., Ángel, S., Capaccioli, M., Côté, P., Ferrarese, L., Galaz, G., Grebel, E., Hempel, M., Hilker, M., Lançon, A., Mieske, S., Miller, B., and Spengler, C. (2018). The next generation fornax survey (ngfs). ii. the central dwarf galaxy population. *The Astrophysical Journal*, 855.

El-Badry, K., Quataert, E., Weisz, D. R., Choksi, N., and Boylan-Kolchin, M. (2019). The formation and hierarchical assembly of globular cluster populations. *MNRAS*, 482(4):4528–4552.

Elmegreen, B. G. (2010). THE GLOBULAR CLUSTER MASS FUNCTION AS a REMNANT OF VIOLENT BIRTH. *The Astrophysical Journal*, 712(2):L184–L188.

Elmegreen, B. G. and Efremov, Y. N. (1997). A universal formation mechanism for open and globular clusters in turbulent gas. *The Astrophysical Journal*, 480(1):235–245.

Fahrion, K., Lyubenova, M., van de Ven, G., Leaman, R., Hilker, M., Martín-Navarro, I., Zhu, L., Alfaro-Cuello, M., Coccato, L., Corsini, E. M., Falcón-Barroso, J., Iodice, E., McDermid, R. M., Sarzi, M., and de Zeeuw, T. (2019). Constraining nuclear star cluster formation using MUSE-AO observations of the early-type galaxy FCC 47. *AAP*, 628:A92.

Fall, S. M., Chandar, R., and Whitmore, B. C. (2005). The age distribution of massive star clusters in the antennae galaxies. *The Astrophysical Journal*, 631(2):L133–L136.

Fall, S. M. and Rees, M. J. (1977). Survival and disruption of galactic substructure. *MNRAS*, 181:37P–42P.

Fall, S. M. and Zhang, Q. (2001). Dynamical evolution of the mass function of globular star clusters. *The Astrophysical Journal*, 561(2):751–765.

Ferguson, H. C. (1989). Population Studies in Groups and Clusters of Galaxies. II. A Catalog of Galaxies in the Central 3.5 Degrees of the Fornax Cluster. *AJ*, 98:367.

Ferguson, H. C. and Sandage, A. (1989). The Spatial Distributions and Intrinsic Shapes of Dwarf Elliptical Galaxies in the Virgo and Fornax Clusters. *ApJL*, 346:L53.

Ferrarese, L., Côté, P., Cuillandre, J.-C., Gwyn, S. D. J., Peng, E. W., MacArthur, L. A., Duc, P.-A., Boselli, A., Mei, S., Erben, T., McConnachie, A. W., Durrell, P. R., Mihos, J. C., Jordán, A., Lançon, A., Puzia, T. H., Emsellem, E., Balogh, M. L., Blakeslee, J. P., van Waerbeke, L., Gavazzi, R., Vollmer, B., Kavelaars, J. J., Woods, D., Ball, N. M., Boissier, S., Courteau, S., Ferriere, E., Gavazzi, G., Hildebrandt, H., Hudelot, P., Huertas-Company, M., Liu, C., McLaughlin, D., Mellier, Y., Milkeraitis, M., Schade, D., Balkowski, C., Bournaud, F., Carlberg, R. G., Chapman, S. C., Hoekstra, H., Peng, C., Sawicki, M., Simard, L., Taylor, J. E., Tully, R. B., van Driel, W., Wilson, C. D., Burdullis, T., Mahoney, B., and Manset, N. (2012). THE NEXT GENERATION VIRGO CLUSTER SURVEY (NGVS). i. INTRODUCTION TO THE SURVEY. *The Astrophysical Journal Supplement Series*, 200(1):4.

Ferrarese, L., Côté, P., MacArthur, L. A., Durrell, P. R., Gwyn, S. D. J., Duc, P.-A., Sánchez-Janssen, R., Santos, M., Blakeslee, J. P., Boselli, A., Boyer, F., Cantiello, M., Courteau, S., Cuillandre, J.-C., Emsellem, E., Erben, T., Gavazzi, G., Guhathakurta, P., Huertas-Company, M., Jordán, A., Lançon, A., Liu, C., Mei, S., Mihos, J. C., Peng, E. W., Puzia, T. H., Roediger, J., Schade, D., Taylor, J. E., Toloba, E., and Zhang, H. (2020). The Next Generation Virgo Cluster Survey (NGVS). XIV. The Discovery of Low-mass Galaxies and a New Galaxy Catalog in the Core of the Virgo Cluster. *ApJ*, 890(2):128.

Forbes, D. A., Brodie, J. P., and Huchra, J. (1996). Globular Cluster Luminosity Functions and the Hubble Constant from WFPC2 Imaging: The Dominant Group Elliptical NGC 5846. *AJ*, 112:2448.

Gaia Collaboration, Brown, A. G. A., Vallenari, A., Prusti, T., de Bruijne, J. H. J., Babusiaux, C., Bailer-Jones, C. A. L., Biermann, M., Evans, D. W., Eyer, L., Jansen, F., Jordi, C., Klioner, S. A., Lammers, U., Lindegren, L., Luri, X., Mignard, F., Panem, C., Pourbaix, D., Randich, S., Sartoretti, P., Siddiqui, H. I., Soubiran, C., van Leeuwen, F., Walton, N. A., Arenou, F., Bastian, U., Cropper, M., Drimmel, R., Katz, D., Lattanzi, M. G., Bakker, J., Cacciari, C., Castañeda, J., Chaoul, L., Cheek, N., De Angeli, F., Fabricius, C., Guerra, R., Holl, B., Masana, E., Messineo, R., Mowlavi, N., Nienartowicz, K., Panuzzo, P., Portell, J., Riello, M., Seabroke, G. M., Tanga, P., Thévenin, F., Gracia-Abril, G., Comoretto, G., Garcia-Reinaldos, M., Teyssier, D., Altmann, M., Andrae, R., Audard, M., Bellas-Velidis, I., Benson,

K., Berthier, J., Blomme, R., Burgess, P., Busso, G., Carry, B., Cellino, A., Clementini, G., Clotet, M., Creevey, O., Davidson, M., De Ridder, J., Delchambre, L., Dell'Oro, A., Ducourant, C., Fernández-Hernández, J., Fouesneau, M., Frémat, Y., Galluccio, L., García-Torres, M., González-Núñez, J., González-Vidal, J. J., Gosset, E., Guy, L. P., Halbwachs, J. L., Hambly, N. C., Harrison, D. L., Hernández, J., Hestroffer, D., Hodgkin, S. T., Hutton, A., Jasniewicz, G., Jean-Antoine-Piccolo, A., Jordan, S., Korn, A. J., Krone-Martins, A., Lanzafame, A. C., Lebzelter, T., Löffler, W., Manteiga, M., Marrese, P. M., Martín-Fleitas, J. M., Moitinho, A., Mora, A., Muinonen, K., Osinde, J., Pancino, E., Pauwels, T., Petit, J. M., Recio-Blanco, A., Richards, P. J., Rimoldini, L., Robin, A. C., Sarro, L. M., Siopis, C., Smith, M., Sozzetti, A., Süveges, M., Torra, J., van Reeven, W., Abbas, U., Abreu Aramburu, A., Accart, S., Aerts, C., Altavilla, G., Álvarez, M. A., Alvarez, R., Alves, J., Anderson, R. I., Andrei, A. H., Anglada Varela, E., Antiche, E., Antoja, T., Arcay, B., Astraatmadja, T. L., Bach, N., Baker, S. G., Balaguer-Núñez, L., Balm, P., Barache, C., Barata, C., Barbato, D., Barblan, F., Barklem, P. S., Barrado, D., Barros, M., Barstow, M. A., Bartholomé Muñoz, S., Bassilana, J. L., Becciani, U., Bellazzini, M., Berihuete, A., Bertone, S., Bianchi, L., Bienaymé, O., Blanco-Cuaresma, S., Boch, T., Boeche, C., Bombrun, A., Borrachero, R., Bossini, D., Bouquillon, S., Bourda, G., Bragaglia, A., Bramante, L., Breddels, M. A., Bressan, A., Brouillet, N., Brüsemeister, T., Brugaletta, E., Bucciarelli, B., Burlacu, A., Busonero, D., Butkevich, A. G., Buzzi, R., Caffau, E., Cancelliere, R., Cannizzaro, G., Cantat-Gaudin, T., Carballo, R., Carlucci, T., Carrasco, J. M., Casamiquela, L., Castellani, M., Castro-Ginard, A., Charlot, P., Chemin, L., Chiavassa, A., Cocozza, G., Costigan, G., Cowell, S., Crifo, F., Crosta, M., Crowley, C., Cuypers, J., Dafonte, C., Damerdji, Y., Dapergolas, A., David, P., David, M., de Laverny, P., De Luise, F., De March, R., de Martino, D., de Souza, R., de Torres, A., Debosscher, J., del Pozo, E., Delbo, M., Delgado, A., Delgado, H. E., Di Matteo, P., Diakite, S., Diener, C., Distefano, E., Dolding, C., Drazinos, P., Durán, J., Edvardsson, B., Enke, H., Eriksson, K., Esquej, P., Eynard Bontemps, G., Fabre, C., Fabrizio, M., Faigler, S., Falcão, A. J., Farràs Casas, M., Federici, L., Fedorets, G., Fernique, P., Figueras, F., Filippi, F., Findeisen, K., Fonti, A., Fraile, E., Fraser, M., Frézouls, B., Gai, M., Galleti, S., Garabato, D., García-Sedano, F., Garofalo, A., Garralda, N., Gavel, A., Gavras, P., Gerssen, J., Geyer, R., Giacobbe, P., Gilmore, G., Girona, S., Giuffrida, G., Glass, F., Gomes, M., Granvik, M., Gueguen, A., Guerrier, A., Guiraud, J., Gutiérrez-Sánchez, R., Haigron, R., Hatzidimitriou, D., Hauser, M., Haywood, M., Heiter, U., Helmi, A., Heu, J., Hilger, T., Hobbs, D., Hofmann, W., Holland, G., Huckle, H. E., Hypki, A., Icardi, V., Janßen, K., Jevardat de Fombelle, G., Jonker, P. G., Juhász, Á. L., Julbe, F., Karampelas, A., Kewley, A., Klar, J., Kochoska, A., Kohley, R., Kolenberg, K., Kontizas, M., Kontizas, E., Koposov, S. E., Kordopatis, G., Kostrzewa-Rutkowska, Z., Koubsky, P., Lambert, S., Lanza, A. F., Lasne, Y., Lavigne, J. B., Le Fustec, Y., Le Poncin-Lafitte, C., Lebreton, Y., Leccia, S., Leclerc, N., Lecoeur-Taibi, I., Lenhardt, H., Leroux, F., Liao, S., Licata, E., Lindstrøm, H. E. P., Lister, T. A., Livanou, E., Lobel, A., López, M., Managau, S., Mann, R. G., Mantelet, G., Marchal, O., Marchant, J. M., Marconi, M., Marinoni, S., Marschalkó, G., Marshall, D. J., Martino, M., Marton, G., Mary, N., Massari, D., Matijevič, G., Mazeh, T., McMillan, P. J., Messina, S., Michalik, D., Millar, N. R., Molina, D., Molinaro, R., Molnár, L., Montegriffo, P., Mor, R., Morbidelli, R., Morel, T., Morris, D., Mulone, A. F., Muraveva, T., Musella, I., Nelemans, G., Nicastro, L., Noval, L., O'Mullane, W., Ordénovic, C., Ordóñez-Blanco, D., Osborne, P., Pagani, C., Pagano, I., Pailler, F., Palacin, H., Palaversa, L., Panahi, A., Pawlak, M., Piersimoni, A. M., Pineau, F. X., Plachy, E., Plum, G., Poggio, E., Poujoulet, E., Prša, A., Pulone, L., Racero, E., Ragaini, S., Rambaux, N., Ramos-Lerate, M., Regibo, S., Reylé, C., Riclet, F., Ripepi, V., Riva, A., Rivard, A., Rixon, G., Roegiers, T., Roelens, M., Romero-Gómez, M., Rowell,

N., Royer, F., Ruiz-Dern, L., Sadowski, G., Sagristà Sellés, T., Sahlmann, J., Salgado, J., Salguero, E., Sanna, N., Santana-Ros, T., Sarasso, M., Savietto, H., Schultheis, M., Sciacca, E., Segol, M., Segovia, J. C., Ségransan, D., Shih, I. C., Siltala, L., Silva, A. F., Smart, R. L., Smith, K. W., Solano, E., Solitro, F., Sordo, R., Soria Nieto, S., Souchay, J., Spagna, A., Spoto, F., Stampa, U., Steele, I. A., Steidelmüller, H., Stephenson, C. A., Stoev, H., Suess, F. F., Surdej, J., Szabados, L., Szegedi-Elek, E., Tapiador, D., Taris, F., Tauran, G., Taylor, M. B., Teixeira, R., Terrett, D., Teyssandier, P., Thuillot, W., Titarenko, A., Torra Clotet, F., Turon, C., Ulla, A., Utrilla, E., Uzzi, S., Vaillant, M., Valentini, G., Valette, V., van Elteren, A., Van Hemelryck, E., van Leeuwen, M., Vaschetto, M., Vecchiato, A., Veljanoski, J., Viala, Y., Vicente, D., Vogt, S., von Essen, C., Voss, H., Votruba, V., Voutsinas, S., Walmsley, G., Weiler, M., Wertz, O., Wevers, T., Wyrzykowski, Ł., Yoldas, A., Žerjal, M., Ziaeepour, H., Zorec, J., Zschocke, S., Zucker, S., Zurbach, C., and Zwitter, T. (2018). Gaia Data Release 2. Summary of the contents and survey properties. *AAP*, 616:A1.

Georgiev, I. Y., Goudfrooij, P., Puzia, T. H., and Hilker, M. (2008). Old Globular Clusters in Magellanic-Type Dwarf Irregular Galaxies. *AJ*, 135(5):1858–1876.

Georgiev, I. Y., Puzia, T. H., Goudfrooij, P., and Hilker, M. (2010). Globular cluster systems in nearby dwarf galaxies – III. Formation efficiencies of old globular clusters*. *Monthly Notices of the Royal Astronomical Society*, 406(3):1967–1984.

Georgiev, I. Y., Puzia, T. H., Hilker, M., and Goudfrooij, P. (2009). Globular cluster systems in nearby dwarf galaxies - I. HST/ACS observations and dynamical properties of globular clusters at low environmental density. *MNRAS*, 392(2):879–893.

Goddard, Q. E., Bastian, N., and Kennicutt, R. C. (2010). On the fraction of star clusters surviving the embedded phase. *MNRAS*, 405(2):857–869.

Guérou, A., Emsellem, E., McDermid, R. M., Côté, P., Ferrarese, L., Blakeslee, J. P., Durrell, P. R., MacArthur, L. A., Peng, E. W., Cuillandre, J.-C., and Gwyn, S. (2015). THE NEXT GENERATION VIRGO CLUSTER SURVEY. XII. STELLAR POPULATIONS AND KINEMATICS OF COMPACT, LOW-MASS EARLY-TYPE GALAXIES FROM GEMINI GMOS-IFU SPECTROSCOPY. *The Astrophysical Journal*, 804(1):70.

Hamraz, E., Peletier, R. F., Khosroshahi, H. G., Valentijn, E. A., den Brok, M., and Venhola, A. (2019). Young stellar populations in early-type dwarf galaxies. *Astronomy & Astrophysics*, 625:A94.

Hanisch, R. J. (1989). *STSDAS: The Space Telescope Science Data Analysis System*, pages 129–140. Springer US, Boston, MA.

Harris, G. L. H., Harris, W. E., and Geisler, D. (2004). Wide-Field Washington Photometry of the NGC 5128 Globular Cluster System. II. Large-Scale Properties of the System. *AJ*, 128(2):723–735.

Harris, W. E. (1996). A Catalog of Parameters for Globular Clusters in the Milky Way. *AJ*, 112:1487.

Harris, W. E., Blakeslee, J. P., and Harris, G. L. H. (2017). Galactic dark matter halos and globular cluster populations. III. extension to extreme environments. *The Astrophysical Journal*, 836(1):67.

Harris, W. E., Harris, G. L., and Hudson, M. J. (2015). DARK MATTER HALOS IN GALAXIES AND GLOBULAR CLUSTER POPULATIONS. II. METALLICITY AND MORPHOLOGY. *The Astrophysical Journal*, 806(1):36.

Harris, W. E., Harris, G. L. H., and Alessi, M. (2013). A CATALOG OF GLOBULAR CLUSTER SYSTEMS: WHAT DETERMINES THE SIZE OF a GALAXY's GLOBULAR CLUSTER POPULATION? *The Astrophysical Journal*, 772(2):82.

Harris, W. E. and van den Bergh, S. (1981). Globular clusters in galaxies beyond the local group. I. New cluster systems in selected northern ellipticals. *AJ*, 86:1627–1642.

Hilker, M., Baumgardt, H., Infante, L., Drinkwater, M., Evstigneeva, E., and Gregg, M. (2007). Dynamical masses of ultra-compact dwarf galaxies in Fornax. *AAP*, 463(1):119–130.

Holtzman, J. A., Faber, S. M., Shaya, E. J., Lauer, T. R., Groth, J., Hunter, D. A., Baum, W. A., Ewald, S. P., Hester, J. J., Light, R. M., Lynds, C. R., O'Neil, E. J., J., and Westphal, J. A. (1992). Planetary Camera Observations of NGC 1275: Discovery of a Central Population of Compact Massive Blue Star Clusters. *AJ*, 103:691.

Hudson, M. J., Harris, G. L., and Harris, W. E. (2014). DARK MATTER HALOS IN GALAXIES AND GLOBULAR CLUSTER POPULATIONS. *The Astrophysical Journal*, 787(1):L5.

Iodice, E., Capaccioli, M., Grado, A., Limatola, L., Spavone, M., Napolitano, N. R., Paolillo, M., Peletier, R. F., Cantiello, M., Lisker, T., Wittmann, C., Venhola, A., Hilker, M., D'Abrusco, R., Pota, V., and Schipani, P. (2016). The Fornax Deep Survey with VST. I. The Extended and Diffuse Stellar Halo of NGC 1399 out to 192 kpc. *ApJ*, 820(1):42.

Jester, S., Schneider, D. P., Richards, G. T., Green, R. F., Schmidt, M., Hall, P. B., Strauss, M. A., Vanden Berk, D. E., Stoughton, C., Gunn, J. E., Brinkmann, J., Kent, S. M., Smith, J. A., Tucker, D. L., and Yanny, B. (2005). The Sloan Digital Sky Survey View of the Palomar-Green Bright Quasar Survey. *AJ*, 130(3):873–895.

Johnston, E., Puzia, T., D'Ago, G., Eigenthaler, P., Galaz, G., Häußler, B., Mora, M., Ordenes-Briceño, Y., Rong, Y., Spengler, C., Vogt, F., Côté, P., Grebel, E., Hilker, M., Mieske, S., Miller, B., Sánchez-Janssen, R., Taylor, M., and Zhang, H. (2020). The next generation fornax survey (ngfs): Vii. a muse view of the nuclear star clusters in fornax dwarf galaxies. *Monthly Notices of the Royal Astronomical Society*, 495:2247–2264.

Jordan, A., Blakeslee, J. P., Cote, P., Ferrarese, L., Infante, L., Mei, S., Merritt, D., Peng, E. W., Tonry, J. L., and West, M. J. (2007). The ACS fornax cluster survey. i. introduction to the survey and data reduction procedures. *The Astrophysical Journal Supplement Series*, 169(2):213–224.

Jordán, A., Peng, E., Blakeslee, J., Côté, P., Eyheramendy, S., and Ferrarese, L. (2015). The acs fornax cluster survey. xi. catalog of globular cluster candidates. *The Astrophysical Journal Supplement Series*, 221:13.

Kacharov, N., Neumayer, N., Seth, A. C., Cappellari, M., McDermid, R., Walcher, C. J., and Böker, T. (2018). Stellar populations and star formation histories of the nuclear star clusters in six nearby galaxies. *MNRAS*, 480(2):1973–1998.

Kashibadze, Olga G., Karachentsev, Igor D., and Karachentseva, Valentina E. (2020). Structure and kinematics of the virgo cluster of galaxies. *A&A*, 635:A135.

Kim, J.-h., Ma, X., Grudić, M. Y., Hopkins, P. F., Hayward, C. C., Wetzel, A., Faucher-Giguère, C.-A., Kereš, D., Garrison-Kimmel, S., and Murray, N. (2018). Formation of globular cluster candidates in merging proto-galaxies at high redshift: a view from the FIRE cosmological simulations. *MNRAS*, 474(3):4232–4244.

Kimm, T., Cen, R., Rosdahl, J., and Yi, S. K. (2016). Formation of Globular Clusters in Atomic-cooling Halos Via Rapid Gas Condensation and Fragmentation during the Epoch of Reionization. *ApJ*, 823(1):52.

Kissler-Patig, M., Kohle, S., Hilker, M., Richtler, T., Infante, L., and Quintana, H. (1997). Globular cluster systems of early-type galaxies in Fornax. *AAP*, 319:470–480.

Kissler-Patig, M., Richtler, T., and Hilker, M. (1996). The elliptical globular cluster system of NGC 720. *AAP*, 308:704–712.

Kourkchi, E. and Tully, R. B. (2017). Galaxy groups within 3500 km s-1. *The Astrophysical Journal*, 843(1):16.

Kron, R. G. (1980). Photometry of a complete sample of faint galaxies. *ApJS*, 43:305–325.

Kruijssen, J. M. D. (2012). On the fraction of star formation occurring in bound stellar clusters. *MNRAS*, 426(4):3008–3040.

Kruijssen, J. M. D. (2015). Globular clusters as the relics of regular star formation in 'normal' high-redshift galaxies. *MNRAS*, 454(2):1658–1686.

Kruijssen, J. M. D., Pfeffer, J. L., Crain, R. A., and Bastian, N. (2019). The E-MOSAICS project: tracing galaxy formation and assembly with the age-metallicity distribution of globular clusters. *MNRAS*, 486(3):3134–3179.

Kuijken, K., Bender, R., Cappellaro, E., Muschielok, B., Baruffolo, A., Cascone, E., Iwert, O., Mitsch, W., Nicklas, H., Valentijn, E., Baade, D., Begeman, K., Bortolussi, A., Boxhoorn, D., Christen, F., Deul, E., Geimer, C., Greggio, L., Harke, R., Häfner, R., Hess, G., Hess, H.-J., Hopp, U., Ilijevski, I., Klink, G., Kravcar, H., Lizon, J., Magagna, C., Müller, P., Niemeczek, R., de Pizzol, L., Poschmann, H., Reif, K., Rengelink, R., Reyes, J., Silber, A., and Wellem, W. (2002). Omegacam: the 16k×16k ccd camera for the vlt survey telescope. *The Messenger*, 110(December 2002):15–18.

Larsen, S. S., Brodie, J. P., Grundahl, F., and Strader, J. (2014). NITROGEN ABUNDANCES AND MULTIPLE STELLAR POPULATIONS IN THE GLOBULAR CLUSTERS OF THE FORNAX dSph. *The Astrophysical Journal*, 797(1):15.

Leaman, R., VandenBerg, D. A., and Mendel, J. T. (2013). The bifurcated age-metallicity relation of Milky Way globular clusters and its implications for the accretion history of the galaxy. *MNRAS*, 436(1):122–135.

Letarte, B., Hill, V., Jablonka, P., Tolstoy, E., François, P., and Meylan, G. (2006). VLT/UVES spectroscopy of individual stars in three globular clusters in the Fornax dwarf spheroidal galaxy. *AAP*, 453(2):547–554.

Li, H., Gnedin, O. Y., Gnedin, N. Y., Meng, X., Semenov, V. A., and Kravtsov, A. V. (2017). STAR CLUSTER FORMATION IN COSMOLOGICAL SIMULATIONS. i. PROPERTIES OF YOUNG CLUSTERS. *The Astrophysical Journal*, 834(1):69.

Lim, S., Peng, E. W., Côté, P., Sales, L. V., den Brok, M., Blakeslee, J. P., and Guhathakurta, P. (2018). The globular cluster systems of ultra-diffuse galaxies in the coma cluster. *The Astrophysical Journal*, 862(1):82.

Liu, Y., Peng, E. W., Blakeslee, J., Côté, P., Ferrarese, L., Jordán, A., Puzia, T. H., Toloba, E., and Zhang, H.-X. (2016). EVIDENCE FOR THE RAPID FORMATION OF LOW-MASS EARLY-TYPE GALAXIES IN DENSE ENVIRONMENTS. *The Astrophysical Journal*, 818(2):179.

Liu, Y., Peng, E. W., Jordán, A., Blakeslee, J. P., Côté, P., Ferrarese, L., and Puzia, T. H. (2019). The ACS Fornax Cluster Survey. III. Globular Cluster Specific Frequencies of Early-type Galaxies. *ApJ*, 875(2):156.

Lotz, J. M., Miller, B. W., and Ferguson, H. C. (2004). The Colors of Dwarf Elliptical Galaxy Globular Cluster Systems, Nuclei, and Stellar Halos. *ApJ*, 613(1):262–278.

Mieske, S., Hilker, M., and Infante, L. (2004). Fornax compact object survey fcos: On the nature of ultra compact dwarf galaxies. *A&A*, 418(2):445–458.

Miller, B. W. and Lotz, J. M. (2005). Globular Cluster Luminosity Functions and Specific Frequencies in Dwarf Elliptical Galaxies. In *American Astronomical Society Meeting Abstracts*, volume 207 of *American Astronomical Society Meeting Abstracts*, page 128.17.

Miller, B. W. and Lotz, J. M. (2007). The globular cluster luminosity function and specific frequency in dwarf elliptical galaxies. *The Astrophysical Journal*, 670(2):1074–1089.

Mistani, P. A., Sales, L. V., Pillepich, A., Sanchez-Janssen, R., Vogelsberger, M., Nelson, D., Rodriguez-Gomez, V., Torrey, P., and Hernquist, L. (2016). On the assembly of dwarf galaxies in clusters and their efficient formation of globular clusters. *MNRAS*, 455(3):2323–2336.

Moore, B., Lake, G., and Katz, N. (1998). Morphological transformation from galaxy harassment. *The Astrophysical Journal*, 495(1):139–151.

National Optical Astronomy Observatories (1999). IRAF: Image Reduction and Analysis Facility.

Neumayer, N., Seth, A., and Böker, T. (2020). Nuclear star clusters. *AAPR*, 28(1):4.

Ordenes-Briceño, Y., Eigenthaler, P., Taylor, M. A., Puzia, T. H., Alamo-Martínez, K., Ribbeck, K. X., Muñoz, R. P., Zhang, H., Grebel, E. K., Ángel, S., Côté, P., Ferrarese, L., Hilker, M., Lançon, A., Mieske, S., Miller, B. W., Rong, Y., and Sánchez-Janssen, R. (2018). The next generation fornax survey (NGFS). III. revealing the spatial substructure of the dwarf galaxy population inside half of fornax's virial radius. *The Astrophysical Journal*, 859(1):52.

Peebles, P. J. E. and Dicke, R. H. (1968). Origin of the Globular Star Clusters. *ApJ*, 154:891.

Peng, C. Y., Ho, L. C., Impey, C. D., and Rix, H.-W. (2002). Detailed Structural Decomposition of Galaxy Images. *AJ*, 124(1):266–293.

Peng, C. Y., Ho, L. C., Impey, C. D., and Rix, H.-W. (2010). Detailed Decomposition of Galaxy Images. II. Beyond Axisymmetric Models. *AJ*, 139(6):2097–2129.

Peng, E. W., Ferguson, H. C., Goudfrooij, P., Hammer, D., Lucey, J. R., Marzke, R. O., Puzia, T. H., Carter, D., Balcells, M., Bridges, T., Chiboucas, K., del Burgo, C., Graham, A. W., Guzmán, R., Hudson, M. J., Matković, A., Merritt, D., Miller, B. W., Mouhcine, M., Phillipps,

S., Sharples, R., Smith, R. J., Tully, B., and Kleijn, G. V. (2011). THEHST/ACS COMA CLUSTER SURVEY. IV. INTERGALACTIC GLOBULAR CLUSTERS AND THE MASSIVE GLOBULAR CLUSTER SYSTEM AT THE CORE OF THE COMA GALAXY CLUSTER. *The Astrophysical Journal*, 730(1):23.

Peng, E. W., Jordán, A., Côté, P., Takamiya, M., West, M. J., Blakeslee, J. P., Chen, C.-W., Ferrarese, L., Mei, S., Tonry, J. L., and West, A. A. (2008). The ACS virgo cluster survey. XV. the formation efficiencies of globular clusters in early-type galaxies: The effects of mass and environment. *The Astrophysical Journal*, 681(1):197–224.

Peng, E. W. and Lim, S. (2016). A RICH GLOBULAR CLUSTER SYSTEM IN DRAGONFLY 17: ARE ULTRA-DIFFUSE GALAXIES PURE STELLAR HALOS? *The Astrophysical Journal*, 822(2):L31.

Peterson, C. J. and King, I. R. (1975). The structure of star clusters. VI. Observed radii and structural parameters in globular clusters. *AJ*, 80:427–436.

Pfeffer, J., Kruijssen, J. M. D., Crain, R. A., and Bastian, N. (2018). The E-MOSAICS project: simulating the formation and co-evolution of galaxies and their star cluster populations. *MNRAS*, 475(4):4309–4346.

Prole, D. J., Davies, J. I., Keenan, O. C., and Davies, L. J. M. (2018). Automated detectionof very low surface brightness galaxiesin the Virgo cluster. *MNRAS*, 478(1):667–681.

Prole, D. J., Hilker, M., van der Burg, R. F. J., Cantiello, M., Venhola, A., Iodice, E., van de Ven, G., Wittmann, C., Peletier, R. F., Mieske, S., Capaccioli, M., Napolitano, N. R., Paolillo, M., Spavone, M., and Valentijn, E. (2019). Halo mass estimates from the globular cluster populations of 175 low surface brightness galaxies in the Fornax cluster. *MNRAS*, 484(4):4865–4880.

Renaud, F., Agertz, O., and Gieles, M. (2017). The origin of the Milky Way globular clusters. *MNRAS*, 465(3):3622–3636.

Rhode, K. L. and Zepf, S. E. (2004). The Globular Cluster Systems of the Early-Type Galaxies NGC 3379, NGC 4406, and NGC 4594 and Implications for Galaxy Formation. *AJ*, 127(1):302–317.

Rhode, K. L., Zepf, S. E., and Santos, M. R. (2005). Metal-poor Globular Clusters and the Formation of Their Host Galaxies. *ApJL*, 630(1):L21–L24.

Rhode, K. L., Zepf, S. E., and Santos, M. R. (2005). Metal-poor globular clusters and the formation of their host galaxies. *The Astrophysical Journal*, 630(1):L21–L24.

Saifollahi, T., Janz, J., Peletier, R. F., Cantiello, M., Hilker, M., Mieske, S., Valentijn, E. A., Venhola, A., and Kleijn, G. V. (2021). Ultra-compact dwarfs beyond the centre of the Fornax galaxy cluster: hints of UCD formation in low-density environments. *MNRAS*, 504(3):3580–3609.

Sánchez-Janssen, R. and Aguerri, J. A. L. (2012). Globular cluster systems as tracers of environmental effects on Virgo early-type dwarfs. *MNRAS*, 424(4):2614–2624.

Sánchez-Janssen, R., Côté, P., Ferrarese, L., Peng, E. W., Roediger, J., Blakeslee, J. P., Emsellem, E., Puzia, T. H., Spengler, C., Taylor, J., Álamo-Martínez, K. A., Boselli, A., Cantiello, M., Cuillandre, J.-C., Duc, P.-A., Durrell, P., Gwyn, S., MacArthur, L. A., Lançon, A., Lim, S., Liu, C., Mei, S., Miller, B., Muñoz, R., Mihos, J. C., Paudel, S., Powalka, M., and Toloba, E. (2019). The next generation virgo cluster survey. XXIII. fundamentals of nuclear star clusters over seven decades in galaxy mass. *The Astrophysical Journal*, 878(1):18.

Schipani, P., Capaccioli, M., Arcidiacono, C., Argomedo, J., Dall'Ora, M., D'Orsi, S., Farinato, J., Magrin, D., Marty, L., Ragazzoni, R., and Umbriaco, G. (2012). VST: from commissioning to science. In Stepp, L. M., Gilmozzi, R., and Hall, H. J., editors, *Ground-based and Airborne Telescopes IV*, volume 8444, pages 468 – 477. International Society for Optics and Photonics, SPIE.

Scott, D. (2015). *Multivariate density estimation: Theory, practice, and visualization: Second edition.*

Searle, L. and Zinn, R. (1978). Composition of halo clusters and the formation of the galactic halo. *ApJ*, 225:357–379.

Seth, A. C., Cappellari, M., Neumayer, N., Caldwell, N., Bastian, N., Olsen, K., Blum, R. D., Debattista, V. P., McDermid, R., Puzia, T., and Stephens, A. (2010). The NGC 404 Nucleus: Star Cluster and Possible Intermediate-mass Black Hole. *ApJ*, 714(1):713–731.

Smith, R., Sánchez-Janssen, R., Beasley, M. A., Candlish, G. N., Gibson, B. K., Puzia, T. H., Janz, J., Knebe, A., Aguerri, J. A. L., Lisker, T., Hensler, G., Fellhauer, M., Ferrarese, L., and Yi, S. K. (2015). The sensitivity of harassment to orbit: mass loss from early-type dwarfs in galaxy clusters. *MNRAS*, 454(3):2502–2516.

Spitler, L. R. and Forbes, D. A. (2009). A new method for estimating dark matter halo masses using globular cluster systems. *MNRAS*, 392(1):L1–L5.

Spitler, L. R., Forbes, D. A., Strader, J., Brodie, J. P., and Gallagher, J. S. (2008). The connection between globular cluster systems and their host galaxy and environment: a case study of the isolated elliptical NGC 821. *MNRAS*, 385(1):361–380.

Su, A., Salo, H., Janz, J., Laurikainen, E., Venhola, A., Peletier, R., Iodice, E., Hilker, M., Cantiello, M., Napolitano, N., Spavone, M., Raj, M., van de Ven, G., Mieske, S., Paolillo, M., Capaccioli, M., Valentijn, E., and Watkins, A. (2021). The fornax deep survey (fds) with the vst xi. the search for signs of preprocessing between the fornax main cluster and fornax a group. *Astronomy & astrophysics*.

Taylor, E. N., Hopkins, A. M., Baldry, I. K., Brown, M. J. I., Driver, S. P., Kelvin, L. S., Hill, D. T., Robotham, A. S. G., Bland-Hawthorn, J., Jones, D. H., Sharp, R. G., Thomas, D., Liske, J., Loveday, J., Norberg, P., Peacock, J. A., Bamford, S. P., Brough, S., Colless, M., Cameron, E., Conselice, C. J., Croom, S. M., Frenk, C. S., Gunawardhana, M., Kuijken, K., Nichol, R. C., Parkinson, H. R., Phillipps, S., Pimbblet, K. A., Popescu, C. C., Prescott, M., Sutherland, W. J., Tuffs, R. J., van Kampen, E., and Wijesinghe, D. (2011). Galaxy And Mass Assembly (GAMA): stellar mass estimates. *MNRAS*, 418(3):1587–1620.

Tremaine, S. D., Ostriker, J. P., and Spitzer, L., J. (1975). The formation of the nuclei of galaxies. I. M31. *ApJ*, 196:407–411.

van Dokkum, P., Abraham, R., Romanowsky, A. J., Brodie, J., Conroy, C., Danieli, S., Lokhorst, D., Merritt, A., Mowla, L., and Zhang, J. (2017). Extensive globular cluster systems associated with ultra diffuse galaxies in the coma cluster. *The Astrophysical Journal*, 844(1):L11.

Venhola, A., Peletier, R., Laurikainen, E., Salo, H., Iodice, E., Mieske, S., Hilker, M., Wittmann, C., Lisker, T., Paolillo, M., Cantiello, M., Janz, J., Spavone, M., D'Abrusco, R., van de Ven, G., Napolitano, N., Verdoes Kleijn, G., Maddox, N., Capaccioli, M., Grado, A., Valentijn, E., Falcon-Barroso, J., and Limatola, L. (2018a). VizieR Online Data Catalog: Fornax Deep Survey with VST. IV. dwarf galaxies (Venhola+, 2018). *VizieR Online Data Catalog*, pages J/A+A/620/A165.

Venhola, A., Peletier, R., Laurikainen, E., Salo, H., Iodice, E., Mieske, S., Hilker, M., Wittmann, C., Lisker, T., Paolillo, M., Cantiello, M., Janz, J., Spavone, M., D'Abrusco, R., Ven, G., Napolitano, N., Kleijn, G., Maddox, N., Capaccioli, M., Grado, A., Valentijn, E., Falcón-Barroso, J., and Limatola, L. (2018b). The Fornax Deep Survey with the VST. IV. A size and magnitude limited catalog of dwarf galaxies in the area of the Fornax cluster. *AAP*, 620:A165.

Venhola, A., Peletier, R., Laurikainen, E., Salo, H., Iodice, E., Mieske, S., Hilker, M., Wittmann, C., Paolillo, M., Cantiello, M., Janz, J., Spavone, M., D'Abrusco, R., van de Ven, G., Napolitano, N., Verdoes Kleijn, G., Capaccioli, M., Grado, A., Valentijn, E., Falcón-Barroso, J., and Limatola, L. (2019). The Fornax Deep Survey (FDS) with VST. VI. Optical properties of the dwarf galaxies in the Fornax cluster. *AAP*, 625:A143.

Venhola, A., Peletier, R., Laurikainen, E., Salo, H., Lisker, T., Iodice, E., Capaccioli, M., Verdois Kleijn, G., Valentijn, E., Mieske, S., Hilker, M., Wittmann, C., van de Ven, G., Grado, A., Spavone, M., Cantiello, M., Napolitano, N., Paolillo, M., and Falcón-Barroso, J. (2017). The Fornax Deep Survey with VST. III. Low surface brightness dwarfs and ultra diffuse galaxies in the center of the Fornax cluster. *AAP*, 608:A142.

Vesperini, E. (1998). Evolution of the mass function of the Galactic globular cluster system. *MNRAS*, 299(4):1019–1039.

Villegas, D., Jordán, A., Peng, E. W., Blakeslee, J. P., Côté, P., Ferrarese, L., Kissler-Patig, M., Mei, S., Infante, L., Tonry, J. L., and West, M. J. (2010). THE ACS FORNAX CLUSTER SURVEY. VIII. THE LUMINOSITY FUNCTION OF GLOBULAR CLUSTERS IN VIRGO AND FORNAX EARLY-TYPE GALAXIES AND ITS USE AS a DISTANCE INDICATOR. *The Astrophysical Journal*, 717(2):603–616.

Virtanen, P., Gommers, R., Oliphant, T. E., Haberland, M., Reddy, T., Cournapeau, D., Burovski, E., Peterson, P., Weckesser, W., Bright, J., van der Walt, S. J., Brett, M., Wilson, J., Millman, K. J., Mayorov, N., Nelson, A. R. J., Jones, E., Kern, R., Larson, E., Carey, C. J., Polat, İ., Feng, Y., Moore, E. W., VanderPlas, J., Laxalde, D., Perktold, J., Cimrman, R., Henriksen, I., Quintero, E. A., Harris, C. R., Archibald, A. M., Ribeiro, A. H., Pedregosa, F., van Mulbregt, P., and SciPy 1.0 Contributors (2020). SciPy 1.0: Fundamental Algorithms for Scientific Computing in Python. *Nature Methods*, 17:261–272.

Whitmore, B. C., Zhang, Q., Leitherer, C., Fall, S. M., Schweizer, F., and Miller, B. W. (1999). The luminosity function of young star clusters in "the antennae" galaxies (NGC 4038/4039). *The Astronomical Journal*, 118(4):1551–1576.

Wolf, J., Martinez, G. D., Bullock, J. S., Kaplinghat, M., Geha, M., Muñoz, R. R., Simon, J. D., and Avedo, F. F. (2010). Accurate masses for dispersion-supported galaxies. *MNRAS*, 406(2):1220–1237.

Zanatta, E. J. B., Sánchez-Janssen, R., Chies-Santos, A. L., de Souza, R. S., and Blakeslee, J. P. (2021). A high occurrence of nuclear star clusters in faint Coma galaxies, and the roles of mass and environment. *arXiv e-prints*, page arXiv:2103.02123.

Zepf, S. E. and Ashman, K. M. (1993). Globular cluster systems formed in galaxy mergers. *MNRAS*, 264:611–618.

Zepf, S. E., Ashman, K. M., and Geisler, D. (1995). Constraints on the Formation History of the Elliptical Galaxy NGC 3923 from the Colors of Its Globular Clusters. *ApJ*, 443:570.

7 Appendix A

Several factors play an important role in the determination of the amount of GC within a galaxy and the values differ due to factors as the data set, method, area or what kind of background subtraction is applied. Therefore, these steps should be conducted with care and reflected upon to be able to draw valid conclusions.

7.1 Data and selection

The GC selection is based upon the outcomes of 19 galaxies from the work of Jordán et al. [2015], who studied 43 galaxies from the ACS Fornax Cluster Survey. They estimate a probability, p_{GC}, for each catalog source that it is a GC. In this work, we have only considered the GCs with a chance of 75% or higher as GCs. Their GC catalogue is determined through magnitude-, color- and half-light radii cuts. One big difference compared to the FDS data is that the GCs can be resolved from HST observations. This makes it possible to estimate the size of the GCs, which can be used to select out background galaxies more effectively than other parameters such as color or compactness.
The sources found in the images of the 19 galaxies are matched with the GCs sources from Jordán et al. [2015]. There can be several underlying reasons for not matching to all GCs in a galaxy image. The leading reason is the magnitude limit of the FDS data, almost no objects are found anymore fainter than $g = 25\ mag$ and therefore also not matched with the GCs from Jordán et al. [2015]. Another source for missing GCs arises when two objects are located close together ($< 1''$) and still resolved in the HST data but detected as one source in the FDS data. The last reason for missing matches which is linked to improper modelling of the light of the galaxy and therefore a bad subtracted image. The light is modelled using the *ellipse* function which will not be optimal for edge-on galaxies or galaxies having strong spiral structures. Especially, the subtracted central region of these galaxies is poor resulting in missing matches. An example of improper modelling due to an edge-on view is visible in Fig. 43.

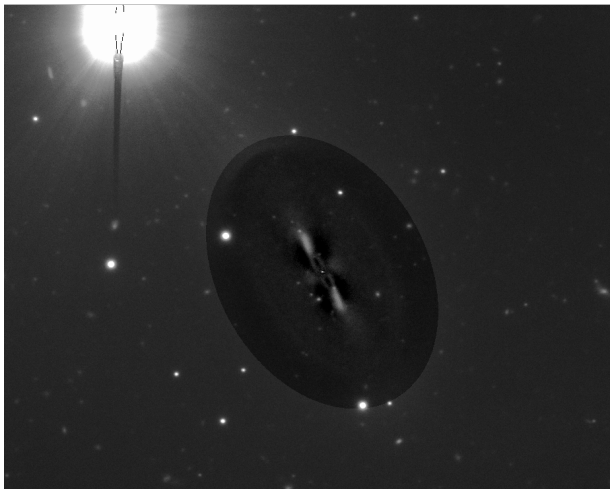

Figure 43: Subtracted frame of the edge-on galaxy FCC55.

To account for these missing matches (GCs), a completeness correction is applied (see 2.5). However, this completeness correction only takes into account the GCs that we do not find and Jordán et al. [2015] does find. This means that we take the GCs catalog with $pGC > 0.75$ as the true number of GCs in these 19 galaxies. This assumption is based on the completeness of

the data from Jordán et al. [2015] which is complete up to a g-magnitude of ~ 26.1 covering $\sim 95\%$ of the GCLF [Cote et al., 2004]. Even though we match and calculate the GCLF until a $g = 25\ mag$, it only needs to be complete till the GCLF peak at $24.5\ mag$ because all the GCs are counted up until the peak and doubled to account for the faint end.

7.1.1 Photometry

Problems that arise using aperture photometry are for example cosmic rays or bad pixels contaminating your aperture or nearby stars. The aperture magnitude from a source, possibly a GCs, can also be influenced by the light of a close objects ($< 1''$). These cases are either disregarded by the selection or their photometric values are too bright. These problems can be best solved by obtaining data where all these objects are resolved. For the first 19 galaxies, all the missing GCs where checked by eye and the unresolved cases are found.
In general, we have tried to apply aperture correction using a constant and solid method. The height of the aperture correction depends on the seeing which differs for every field. Even throughout the field there fluctuations in the seeing. By calculating the aperture correction new for every galaxy based on five unsaturated brightest stars available in their big fields, we do not consider extra effects of these local fluctuations. The aperture correction method was the same for all the galaxies and the corrections for the first 19 galaxies can be found in Fig. 10.
Another parameter for which we have tried to take care of the seeing effects is the compactness. If two similar sized point sources are measured with different seeing values, one object will appear blurrier than the other. The seeing is often denoted by the FWHM, which will be higher for larger seeing effects. When measuring the compactness the blurrier object will likely have a larger compactness value. To decrease these effect we use a normalization from Eq. 2.3.2. Also here five unsaturated bright stars from the big field are used to calculate a mean compactness, which can then be subtracted from every object. In fields where the seeing is higher, the mean compactness value for point sourced will be higher than for point sources in field where there is a low FWHM. By subtracting this mean compactness from every object, the compactness is normalized.

8 Appendix B

Magnitude range	μ_{g-i}	σ_{g-i}	$\sigma_{g-i}/\sqrt{N}$
21-22	0.149	0.269	0.075
22-23	0.047	0.142	0.018
23-24	0.027	0.221	0.018
24-25	0.026	0.333	0.030

Table 10: The mean off-set, standard deviation and standard deviation divided by the number of objects per g magnitude range between the this work and the work of Jordán et al. [2015]. N is the number of objects per g magnitude range.

Magnitude range	μ_{z-i}	σ_{z-i}	$\sigma_{z-i}/\sqrt{N}$
21-22	-0.138	0.306	0.085
22-23	-0.126	0.193	0.025
23-24	-0.131	0.334	0.027
24-25	-0.101	0.475	0.043

Table 11: The mean off-set, standard deviation and standard deviation divided by the number of objects per g magnitude range between the this work and the work of Jordán et al. [2015]. N is the number of objects per g magnitude range.

Magnitude range	μ_r	σ_r	$\sigma_r/\sqrt{N}$
21-22	0.011	0.100	0.008
22-23	0.013	0.102	0.006
23-24	0.0002	0.167	0.006
24-25	-0.020	0.220	0.007

Table 12: The mean off-set, standard deviation and standard deviation divided by the number of objects per g magnitude range between the this work and the work of Cantiello et al. [2020]. N is the number of objects per g magnitude range.

Magnitude range	μ_i	σ_i	$\sigma_i/\sqrt{N}$
21-22	0.072	0.085	0.009
22-23	0.054	0.122	0.007
23-24	0.061	0.160	0.006
24-25	0.044	0.262	0.009

Table 13: The mean off-set, standard deviation and standard deviation divided by the number of objects per g magnitude range between the this work and the work of Cantiello et al. [2020]. N is the number of objects per g magnitude range.

9 Appendix C

Target	RA_ICRS	DE_ICRS	rmag	gmag	reff	Class	Ref	Reason
FDS25_DWARF001	51.3331	-36.3849	12.6425	12.9577	66.50518	I	FCC39, ESO 357-29	1
FDS6_DWARF002	55.5949	-35.1541	12.6883	13.3766	11.4426	e(s)	FCC277, [JPB2015]	1
FDS5_DWARF000	55.3856	-34.8888	13.2292	13.7875	16.473021	I	FCC263, ESO 358-51	1
FDS25_DWARF241	51.2893	-36.3652	13.3442	13.7214	33.889919	I	FCC37	1
FDS6_DWARF176	56.3012	-35.5709	15.4917	15.6647	30.297041	I	FCC302, ESO 358-60	2
FDS33_DWARF088	56.6567	-37.1595	15.7547	16.4492	14.72654	e*	FCC314, LEDA 13822	3
FDS33_DWARF121	57.3021	-36.974	16.516	17.1869	18.096239	e	FCC331, LEDA 75007	3
FDS28_DWARF052	49.9835	-37.7865	16.9548	17.3422	6.19022	I	LEDA 617644	4
FDS6_DWARF454	56.1254	-35.1785	18.2504	18.7758	7.91242	e	FCC295, LEDA 74967	5
FDS25_DWARF296	50.4294	-36.208	18.3996	18.8918	12.17424	e	N	5
FDS9_DWARF135	54.5936	-33.6601	18.4239	18.9712	7.36712	e*	FCC209, LEDA 74812	5
FDS16_DWARF232	53.0219	-35.4257	18.5289	19.2335	6.16724	e*	FCC B770	6
FDS16_DWARF472	52.8447	-34.9714	18.8624	19.5062	7.10998	e	FCC94, FCC 94	6
FDS16_DWARF152	52.9532	-35.5825	19.2869	19.9932	4.90954	e	N	6
FDS33_DWARF129	56.9447	-36.9578	19.3493	19.9471	4.05442	e	N	3
FDS16_DWARF246	53.0917	-35.4061	19.3509	20.3968	9.0905	e*	N	4
FDS16_DWARF486	52.8204	-34.9616	19.3604	20.0859	6.4767	e*	LEDA 74657	6
FDS33_DWARF081	56.5214	-37.1716	19.6074	20.2283	2.64124	I	N	3
FDS7_DWARF275	55.5918	-36.4473	19.7923	20.0184	2.853	I	N	7
FDS27_DWARF103	50.1276	-36.6828	19.98	20.3892	2.45936	I	N	4
FDS11_DWARF229	54.5827	-35.4825	20.5579	21.2528	2.741	e	CGF 3-38, CGF 3-62	4
FDS17_DWARF303	53.3191	-36.0942	20.7856	21.2155	2.83424	e	N	4
FDS5_DWARF608b	55.2847	-34.2765	21.4903	21.845	1.58054	I	N	4
FDS22_DWARF256	52.1956	-37.1012	22.5603	23.0196	2.05348	e	N	4

Figure 44: List of the missing dwarf galaxies. The columns of the table represent the following properties: $target\_name$ is the name of the objects, RA_{ICRS} is the right accession, DE_{ICRS} declination, $rmag\_fit$ and $gmag\_fits$ are the galaxy magnitudes obtained through Sersic fitting, $reff$ is the effective radius in $''$, $Class$ is the morphological classification, Ref show other references. The last column ($Reason$) shows the reason why this galaxy is not included in this work: 1) problem fit (center objects), 2) problem fit (edge-on), 3) i-band data not available, 4) problem code (no GCs found in complete image), new version include galaxy 0 GCs, 5) problem code (too few good isolated stars for correction calculation), 6) problem weight-image, 7) problem gri-image. All the parameters are retrieved from Venhola et al. [2018a] unless stated otherwise.